Norwegian University
of Life Sciences

Master's Thesis 2023 30 ECTS
Faculty of Science and Technology

Simulation of a vertical bifacial PV system compared to measured values

Amalie Elisabeth Robsahm
Environmental Physics and Renewable Energy

Preface

This master's thesis represents the accomplishment of the final assignment within the master's degree in Environmental Physics and Renewable Energy at the Norwegian University of Life Sciences (NMBU). The thesis has been written at the Faculty of Science and Technology at NMBU, in collaboration with the Institute for Energy Technology (IFE).

First of all, I would like to thank my two supervisors Espen Olsen (NMBU) and Heine Nygard Riise (IFE) for their guidance, advice, and support during the work performed in this thesis. Your feedback has been essential for the completion of this work. I would also like to thank Heine for the opportunity to collaborate with IFE studying the concept from Over Easy Solar AS, and for being included in the community at IFE. Working with you has been educational and inspirational.

I also want to show my gratitude to Magnus Moe Nygård (IFE) for helping me understand the software bifacial_radiance and for the guidance while developing the 3D model of the Over Easy Solar AS test site at IFE. Magnus and Mari Øgaard (IFE) also deserve a thank you for all their helpful input, advice, and discussions while working on this thesis. Writing this thesis would not have been possible without you.

Finally, I would like to thank my mother Anna Maria Elisabeth Robsahm and friend Catarina Wear Edwin for proofreading, and not least my family and the people around me for always supporting me and showing interest in my work.

Amalie Elisabeth Robsahm

Ås, May 2023

Abstract

Photovoltaic (PV) systems have gained great interest the recent years with an increasing rate of installed capacity. In addition to the monofacial solar panels, the interest in bifacial solar panels, with an expected market share of 30.0 % by 2030, increases. The bifacial solar panels utilize irradiance on both the front and rear sides of the panel to generate energy. Hence, they are able to generate more energy than monofacial solar panels, making them interesting due to the demand for energy-efficient solar panels.

Over Easy Solar AS offers vertically mounted bifacial solar panels with a height of approximately 22.0 cm. Compared to conventional solar panels, they do not need intrusive fasteners and heavy ballast. Thereby, the solar panels are suitable for many flat roofs and green roofs as light and water are provided to the plants underneath. At the Institute for Energy Technology (IFE) at Kjeller, a test site including solar panels from Over Easy Solar AS has been mounted. As the technology from Over Easy Solar AS was introduced in 2021, addressing the performance using software to simulate the irradiance and power output, with possible factors affecting the simulations has not been researched much.

In this thesis, the software bifacial_radiance was assessed by creating a 3D model and simulating the irradiance using backward ray tracing for the test site at IFE. Even though bifacial_radiance is a time-consuming software, simulations were performed for clear-sky days, overcast days, and days with varying weather, for all seasons in Norway. Overall, the results from bifacial_radiance show an overestimation of the irradiance compared to measured irradiance with a percentage difference of 5.06 % – 16.54 %, but the model gives a rough estimate of the expected irradiance. Still, there are some days where there is good compliance between simulated and measured irradiance, and other days with a large deviation, especially during the winter. There are many possible explanations for the deviation between simulated and measured irradiance such as albedo, shading, and snow. Differences between the 3D model and the test site, such as orientation, materials, surrounding objects, and positioning of objects are other factors that may affect the irradiance. This thesis thoroughly and systematically addresses factors that may affect the simulated and measured irradiance for a PV system.

The simulated power using pvlib shows an overestimation of the DC and AC power compared to the measured values. Possible explanations are system losses such as shading and cable losses. Snow covering the solar panels is also a significant factor that may affect the measured power and cause a larger deviation in the results. When simulating the DC energy for a longer period of time, the percentage difference between measured and simulated energy varies in the range of 28.29 % – 119.58 %. Hence, further work and implementation of the factors such as shading and snow should be done to develop a more accurate model for simulating power and energy.

Sammendrag

De siste årene har det vært stor interesse rundt fotovoltaiske (PV) systemer og den installerte kapasiteten fortsetter å øke. I tillegg til ensidige solcellepaneler, har interessen for tosidige solcellepaneler, med en forventet markedsandel på 30.0 % innen 2030, økt. Disse panelene genererer energi fra innstråling på både fremsiden og baksiden av panelet. Derfor kan de generere mer energi enn ensidige paneler, noe som er en fordel grunnet etterspørselen etter energieffektive paneler.

Over Easy Solar AS tilbyr vertikale tosidige solcellepaneler med en høyde på ca. 22.0 cm. Sammenliknet med konvensjonelle solcellepaneler har de ikke behov for påtrengende festematerieller og tung ballast. Dermed er disse panelene egnet for mange flate tak og grønne tak, da lys og vann enkelt tilføres plantene under. Ved Institutt for Energiteknikk (IFE) på Kjeller er det montert et testanlegg med paneler fra Over Easy Solar AS. Ettersom teknologien til Over Easy Solar AS ble introdusert i 2021, har ytelsen av programvarer for å simulere innstråling og effekt, med faktorer som kan påvirke simuleringene ikke blitt forsket mye på.

I denne oppgaven ble programvaren bifacial_radiance vurdert ved å lage en 3D-modell og simulere innstråling ved hjelp av bakover strålesporing på test anlegget ved IFE. Selv om bifacial_radiance er en tidskrevende programvare, ble simuleringer gjort for dager med klar himmel, overskyede dager, og dager med varierende vær for alle årstider i Norge. Overordnet viser resultatene fra bifacial_radiance en overestimering av innstråling sammenliknet med målt innstråling med en forskjell på 5.06 % – 16.54 %, men modellen gir et grovt estimat av innstrålingen som kan forventes. Likevel er det dager med godt samsvar mellom simulert og målt innstråling, og andre dager med stort avvik, spesielt om vinteren. Det kan være mange mulige forklaringer på overestimering av innstråling, slik som albedo, skygge og snø. Forskjeller mellom 3D-modellen og testanlegget som orientering, materialer, omkringliggende objekter og posisjonering av objekter er andre faktorer som kan påvirke innstrålingen. Denne oppgaven tar grundig og systematisk opp mulige faktorer som kan påvirke simulert og målt innstråling i et PV-system.

Den simulerte effekten fra anlegget ved bruk av pvlib viser også en overestimering av DC og AC effekt sammenlignet med målte verdier. Denne overestimeringen kan komme av systemtap slik som skygge i anlegget og kabeltap. Snø som dekker panelene er også en signifikant faktor som kan påvirke målt effekt og dermed føre til større avvik. Når DC energien simuleres for en lenger periode er forskjellen mellom målt og simulert energi i området 28.29 % – 119.58 %. Derfor bør videre arbeid og implementering av faktorer som skygge og snø utføres for å utvikle en bedre modell til å simulere effekt og energi.

Contents

Preface i

Abstract ii

Sammendrag iii

1 Introduction 1
- 1.1 Scope of the thesis . . . 2
- 1.2 Structure of the thesis . . . 2

2 Theory 4
- 2.1 Irradiance . . . 4
  - 2.1.1 The Sun . . . 4
  - 2.1.2 Sun position and air mass . . . 4
  - 2.1.3 Direct and diffuse irradiance . . . 5
  - 2.1.4 Albedo . . . 7
- 2.2 The Nordic climate . . . 8
- 2.3 How do solar cells work? . . . 9
  - 2.3.1 Solar cells . . . 9
  - 2.3.2 Half-cut solar cells . . . 10
  - 2.3.3 The IV curve of a solar cell . . . 10
  - 2.3.4 Inverter and optimizers . . . 12
- 2.4 Bifacial solar technology . . . 13
  - 2.4.1 Over Easy Solar AS . . . 14
  - 2.4.2 Characterization of bifacial solar panels . . . 15
  - 2.4.3 Simulating the irradiance . . . 16

3 Methodology 19
- 3.1 The Over Easy Solar AS test site . . . 19
- 3.2 The 3D model in bifacial_radiance . . . 21
  - 3.2.1 Creating the 3D model and simulating the irradiance . . . 21
  - 3.2.2 The 3D model of the test site . . . 22
- 3.3 Collecting data . . . 23
- 3.4 Quality and uncertainty of data . . . 26
  - 3.4.1 Uncertainty analysis . . . 26
- 3.5 Performance of the 3D model . . . 28
  - 3.5.1 Simulating the irradiance . . . 28
  - 3.5.2 Angle of incidence . . . 30
- 3.6 Simulating the power . . . 31

4 Results & discussion 33
- 4.1 Simulated irradiance compared to measured irradiance . . . 33
  - 4.1.1 Time interval in data used to simulate the irradiance . . . 33
  - 4.1.2 Shading on the test site . . . 36
  - 4.1.3 Snow on the test site . . . 37
  - 4.1.4 Factors when creating the 3D model affecting the irradiance 39
  - 4.1.5 Evaluation of the 3D model for daily simulated irradiance . 40
  - 4.1.6 Aggregated simulation using cumulative sky . . . 41
- 4.2 The impact of selected factors on simulated irradiance . . . 42

4.2.1 Orientation of the 3D model . . . 42
4.2.2 Angle of incidence . . . 44
4.2.3 Albedo . . . 45
4.2.4 How albedo affects the measurement uncertainty . . . 49
4.3 Power output from the test site . . . 50
4.3.1 Models to simulate the DC power . . . 50
4.3.2 The time interval in data used to simulate power . . . 51
4.3.3 Simulated power and inverter efficiency for selected days . . . 54
4.4 Energy simulation using a cumulative sky . . . 57

5 Conclusion **59**

6 Further work **61**
6.1 Data . . . 61
6.2 The 3D model and simulating the irradiance . . . 61
6.3 Simulating the power and energy . . . 62

References **67**

A Datasheet for the pyranometer **68**

B Datasheet for the pyrheliometer **70**

C Datasheet for the inverter SE22200H **72**

D Scripts **74**

E Simulated irradiance compared to measured irradiance **76**
E.1 Clear-sky days . . . 76
E.2 Overcast days . . . 82
E.3 Days with varying weather . . . 86
E.4 Cumulative sky, irradiance for a longer period of time . . . 90

F Orientation of the test site **91**

G Measurement uncertainty due to albedo for simulated irradiance **93**

H Simulated power for selected days **96**
H.1 Clear-sky days . . . 96
H.2 Overcast days . . . 100
H.3 Days with varying weather . . . 104

List of Figures

1 Spherical coordinate system . . . 5
2 Diffuse and direct irradiance on a tilted surface . . . 6
3 GHI, DHI, and DNI for a clear-sky day and an overcast day . . . 6
4 Reflection of irradiance on a surface . . . 7
5 How a solar cell generates energy . . . 9
6 Half-cut solar cell . . . 10
7 IV curve for a solar cell . . . 11
8 Mounting of bifacial solar panels . . . 14
9 Solar panels from Over Easy Solar AS . . . 15
10 Ray tracing . . . 16
11 View factor . . . 17
12 The test site at IFE with solar panels from Over Easy Solar AS . . . 19
13 Google Earth Pro, orientation of the test site . . . 19
14 Measurements of the solar panels on the test site . . . 20
15 Bird-view of how the solar panels on the test site are connected . . . 20
16 Flowchart - bifacial_radiance . . . 22
17 3D model of the test site . . . 23
18 3D model of the test site from the side . . . 23
19 3D model of the test site, closeup from the side . . . 23
20 3D model of the test site from the east side . . . 23
21 Radiometers on the test site . . . 24
22 The reference cells on the test site . . . 25
23 Flowchart - angle of incidence . . . 30
24 Flowchart - simulating the power . . . 31
25 GHI the 12^{th} of August and the 23^{rd} of December 2022 . . . 33
26 Irradiance the 12^{th} of August and the 23^{rd} of December 2022 . . . 34
27 Irradiance the 12^{th} of August and the 23^{rd} of December 2022 with a 5-minute interval . . . 35
28 Objects surrounding the test site . . . 36
29 Webcam of the test site the 23^{rd} of December 2022 . . . 37
30 Irradiance the 22^{nd} of February 2023 . . . 38
31 Webcam of the test site the 23^{rd} of February 2023 . . . 38
32 Reference cells in the 3D model . . . 39
33 Simulated and measured irradiance using a cumulative sky . . . 41
34 Irradiance for different orientations of the PV system . . . 43
35 Irradiance where losses due to the AOI have been taken into account 44
36 Daily albedo . . . 45
37 Albedo the 17^{th} and the 18^{th} of December 2022 . . . 46
38 Webcam of the test site the 17^{th} of December 2022 . . . 47
39 Radiometers relative to the test site . . . 47
40 Albedo the 12^{th} of August 2022 and the 26^{th} of February 2023 . . . 48
41 Irradiance with measurement uncertainty due to albedo . . . 49
42 Comparison simulating the DC power with the singlediode and pvwatts models from pvlib . . . 51
43 DC and AC power the 22^{nd} of July 2022 . . . 52
44 Measured AC power and GHI the 22^{nd} of July 2022 . . . 53
45 Measured AC power the 22^{nd} of July 2022 plotted hourly . . . 53
46 DC power, AC power, and inverter efficiency the 12^{th} of August 2022 54

47 DC power, AC power, and inverter efficiency the 23^{rd} of December 2022 . . . 56
48 DC energy for the case of a cumulative sky . . . 57
49 Appendix - Irradiance the 12^{th} of August 2022 . . . 76
50 Appendix - Irradiance the 12^{th} of August 2022, 5-minute interval . . . 77
51 Appendix - Irradiance the 11^{th} of October 2022 . . . 78
52 Appendix - Irradiance the 23^{rd} of December 2022 . . . 79
53 Appendix - Irradiance the 23^{rd} of December 2022, 5-minute interval 80
54 Appendix - Irradiance the 1^{st} of March 2023 . . . 81
55 Appendix - Irradiance the 22^{nd} of July 2022 . . . 82
56 Appendix - Irradiance the 17^{th} of October 2022 . . . 83
57 Appendix - Irradiance the 26^{st} of December 2022 . . . 84
58 Appendix - Irradiance the 22^{nd} of February 2023 . . . 85
59 Appendix - Irradiance the 21^{st} of July 2022 . . . 86
60 Appendix - Irradiance the 7^{rd} of October 2022 . . . 87
61 Appendix - Irradiance the 24^{th} of December 2022 . . . 88
62 Appendix - Irradiance the 26^{st} of February 2023 . . . 89
63 Appendix - Irradiance using a cumulative sky . . . 90
64 Appendix - Irradiance the 12^{th} of August 2022, different orientations 91
65 Appendix - Irradiance the 12^{th} of August 2022, different orientations 92
66 Appendix - Irradiance the 12^{th} of August 2022 with measurement uncertainty due to albedo . . . 93
67 Appendix - Irradiance the 23^{rd} of December 2022 with measurement uncertainty due to albedo . . . 94
68 Appendix - Irradiance the 22^{nd} of February 2023 with measurement uncertainty due to albedo . . . 95
69 Appendix - DC power, AC power, and inverter efficiency the 12^{th} of August 2022 . . . 96
70 Appendix - DC power, AC power, and inverter efficiency the 11^{th} of October 2022 . . . 97
71 Appendix - DC power, AC power, and inverter efficiency the 23^{rd} of December 2022 . . . 98
72 Appendix - DC power, AC power, and inverter efficiency the 1^{st} of March 2023 . . . 99
73 Appendix - DC power, AC power, and inverter efficiency the 22^{nd} of July 2022 . . . 100
74 Appendix - DC power, AC power, and inverter efficiency the 17^{th} of October 2022 . . . 101
75 Appendix - DC power, AC power, and inverter efficiency the 26^{st} of December 2022 . . . 102
76 Appendix - DC power, AC power, and inverter efficiency the 22^{nd} of February 2023 . . . 103
77 Appendix - DC power, AC power, and inverter efficiency the 21^{st} of July 2022 . . . 104
78 Appendix - DC power, AC power, and inverter efficiency the 7^{th} of October 2022 . . . 105
79 Appendix - DC power, AC power, and inverter efficiency the 24^{th} of December 2022 . . . 106
80 Appendix - DC power, AC power, and inverter efficiency the 26^{st} of February 2023 . . . 107

List of Tables

1 Typical albedo for different materials 8
2 Materials used in the 3D model 21
3 Key information of the inverter 26
4 Technical specifications for the pyranometer and the pyrheliometer on the test site 27
5 Percentage difference between simulated and measured irradiance . 41
6 Percentage difference between simulated and measured DC energy . 58

Abbreviations

IFE	Institute for Energy Technology
IEA	International Energy Agency
PV	Photovoltaic
AM	Air Mass
STC	Standard Test Conditions
GHI	Global Horizontal Irradiation
DHI	Diffuse Horizontal Irradiation
DNI	Direct Normal Irradiation
BRDF	Bidirectional Reflectance Distribution Function
DC	Direct current
AC	Alternating current
c-Si	Crystalline silicon
MPP	Maximum Power Point
MPPT	Maximum Power Point Tracker
IV curve	Current-voltage curve
PV curve	Power-voltage curve
FF	Fill factor
VF	View factor
GCR	Ground Coverage Ratio
IMT	Ingenieurbüro Mencke & Tegtmeyer
TMY	Typical Meteorological Year
EPW	EnergyPlus
AOI	Angle of incidence
PERC	Passivated Emitter and Rear Contact
NREL	National Renewable Energy Laboratory
ASHRAE	American Society of Heating, Refrigeration and Air Conditioning Engineers
VCOM	meteocontrol Virtual Control Room

1 Introduction

Energy and the use of energy sources is an important topic considering the population growth and the high standard of living in today's society. The increasing demand for energy puts pressure on the energy market and the available energy resources. Despite a decreasing trend, non-renewable energy sources still account for most of the energy produced, in 2021 the share of non-renewable energy sources was 71.3 % [1]. The use of energy from non-renewable sources such as fossil fuels and coal releases greenhouse gases like carbon dioxide and water vapor, and therefore, contributes to global warming. To change this trend, non-renewable energy sources need to be phased out while renewable energy sources, such as solar and wind energy should be implemented. According to International Energy Agency (IEA), the share of renewable energy was 29.0 % in 2021, and it should be 60.0 % in 2030 to reach the goals in the Paris Agreement [1, 2]. To reach this goal, the increasing rate needs to be over 12.0 % annually from 2022 – 2030 [1].

Implementation of renewable energy has an increasing growth rate these days, especially wind and solar energy which accounted for 90.0 % of the renewable energy installations in 2021, reaching a total renewable energy share of 28.7 % [1]. Using photovoltaic (PV) systems to generate power has attracted great interest the recent years and in Nordic countries like Norway and Sweden. Focusing on Norway, the installed capacity of solar energy keeps increasing. In 2020 alone there was installed 40.0 MW and in 2022 the installed capacity reached 149.0 MW i.e., almost 4 times as much as the installed capacity in 2020 [3, 4]. By the end of 2022, the total installed capacity of solar energy in Norway reached 327.0 MW [4] and by 2030, the produced energy from PV systems is estimated between 1.2 TWh and 4.0 TWh [3].

There are challenges utilizing solar energy because the amount of generated energy depends on meteorological conditions, the most important being irradiance, soiling, albedo, and ambient temperature. Irradiance is an important parameter for the energy generated from solar panels, as generated energy increases with the irradiance. To utilize the PV system to its maximum, there need to be good conditions such as a clear-sky and high ground albedo for more reflection of the incoming irradiance. Compared to the climate at the equator, there are high seasonal variations in the Nordic climate, resulting in variations in the day length and weather such as periods with or without snow. The irradiance is also lower far away from the equator, but lower ambient temperature, especially in the winter, is an advantage and contributes to more efficient solar cells. At low ambient temperatures, the voltage in the solar cells increases and results in a higher energy generation rate [5]. Snow can also affect the energy generation rate positively due to higher ground albedo, provided that the solar panels are not covered in snow. [6]

With the demand for energy-efficient solar panels, the interest about bifacial solar panels is increasing. Even though the research on bifacial solar panels started in the 1960s [7], they are relatively new on the solar energy market with a market share of 12.0 % in 2020 [8]. By 2030, this market share is expected to increase to 30.0 % [8]. Bifacial solar panels have the advantage to receive and utilize irradiance from both sides of the panel to generate energy, and therefore, utilize the ground-reflected irradiance. In other words, there is potential for a higher amount of

generated energy than with monofacial solar panels of the same area.

In Norway, many PV systems are installed on flat and pitched roofs, but installing solar panels on flat roofs is not always possible. Depending on the wind load and snow load in the area, not all roofs are suitable for solar panels due to the heavy ballast needed to install a PV system. Also, installing solar panels on green roofs is not optimal as the panels cause shading on the grass and plants underneath. A new type of solar panel developed and introduced by Over Easy Solar AS in 2021 [9] has entered the market and is a solution to these challenges. Due to vertically mounted bifacial solar panels, with a height of approximately 22.0 cm [10], the solar panels are in no need of heavy ballast and intrusive fasteners [11]. Hence, they are suitable for many roofs. Their height and vertical mounting make the panels ideal for green roofs as well because the panel design ensures enough light and water for the plants underneath [12].

1.1 Scope of the thesis

With the increasing curiosity around the solar panels from Over Easy Solar AS, several sites in Norway and Europe are testing out these solar panels. One of them is the test site at the Institute for Energy Technology (IFE) located at Kjeller in Norway. This test site is studied in this master's thesis. As described in Section 2.4.1, these solar panels stand out from conventional bifacial solar panels due to their vertical mounting and size. Hence, methods for estimating the irradiance and the power output have not been thoroughly researched yet.

At the test site, several instruments for monitoring the irradiance, the power, and the energy output from the PV system have been installed. Thus, the site is optimal for testing software for estimating the irradiance, power, and energy for a vertical bifacial PV system from Over Easy Solar AS in the Nordic climate. Measured irradiance can be used as input when testing software and the results can be compared to measured values. Resultingly, the accuracy of the software and factors that may affect the results can be evaluated.

This thesis evaluates the performance of the software bifacial_radiance, RADIANCE, and pvlib to estimate the irradiance as well as the generated power and energy using measured data from the test site as input. The key work is presented in the list below.

- Construct a 3D model of the Over Easy Solar AS test site at IFE using bifacial_radiance and backward ray tracing.
- Simulate the irradiance with bifacial_radiance for selected days and months, compare the results with measured values, and address possible factors that can affect simulated and measured irradiance.
- Simulate the power and energy output from the test site for selected days and months, respectively, and compare the results with measured values.

1.2 Structure of the thesis

This master's thesis includes a theory section containing literature important for understanding the methods used and the result, followed by the methodology.

The methodology presents how the 3D model of the Over Easy Solar AS test site was developed with bifacial_radiance and RADIANCE, how the data were collected, and the measurement uncertainty in these data. Thereafter, the analysis of simulating the irradiance and estimating the generated power and energy is introduced before the results are presented and discussed. Finally, the conclusion displays the most important findings from the work performed in this master's thesis.

The appendix presents the datasheets for the instruments at the test site, a description of the important scripts created to develop the 3D model, the weather file, and to carry out the analysis. In addition to the attached ZIP file, the scripts are available on GitHub in the repository *Simulation-of-a-vertical-bifacial-PV-system-compared-to-measured-values*.

2 Theory

The theory section describes the relevant background for understanding the methods and results presented in this master's thesis. As this thesis is angled towards bifacial solar technology and the solar panels from Over Easy Solar AS, the topics described are solar irradiance, how solar cells work, and important bifacial solar parameters.

2.1 Irradiance

2.1.1 The Sun

The Sun is an important renewable resource that does not only contribute to generating energy, but also for sustaining life on Earth. Not only is the Sun an important factor in generating energy through solar panels, but the energy and heat from the Sun are fundamental for the other energy sources, both renewable energy sources like solar, water, and wind energy and non-renewable energy sources like coal, gas, and oil. [13]

The energy and heat produced in the Sun are the result of the fusion of hydrogen to helium in the core. This energy is radiated from the Sun at a rate of 3.8×10^{26} W, where 1.7×10^{18} W reaches the top of the atmosphere [14]. This amount of energy can be described through the solar constant at 1361 W/m^2 [15], which describes the incoming irradiance. On top of the atmosphere, the energy is evenly distributed, and thus, the solar constant is equal all over the world.

The atmosphere absorbs and reflects some of the incoming irradiance, consequently, the Earth receives a lower amount of irradiance than the top of the atmosphere. The amount of irradiance depends on the solar activity and the position of the Sun relative to an observation point on Earth, as described in Section 2.1.2. In the atmosphere, the irradiance can also be scattered by clouds, aerosols, and molecules, resulting in the Rayleigh effect and Mie scattering [16]. In the end, the irradiance reaching the surface of the Earth has wavelengths in the range of 300 nm – 4000 nm [17], this irradiance is defined as short-waved radiation. [14, 17]

2.1.2 Sun position and air mass

The irradiance and the solar constant on the Earth's surface are not evenly distributed due to the angle towards the Sun. The angle towards the Sun is lower at the equator than the poles, and thus, the irradiance at the equator is high and it decreases towards the poles as the amount of atmosphere to pass increases. The angle of the Sun also results in higher variations in the seasons towards the poles.

The position of the Sun relative to an observation point, A, on the Earth's surface is described through the spherical coordinate system shown in Figure 1. [17]

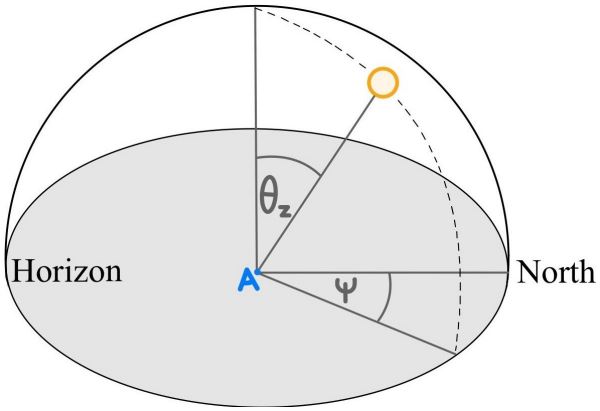

Figure 1: *The spherical coordinate system showing the solar zenith angle, ψ, and the solar azimuth angle, θ_z, for a Sun position relative to an observation point, A, on the Earth's surface.*

The parameters solar azimuth angle (ψ) and solar zenith angle (θ_z) are used to define the position of the Sun. While the solar azimuth angle describes the position of the Sun relative to the north ($\phi = 0\ ^\circ$) in a clockwise direction, the solar zenith angle describes the angle between the Sun and the vertical as shown in Figure 1. [17] The solar zenith angle can be calculated with equation 1

$$\cos\theta_z = \sin\delta\sin\phi + \cos\delta\cos\phi\cos\omega, \tag{1}$$

where ϕ and ω represent the geographical latitude according to the observation point A and the hour angle for a specific location, respectively. The last parameter, δ, is the declination angle, which for solar noon is defined to be zero. [17]

As mentioned, the position of the Sun affects the amount of atmosphere the sunlight needs to pass in order to reach the Earth's surface. This is described by the term Air Mass (AM). The AM can be calculated from the solar zenith angle by comparing the actual distance sunlight travels in the atmosphere and the shortest possible distance as shown in equation 2 [14]

$$AM = \frac{1}{\cos\theta_z}. \tag{2}$$

The shortest distance the sunlight needs to pass in order to reach the surface of the Earth happens when the Sun is directly above the observation point on the Earth's surface. In this case, θ_z is zero so that AM = 1, resulting in a solar spectrum defined as AM1. Increasing the solar zenith angle increases the AM because there is more atmosphere to pass, one of these is AM1.5. [14]

The solar spectrum AM1.5 together with an incoming irradiance at 1000 W/m^2 and a solar cell temperature at 25°C are important parameters included in the standard test conditions (STC) used while testing solar panels. [14]

2.1.3 Direct and diffuse irradiance

The Global Horizontal Irradiance (GHI) is the broadband irradiance [W/m^2] measured in a horizontal plane. GHI can be divided into two components, Direct

Normal Irradiance (DNI) and Diffuse Horizontal Irradiance (DHI) shown in Figure 2 [14].

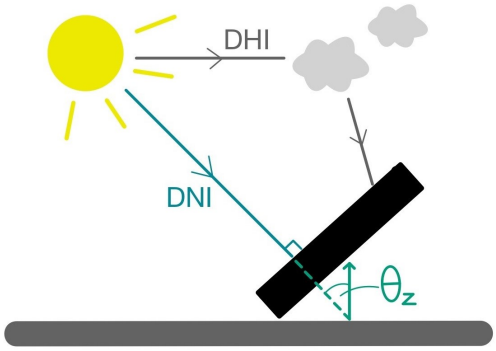

Figure 2: *Overview of the difference between DNI (Direct Normal Irradiance) and DHI (Diffuse Horizontal Irradiance) reaching a tilted surface.*

DNI is the irradiance from the Sun that travels through the atmosphere in a straight line. DHI on the other hand, is the irradiance that gets scattered on its way through the atmosphere before reaching the Earth's surface as shown in Figure 2. This scattering happens in all directions due to clouds, aerosols, molecules, and ground reflectance [17].

Together with the GHI, the parameters DHI and DNI can be measured with radiometers as described in Section 3.3. DNI and DHI constitute GHI with the relationship shown in the equation 3 [14]

$$GHI = DHI + DNI\cos(\theta_z). \tag{3}$$

Weather and latitude are important parameters that influence the amount of clouds, molecules, and aerosols in the atmosphere. Consequently, the amount of diffuse and direct irradiance is affected and varies throughout the day and with the seasons. Cloudy weather results in a lot of scattering and consequently zero to low DNI as shown to the right in Figure 3. On the other hand, for a clear-sky situation, there is low scattering and consequently a high DNI as shown to the left in Figure 3. [17] This figure shows the relative magnitude of GHI, DNI, and DHI for a typical clear-sky day and an overcast day.

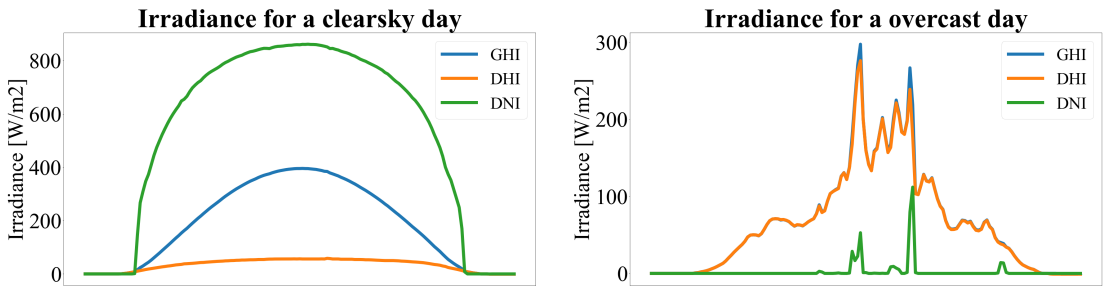

Figure 3: *Overview of the difference between GHI, DHI, and DNI for a clear-sky day (left) and an overcast day (right). Note that the irradiance on the y-axis of the two graphs is in different scales as the irradiance is higher for the clear-sky day.*

2.1.4 Albedo

Some of the incoming irradiance that irradiates a surface will be reflected. The amount of reflected irradiance depends on the albedo (α), which is defined as the percentage of reflected irradiance. Therefore, the albedo is a value between 0 and 1. For a pure black material (blackbody), the albedo is 0 as none of the incoming irradiance is reflected. For a pure white material, there is 100 % reflection, thusly the albedo is 1. [18] In other words, the higher the albedo, the more irradiance is reflected as shown with equation 4

$$\alpha = \frac{I_{down}}{I_{up}}. \tag{4}$$

Here I_{down} is the reflected irradiance from the ground and I_{up} is the incoming irradiance from the sky. These two parameters can be measured with an albedometer as explained in Section 3.3.

Albedo is a material-dependent value affected by changes in the material, such as age, water content, and irradiance. Rainfalls decrease the albedo, for sand rain reduces the albedo from an average of 0.4 to 0.34 [18]. If there is a high amount of water content in the material, the albedo decreases as well [18]. Also, the texture of the surface has an impact on the albedo. If the surface is matt and rough, the solar irradiance gets scattered by the surface in all directions resulting in diffuse reflection and a lower albedo. Glossy surfaces have higher albedo because the irradiance is reflected uniformly with no scattering, resulting in specular reflection. [18] The difference between diffuse and specular reflection on a surface is shown in Figure 4. Hence, depending on the surface, there can be a combination of specular and diffuse reflection.

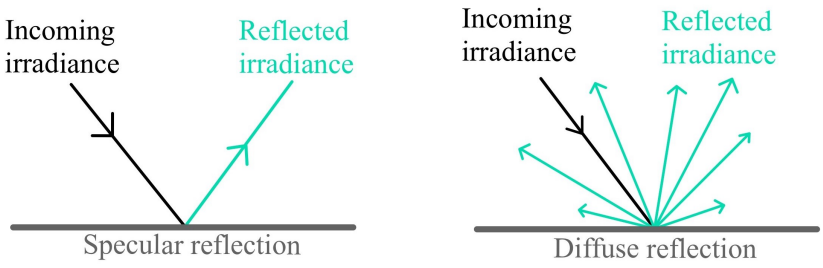

Figure 4: *Specular and diffuse reflection form an irradiance beam reaching a surface.*

Regarding irradiance, the albedo depends on the amount of diffuse light. The incoming solar irradiance is reflected and scattered by particles in the atmosphere such as clouds and aerosols, resulting in a higher amount of diffuse light. The diffuse light reaching a surface, such as a roof, can be scattered in multiple directions depending on physical parameters such as texture, roughness, and the angles of the incoming and outgoing irradiance. This scattering can impact the amount of reflected irradiance and thereby affect the albedo. As the solar position varies throughout the day, the albedo varies. In the morning and the afternoon, when the irradiance hits the surface at a lower angle, there is a higher probability of reflection, which can affect the albedo. This is more noticeable in the Nordic climate far away from the equator as mentioned in Section 2.1.1. [18, 19]

How the irradiance is reflected and how the physical parameters mentioned affect the albedo can be explained by the Bidirectional Reflectance Distribution Function (BRDF). This function takes the physical parameters such as texture, roughness, and irradiance, as mentioned above, into account together with the direction of the diffuse and specular reflected irradiance. [19, 20] BRDF can be used to calculate the so-called black-sky and white-sky albedo, the surface albedo due to direct irradiance and diffuse irradiance, respectively [21].

The range of typical albedo values for different materials is shown in Table 1.

Table 1: *Range of typical albedo values for different materials [22, 23, 24].*

Material	**Range of albedo**	**Reference**
Asphalt	0.05 – 0.2	[22, 23]
Fresh snow	0.9	[24]
Grass	0.25 – 0.3	[22, 23]
Grassland	0.1 – 0.25	[24]
Concrete	0.25 – 0.7	[22, 23]
Forest	0.05 – 0.2	[24]

As the table shows, the range of albedo values is for some materials large in relation to an albedo between 0 and 1. In addition to the factors affecting the albedo mentioned above, the composition of the material is important. For aluminum, there is a difference between matt and polished material. For concrete, on the other hand, there is a difference between regular concrete and concrete combined with white cement. Because the table above does not distinguish between these, the ranges of albedo values are broader.

2.2 The Nordic climate

Solar energy in the Nordic climate has its advantages and disadvantages. With high latitudes and large variations in the seasons due to the changing angle towards the Sun, the irradiance varies throughout the year. This results in a higher proportion of irradiance accessible for solar energy in the summer than in the winter [25]. In addition to irradiance, the performance of solar panels increases with lower ambient temperature, which is the case for the Nordic climate during the winter [5].

The seasonal variations in ambient temperature and weather does not only affect the amount of irradiance, but also the albedo. Snowfalls in the winter with a high albedo, as shown in Table 1, causes more ground-reflected irradiance. The orientation and tilt of solar panels affect the amount of soiling from snow and if the solar panels get covered in snow or not. With a higher panel tilt, the snow can fall off easier compared to a tilt at for example 10°, which is the common tilt for solar panels mounted on flat roofs in Norway. With a 10° tilt, the snow can cover the panels for a longer period of time and thereby reduce the amount of generated energy. [26]

2.3 How do solar cells work?

2.3.1 Solar cells

There are several types of solar cells on the market, the most common being monocrystalline and polycrystalline silicon (c-Si) due to their efficiency, simple manufacturing, and the abundance of the needed raw materials [27, 28].

Solar cells absorb the incoming solar irradiance and generate energy through an external circuit as shown in Figure 5. The solar cells consist of a semiconductor material that is doped with another material to improve the properties to conduct electricity and thereby generate energy. For c-Si solar cells, the semiconductor is silicon, usually doped with boron and phosphorus for P- and N-doping, respectively. N-doping results in an excess of electrons, while P-doping results in an excess of holes due to a deficit of electrons. The P- and N-doped semiconductor constitutes the electrically neutral P- and N-side, respectively. [14, 29]

When the P- and N-side are brought together, electrons and holes recombine to create a PN junction as shown in Figure 5. The recombination happens as the electrons and holes are free-charge carriers. Boron and phosphorus, used in doping, are not free-charge carriers, resulting in an excess of fixed charges in the PN junction when the electrons and holes recombine. [14, 29]

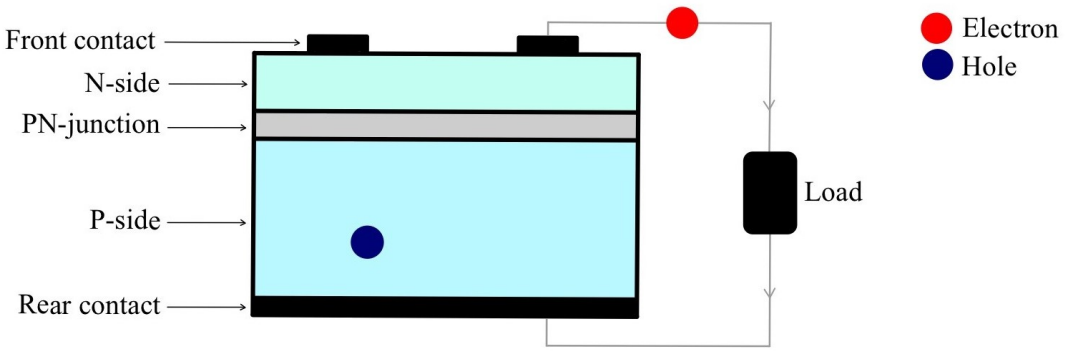

Figure 5: *A overview of how a solar cell works. When incoming photons reach the N-side in a solar cell an electron-hole pair is created. The electron transfers into the external circuit through a front contact to create a direct current (DC) and the hole transfer to the P-side. Thereafter, the electron-hole pair is recombined in the P-side when the electron from the external circuit arrives through the rear contact.*

When sunlight, photons, reaches the N-side, electrons from the N-side are excited, creating electron-hole pairs. While the holes transfer into the P-side, the electrons are transferred through the front contact of the solar cell into an external circuit with a load where a direct current (DC) is generated. Thereafter the electron reaches the P-side through the rear contact of the solar cell to recombine with the holes. [14]

Solar cells with approximately the same characteristics combined in series constitute a solar panel. One way to estimate the amount of generated DC power (P_{dc}) for a solar panel is to use the pvwatts model from National Renewable Energy Laboratory (NREL) in equation 5 [30, 31]

$$P_{dc} = \frac{I_{recieved}}{1000} P_{dc0}(1 + \gamma_{pdc}(T_{cell} - T_{ref})). \tag{5}$$

Here $I_{recieved}$ is the irradiance [W/m^2] received by the solar cells, T_{cell} is the temperature [°C] in the solar cell, and γ_{pdc} is the temperature coefficient for the power [1/°C]. T_{ref} is the temperature [°C] at reference conditions, STC.

The last parameter in equation 5 is P_{dc0}, which is the rated DC power of the system. If the DC power output from a solar panel rated at for example 550 Wp is calculated, $P_{dc0} = 550$ Wp. On the other hand, if the DC power output from a PV system with n solar panels of 550 Wp is calculated, $P_{dc0} = 550 \cdot n$ Wp.

2.3.2 Half-cut solar cells

Solar cells can be standard solar cells or half-cut solar cells as shown in Figure 6. By using a laser, a solar cell can be cut into two parts to make a half-cut solar cell. When half-cut solar cells are used in solar panels, the number of cells doubles compared to solar panels consisting of standard solar cells. The current in each solar cell is halved when half-cut cells are used, thus, there is less resistance influencing the current. Due to lower resistance, the power loss is lower, and the efficiency increases. Also, in half-cut solar cells, there is a negligible shading loss because if one half is shaded, the other half will still be active. [27]

There are disadvantages with half-cut solar cells as well, due to laser cutting there is an added step in the manufacturing line of producing solar panels. Cutting a solar cell also makes the cell more fragile and there can be mismatch losses and challenges with edge recombination. [27]

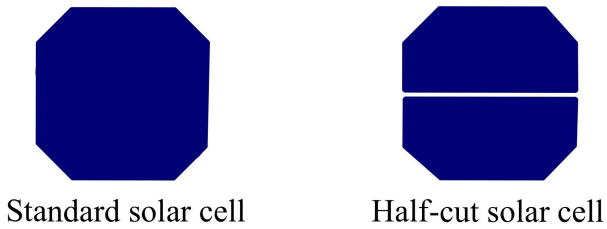

Figure 6: *Comparison of a standard solar cell (left) and a half-cut solar cell (right).*

2.3.3 The IV curve of a solar cell

To characterize a solar cell, an IV curve (current-voltage curve) shown in Figure 7 is used. This curve describes the current response of a solar cell as a function of the imposed voltage. Also in Figure 7, the corresponding PV curve (power-voltage curve) describing the power output as a function of the imposed voltage is displayed. [14]

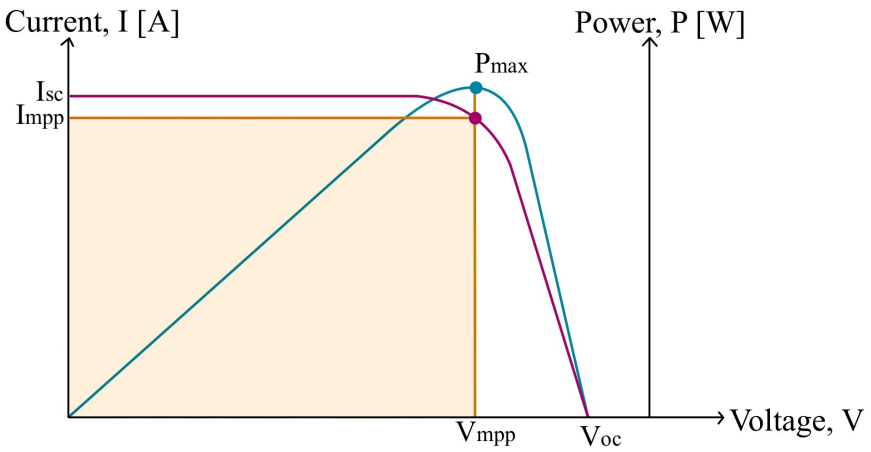

Figure 7: *A typical IV curve and PV curve for a solar cell where the maximum current (I_{mpp}) and the short-circuit current (I_{SC}) is marked along the left y-axis. The corresponding maximum voltage (V_{mpp}) and the open-circuit voltage (V_{OC}) are marked along the x-axis. The maximal power (P_{max}) and the shaded area constituting the fill factor (FF) are shown as well.*

The relationship between the current and the voltage can be described by the single diode equation [14, 32]

$$I = I_L - I_0\left[exp\left(\frac{V + IR_s}{nN_sV_{th}}\right) - 1\right] - \frac{V + IR_s}{R_{sh}}. \tag{6}$$

In this equation, I_L is the current [A] in the solar cell due to the light, I_0 is the saturation current [A] and I is the current [A]. R_s and R_{sh} is respectively the series and shunt resistance [Ω], while V is the voltage [V] and V_{th} is the thermal voltage [V]. Lastly, N_s is how many cells are connected in series and n is the diode factor. The diode factor ranges between 1 and 2, with 1 being the case of an ideal solar cell [14].

R_s and R_{sh} are two important parameters that affect the IV curve. Figure 7 shows an ideal solar cell and is the result of a low R_s and a high R_{sh}. When R_s is low there is little resistance in the conductive materials of the solar cell, such as the metal. The low resistance reduces the losses so that the current passes easily. On the other hand, a high R_{sh} is important to prevent a leakage current that will increase the losses and reduce the efficiency of the solar cell. [14, 33] Therefore, a low R_s and a high R_{sh} are important for an efficient and optimized solar cell.

In the situation of an open-circuit, the solar cell delivers no current, in other words, the open-circuit current is 0 A. The corresponding open-circuit voltage, (V_{OC}) [V], across the solar cell, is then at its maximum. In the opposite case, when the solar cell suffers a short-circuit, the voltage is 0 V. Then the current is at its maximum, defined as the short-circuit current (I_{SC}) [A]. I_{SC} and V_{OC} are not constant values as they vary with the temperature and the incoming light that determines the incoming photon flux and irradiance. I_{SC} also depends on characteristics specific to the solar cell like absorption and reflection. [14]

Marked on the IV curve are also I_{mpp} [A] and V_{mpp} [V]. This is the current and voltage when the solar cell operates at the Maximum Power Point (MPP). When running the solar cells in a PV system at MPP, the operation of the system is

optimized, and maximum power (P_{max}) [W] is achieved. This is shown in the PV curve in Figure 7. On the other, hand the MPP will vary with the ambient conditions like irradiance and temperature. With a temperature change and shading, the MPP is affected, which may change the characteristics of the IV curve and PV curve. [14] I_{mpp} and V_{mpp} are used to calculate the maximum power as shown in equation 7 [14]

$$P_{max} = I_{mpp}V_{mpp}. \tag{7}$$

The last parameter shown in the IV curve is the fill factor (FF) that describes the relationship between the maximum power and the product of the parameters V_{OC} and I_{SC}. For a solar cell with good quality, the FF is expected to exceed 70 % [33]. The FF is visualized as a rectangle as shown with the shaded area in Figure 7 and is described with equation 8 [14]

$$FF = \frac{I_{mpp}V_{mpp}}{I_{SC}V_{OC}}. \tag{8}$$

These parameters can be used to calculate the efficiency η for a solar cell. This efficiency describes the amount of energy produced for a given irradiance, and therefore, indicates the quality of the solar cell. The efficiency can be calculated with equation 9

$$\eta = \frac{I_{SC}V_{OC}FF}{IA}, \tag{9}$$

where I is the irradiance [W/m^2] and A is the area of the solar cell [m^2]. The efficiency of a solar cell is affected by temperature changes relative to the STC at 25°C. The efficiency of a solar cell with a temperature of T_M can be calculated as followed

$$\eta(T_M, I_{STC}) = \eta(STC) + \frac{\partial\eta}{\partial T}(STC)(T_M - T_{STC}), \tag{10}$$

where $\partial\eta/\partial T$ is defined as the efficiency temperature coefficient as STC [14].

As mentioned, temperature and irradiance are two important factors affecting the IV curve and the efficiency of a solar cell. As the ambient temperature decreases, so does the temperature of the solar cell. This results in a higher V_{OC} and an increase of the power output due to an MPP shift towards higher voltages. I_{SC} on the other hand, is proportional to the irradiance due to a higher number of photons absorbed by the solar cell. Hence, higher irradiance increases I_{SC}, but at high I_{SC}, V_{OC} may start to decrease due to the efficiency limit of the solar cell. [33]

2.3.4 Inverter and optimizers

Most of the electricity used today is alternating current (AC). Therefore, an inverter is connected to the PV system to convert the DC power to AC power that can be fed to the grid or used in the household. Not only does the inverter convert

the power from DC to AC, but it also monitors the system and communicates the status of the PV system to the user/grid. [34]

There are many different types and sizes of inverters, all depending on the amount of generated power from the PV system and if the electrical grid is 230 V or 400 V AC, if there is single-phase or three-phase, respectively. Single-phase inverters are coupled with one of the phases in the grid while three-phase inverters are coupled with all three phases. These inverters are usually used for smaller and larger PV systems, respectively. To achieve the maximum generated AC power, the efficiency of the inverter needs to be high to reduce the losses during the conversion from DC to AC. [14] Hence, typical inverter efficiencies are in the range 95 % – 98 % [35]. When both the DC and the AC power are known, the inverter efficiency can be calculated by looking at the relationship between AC and DC power. A more complex model to calculate the inverter efficiency, when the AC power is not known, is with the pvwatts model from NREL in equation 11 [31, 30]

$$\eta = \frac{\eta_{nom}}{\eta_{ref}}\Big(- 0.0162\zeta - \frac{0.0059}{\zeta} + 0.9858\Big), \tag{11}$$

η_{nom} and η_{ref} are the nominal and reference efficiency of the inverter, respectively [31, 30]. If not known, η_{ref} can be calculated as followed

$$\eta_{ref} = \frac{P_{ac0}}{P_{dc0}}, \tag{12}$$

where P_{dc0} is the inverter's input limit of DC power and P_{ac0} is the AC-rating [30]. These parameters, together with the DC power (P_{dc}) are used to define ζ as shown in equation 13

$$\zeta = \frac{P_{dc}}{P_{dc0}} = \frac{P_{dc}\eta_{nom}}{P_{ac0}}. \tag{13}$$

To optimize the performance of a PV system, an inverter can be used in combination with optimizers. An optimizer can be connected to one or more solar panels and include a DC-DC converter and an MPPT (Maximum Power Point Tracker). Using optimizers makes it possible for solar panels to work at their MPP and maximize the performance of the PV system. These optimizers can then be connected in series to the inverter. [14]

2.4 Bifacial solar technology

Research on the bifacial PV technology has been done since the 1960s [7], but it is a new concept on the market with an expected market share of 30% in 2030 [8]. There may be several reasons that bifacial solar panels did not enter the market in the 1960s such as the technology and reductions in cost. There have been many advancements in solar cell technology since the 1960s, and with the increasing demand for solar energy, the cost of producing bifacial solar panels has decreased, making them more cost-effective [7, 8]. While monofacial solar panels only absorb irradiance from the front side of the panels, bifacial solar panels can absorb irradiance also on the rear side and generate energy from both sides of

the panel. The demand for energy-efficient solar panels has increased over the years, making bifacial solar panels more interesting due to the higher power output compared with monofacial solar panels of the same area. [28]

Since bifacial solar panels generate energy from both sides of the panel, higher albedo results in more reflected irradiance and more generated energy from the rear side. The irradiance on the rear side of the solar panels is not evenly distributed due to the dependence on factors such as albedo and diffuse irradiance. The irradiance on the rear side is also affected by the tilt angle of the solar panels due to shading. A low tilt can result in more shading than vertically mounted solar panels. The rear side of vertically mounted solar panels can also be irradiated by more direct and diffuse irradiance. Tilted and vertically mounted bifacial solar panels shown in Figure 8 are common configurations. [7]

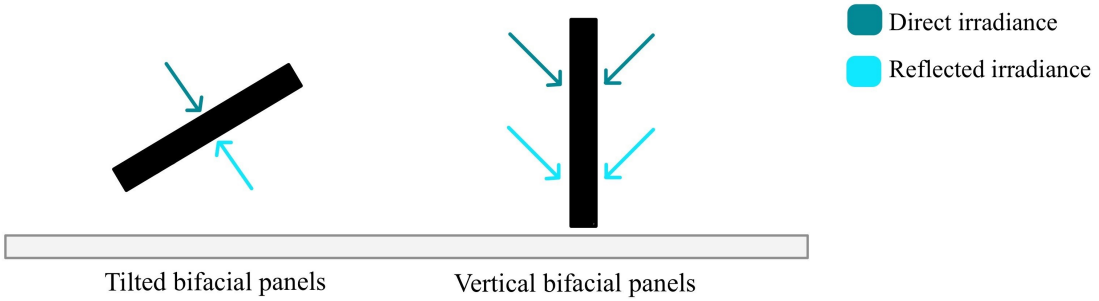

Figure 8: *Illustration of tilted bifacial solar panels (left) and vertically mounted bifacial solar panels (right).*

The tilted bifacial panels to the left in Figure 8 are similar to the traditional mounting of monofacial solar panels, this configuration is used both on the roof and in ground-mounted installations. The tilt of the panels can be adapted to optimize the amount of generated energy for the location. For large PV systems with optimal conditions, i.e. mounting the system at least 0.5 m above the ground, ensuring low shading from the rear side, a high row distance between the rows of panels, and a high ground albedo such as fresh snow, the bifacial gain for tilted bifacial solar panels can increase by up to 30 % [36].

The vertical mounting does not cover much of the ground compared to the tilted mounting, hence, the ground coverage ratio (GCR) is low. Therefore, vertical mounting is beneficial in areas with farming practices, AgriPV [36]. Often the bifacial solar panels are large and meant for ground mounting, but a new concept from Over Easy Solar AS has made it possible to install vertical bifacial solar panels on flat roofs and green roofs as described in section 2.4.1.

2.4.1 Over Easy Solar AS

In 2021, Over Easy Solar AS was founded by Trygve Mongstad with the concept of vertical bifacial PV systems for green roofs and flat roofs [9]. Several installations have been mounted in Norway as well as other countries such as France and Spain [10].

The solar panels from Over Easy Solar AS stand out from regular vertical bifacial solar panels because of their size. The commercial solar panels shown in Figure 9, are 1420 x 220 mm consisting of 8 standard solar cells, rated 50 Wp. Solar panels

with the size of 1350 x 206 mm consisting of 14 half-cut solar cells, rated 40 Wp are also tested on several test sites [10]. With no need for heavy ballast and intrusive fasteners [11], these panels are applicable for many flat roofs where there is a limit for ballast and for green roofs as the panel design ensures water and light for the plants underneath [12]. Also, the distance between the bottom of the panels and the roof can be adjusted, as shown to the right in Figure 9, to let the plants grow without affecting the solar panels and the generated power.

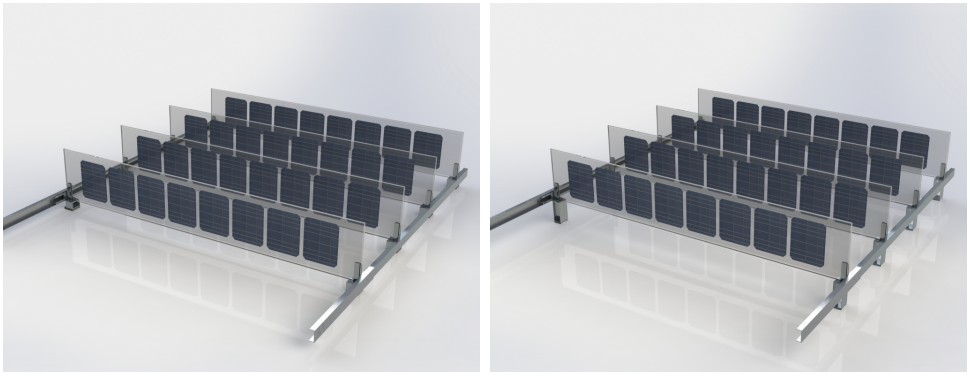

Figure 9: *The commercial Over Easy Solar AS solar panels for flat roofs (left) and green roofs (right) [11, 12]. In the picture to the right, for green roofs, the distance between the ground and the panels is higher than in the left picture for flat roofs.*

The solar panels from Over Easy Solar AS can be mounted either in an east/west or a south/north configuration. While the east/west configuration results in one generated energy peak in the morning and one in the afternoon, the south/north configuration have one energy peak in the middle of the day.

2.4.2 Characterization of bifacial solar panels

For bifacial solar panels, the bifaciality factor and the bifacial gain are two important parameters used to describe the performance of the solar panels by looking at the efficiency on the rear side and the increase in energy yield compared to monofacial solar panels, respectively.

Bifaciality factor

The efficiency on the rear side of a bifacial solar panel is not the same as on the front side. The bifaciality factor (BF) is used to describe the efficiency on the rear side relative to the front side and can be calculated with equation 14 [37]

$$BF(\%) = \frac{\eta_{rear}}{\eta_{front}} \times 100\%. \tag{14}$$

Here η_{rear} is the efficiency on the rear side of the solar panel and η_{front} is the efficiency on the front side. This factor is a number between 0 % and 100 %. For bifacial PERC (Passivated Emitter and Rear Contact) [28] solar cells the bifaciality factor is approximately 65 % – 80 % [28, 9].

The bifaciality factor is a non-constant value and the efficiency on the front and the rear side will depend on the solar panel, its temperature, and the irradiance [37]. Still, the bifaciality factor is normally defined during STC.

Bifacial gain

With bifacial solar panels the energy yield increases. The term bifacial gain (BG) describes the increase in energy yield for a bifacial solar panel compared to a monofacial solar panel [38]. For a solar panel, the bifacial gain can be calculated with equation 15 [38]

$$BG = \frac{E_{rear} - E_{front}}{E_{front}}, \tag{15}$$

where E_{rear} is the energy yield on the rear side of the solar panel, and E_{front} is the energy yield from the front side of the solar panel. For a PERC bifacial solar panel, BG is approximately 4 – 8 % [37].

The bifacial gain is site-specific and temporal, and therefore, is not a constant value [20]. As mentioned, the irradiance on the rear side of a bifacial solar panel will depend on several factors like albedo, shading, operating conditions, and temperature. A high ground albedo will for example result in more reflected irradiance and can affect the generated power from the rear side of the solar panel. Hence, bifacial gain must be assumed for each and every site.

2.4.3 Simulating the irradiance

As the irradiance on the rear side of bifacial solar panels is not evenly distributed, simulating the rear side irradiance is a complicated task. Models used to simulate the irradiance in bifacial PV systems are ray tracing, view factor, and transposition models.

Ray tracing

Ray tracing is a simulation method where the interactions between virtual objects in a scene and traced light rays are used to make an image. Forward and backward ray tracing, shown in Figure 10, are the two methods used.

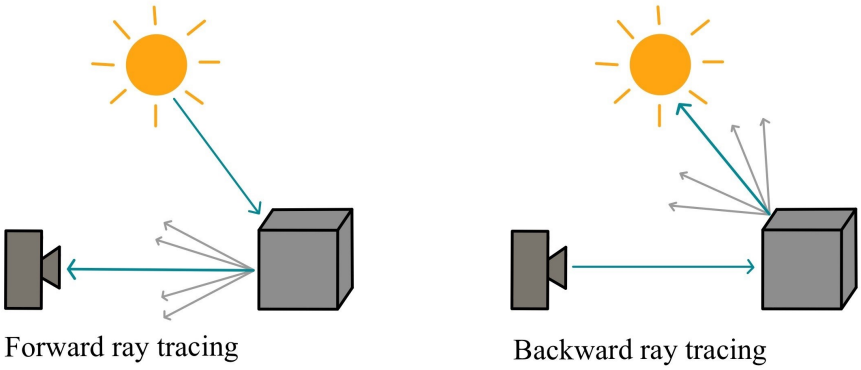

Figure 10: *Illustration of forward and backward ray tracing.*

The difference between forward and backward ray tracing is that while forward ray tracing tracks the light rays from the light source to the object before reaching the sensor, backward ray tracing tracks the light rays from the sensor to the object

before reaching the light source. Forward ray tracing is an accurate, but time-consuming method as the light rays reaching the sensor is a fraction of the light rays from the object as shown in Figure 10. Backward ray tracing on the other hand is more time efficient as only the light rays reaching the sensor are simulated. [20, 24]

Ray tracing models can take into account both the direct and diffuse shading on both sides of the solar panel and thereby make realistic light situations [24]. Hence, these models are promising for making accurate irradiance simulations for bifacial PV systems. In this thesis, RADIANCE has been used to perform backward ray tracing.

View factor

Another tool for simulating the irradiance is view factor (VF) models which assume conservation of radiation and isotropic scattering of the irradiance reaching a surface. VF describes the amount of irradiance reaching a surface B from surface A and can be calculated with equation 16 followed by the irradiance on surface B with equation 17 [24, 20]

$$VF_{A\to B} = \frac{1}{A_A}\int_{A_A}\int_{A_B}\frac{cos\theta_A cos\theta_B}{\pi s^2}dA_A dA_B, \tag{16}$$

$$I_B = \sum VF_{A\to B}\cdot I_A. \tag{17}$$

Here the area of surfaces A and B are represented by A_A and A_B respectively, s is the ray between surface A and B, while θ_A and θ_B are the angles between the irradiance ray from surface A to B, and the normal (n_A and n_B) of the surfaces. This is displayed in Figure 11. I_A defines the reflected irradiance from surface A. [24]

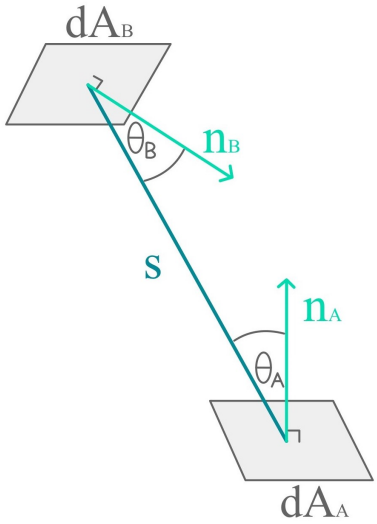

Figure 11: *Overview of the parameters implemented in view factor models.*

The VF affects the amount of reflected and diffuse irradiance on solar panels. There are several view factors to take into account such as solar panels to the sky, solar panels to the ground, and the view from one solar panel to another. Due to

shading in a PV system, there is a difference in view factor between unshaded and shaded ground. [39]

Most of the developed VF models for studying PV systems and simulating the irradiance, such as PVsyst, pvfactors, and bifacialvf, are in 2D. These 2D models assume the length of the rows in a PV system to be infinite, and consequently consistent irradiance throughout all the rows. The assumption of infinite row length may be fair for large PV systems, but for smaller systems, the error increases. Also, due to the 2D models, the edge effects are neglected because the model assumes equal ground shading for all solar panels. This can cause larger errors for bifacial PV systems where the edge effect is important since the unshaded view factors are higher for the solar panels on the edge in a row. Thus, there is more irradiance on the edge. [24]

Transposition models

Transposition models are another method to predict the irradiance on tilted surfaces. With site-specific parameters like solar zenith angle and surface inclination, these models are used to correlate the diffuse irradiance on an inclined surface from measured or simulated irradiance on the horizontal surface. [40, 41]

The isotropic transposition models are the simplest models which assume a uniform distribution of diffuse irradiance over the sky dome and no horizon brightening is assumed. Therefore, the diffuse irradiance on the inclined surface depends on the amount of sky dome seen by the surface. The other type of transposition model is anisotropic, these models assume non-uniformly distribution of the diffuse irradiance in the area close to the Sun, while the diffuse irradiance on the rest of the sky dome is uniformly distributed. [41] One of the most used anisotropic transposition models is Perez, this model splits the sky dome into three areas, the isotropic background, the circumsolar disc, and the horizon band [40]. Hence, the circumsolar and horizon brightening is taken into account. Still, not all anisotropic transposition model takes the horizon brightening into account, one being the Hay model [42]. Both the Perez and the Hay model is offered in the software PVsyst.

3 Methodology

This section provides information about the test site and how the 3D model of the PV system has been developed. How the data have been collected and how the different analyses have been performed are presented as well.

3.1 The Over Easy Solar AS test site

In this thesis, a test site located at the IFE consisting of solar panels from Over Easy Solar AS has been studied. A 3D model of the test site has been developed to simulate the irradiance on the PV system and estimate the generated power and energy.

The test site consists of 36 bifacial PERC solar panels, rated 40 Wp, installed on a bitumen roof. The bifaciality factor of the panels is in the range of 75.6 % – 80.6 %, with an average of 78.6 %. For the case of this thesis, the average bifaciality factor has been used. A picture of the test site from the south-east is shown in Figure 12, with a total installed capacity being 1440 Wp.

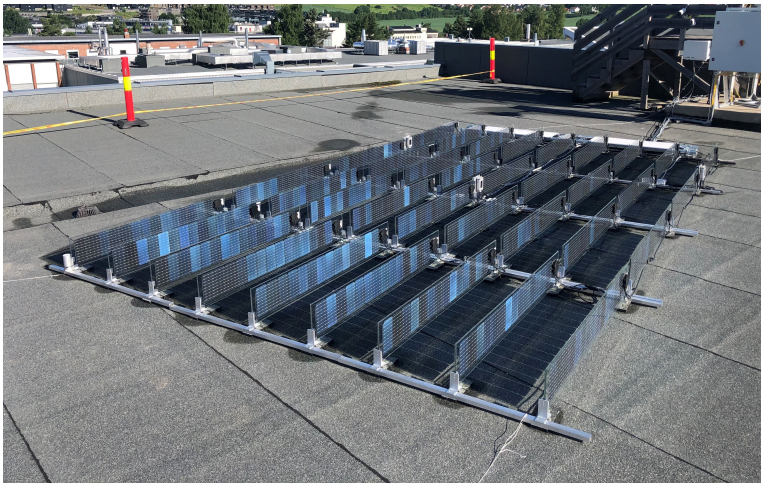

Figure 12: *Overview of the test site at IFE with the solar panels from Over Easy Solar AS taken from the south-east. The panels are facing east/west.*

As Figure 12 displays, the array of solar panels is fixed-tilted in a vertical position. They are mounted in an east/west configuration with the rear side of the panels facing east. The azimuth angle towards the east was found to be approximately 86° by using Google Earth Pro [43] as shown in Figure 13.

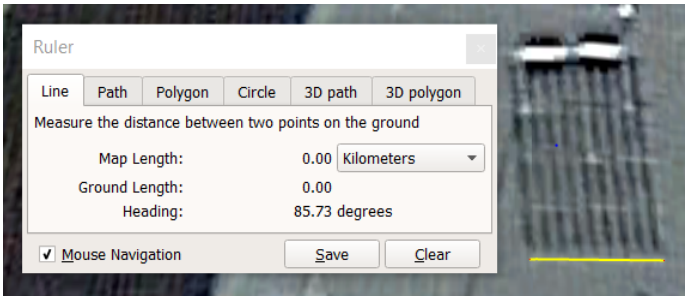

Figure 13: *The test site in Google Earth Pro and the azimuth angle of approximately 86° [43].*

The solar panels are 135.0 cm long and 20.6 cm tall, with the distance between the panels in one row being 9.9 cm. For simplicity, the distance used between the 9 rows is 39.0 cm even though the distance was slightly varying in the range of 38.6 cm – 40.0 cm. The other measurements of the solar panels, from the east side, are shown in Figure 14.

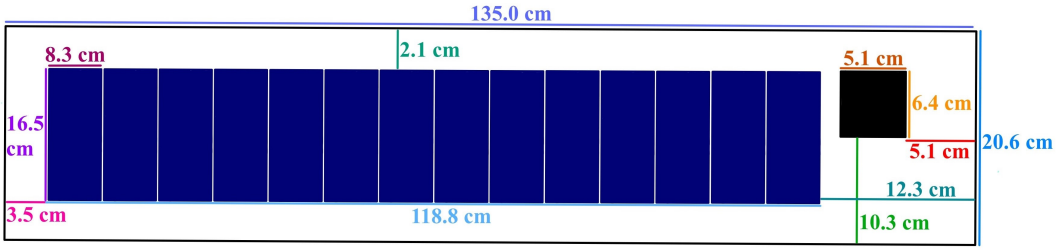

Figure 14: *Schematic illustration of a solar panel from Over Easy Solar AS on the test site taken from the rear side of the solar panel.*

The solar panels are distributed into 9 rows and each solar panel is built up by 14 half-cut solar cells connected in series, with a gap of 0.2 cm between each cell. All the cells are covered with glass. The 36 solar panels on the test site are divided into 9 optimizers as shown in Figure 15. Thus, one optimizer is connected to 4 solar panels. The 9 optimizers are connected in series into one array to an MPPT of the inverter. There are also three reference cells, described in Section 3.3, installed in the PV system. The position of the reference cells is marked with the numbers 1,2, and 3 in Figure 15.

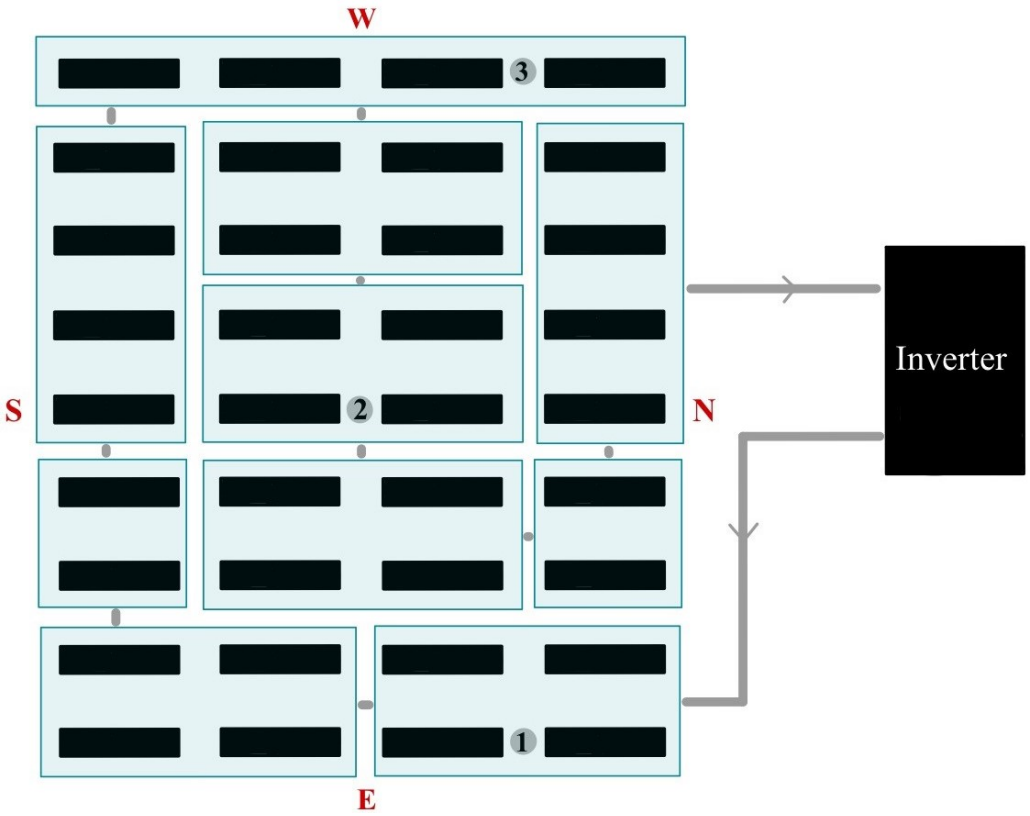

Figure 15: *Bird-view of how the solar panels on the test site are connected in relation to the 9 optimizers. These optimizers are connected in series into an MPPT of the inverter. Lastly, the position of the reference cells is marked with the numbers 1, 2, and 3.*

3.2 The 3D model in bifacial_radiance

3.2.1 Creating the 3D model and simulating the irradiance

The software used to create the 3D model and simulate the irradiance on the test site was bifacial_radiance which uses backward ray tracing. Bifacial_radiance is a python wrapper for RADIANCE and is used to simulate the irradiance on a detailed PV system as shown in Section 3.2.2. The model construction and simulation in bifacial_radiance are explained in the flowchart in Figure 16, at the bottom of this subsection.

The first step in creating the 3D model in bifacial_radiance was to define the dimensions of the solar cells and the solar panels with the glass-glass structure using the measurements mentioned in Section 3.1 and Figure 14.

For the additional virtual 3D objects such as the rails along the rows of the panels and the reference cells, materials from RADIANCE were used. These materials are defined with the color channels red, green, and blue (RGB) together with surface reflectance, roughness, and specularity. [24] The materials that were used for the different objects are shown in Table 2. All the materials used are defaults included in bifacial_radiance software.

Table 2: *Overview of the different materials used to create the 3D model.*

Object	**Material name**	**material type**	**R**	**G**	**B**	**spec**	**rough**
Glass on panels	stock glass	glass	0.96	0.96	0.96	-	-
Rails	Metal_Grey	plastic	0.43	0.448	0.465	0.5	0.5
Box	black	plastic	0.01	0.01	0.01	0	0

All the objects in the PV system on the test site consist of different materials with different properties. Therefore, the objects in the 3D model were assigned different materials to correspond to the test site as best as possible based on the default materials in bifacial_radiance. By doing this, the light simulations with RADIANCE get more accurate compared to the real light situation, which is an advantage in the ray tracing performed by RADIANCE.

The objects were created with RADIANCE by defining the material, the dimensions of the objects in x-, y-, and z-direction, and the starting position of the objects. One thing to keep in mind while creating the objects in the PV system is that bifacial_radiance automatically defines the objects according to origin (0,0,0). Therefore, a rectangle is defined with one of the corners in origin, while the origin of a sphere is defined in the center. The objects also needed to be rotated to match the orientation of the solar panels at 86°.

Weather data including measured GHI, DHI, DNI, and albedo for the defined latitude and longitude was imported into bifacial_radiance. After defining the time period to simulate the irradiance, sky files for each timestamp were created using the Perez All-Weather Sky model implemented in bifacial_radiance for the imported weather data. This is the most widely used irradiance model for modeling tilted solar systems [44]. For all timestamps, the ground albedo was selected from the imported weather file. These sky files together with the ground albedo and the scene were combined into one octree file per timestamp. [45]

The octree files were analyzed to simulate the irradiance and look at the performance of the software. To match the test site, the simulations were performed for sensors placed on the east and the west side of the reference cells marked with 1, 2, and 3 in Figure 15.

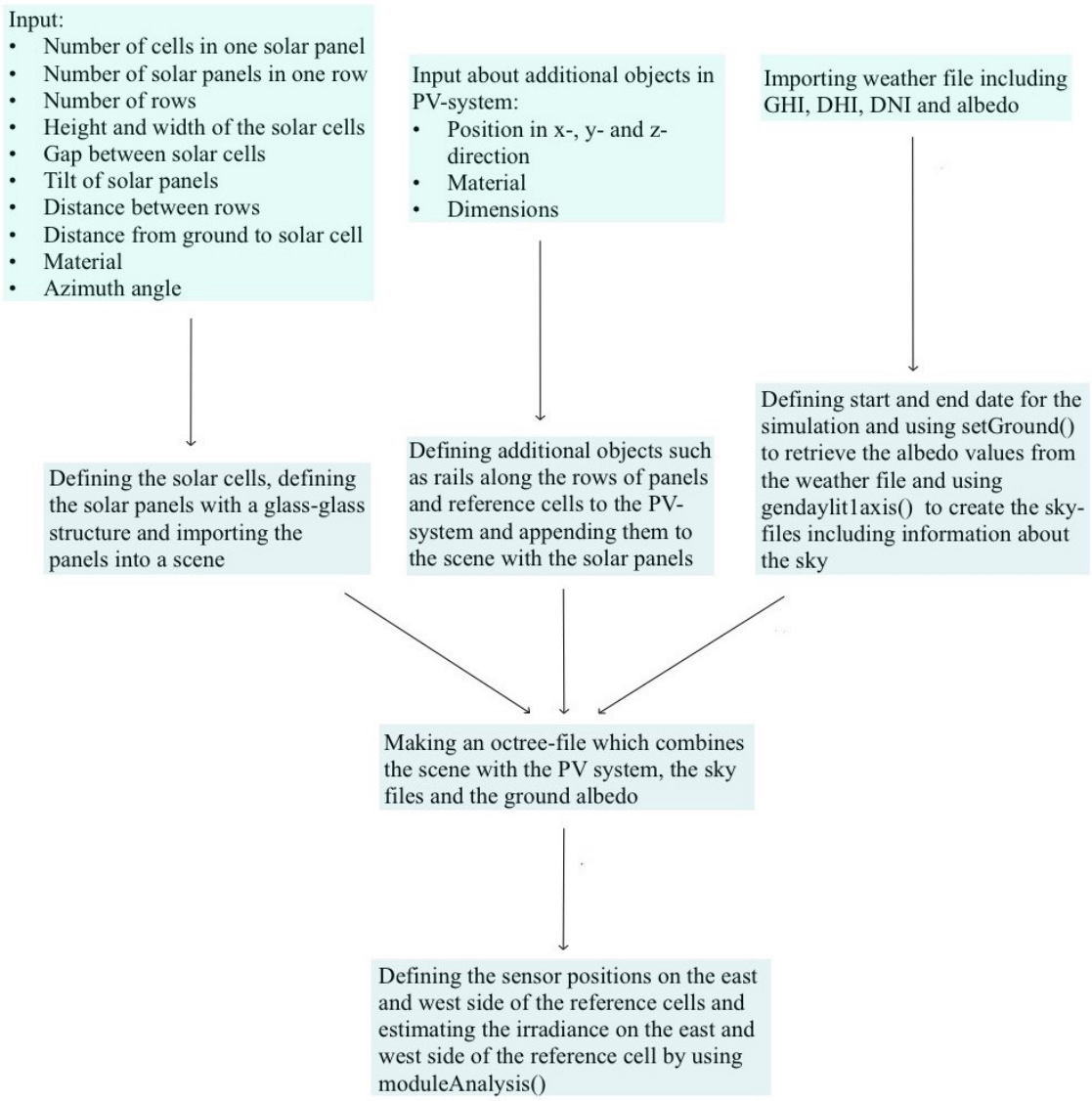

Figure 16: *Flowchart of the process in bifacial_radiance used to create the 3D model and simulate the irradiance on the PV system.*

3.2.2 The 3D model of the test site

Rvu-viewer, a functionality in RADIANCE, was used to look at the 3D model of the test site from different angles and to check the position of the defined objects in relation to the solar panels. Figure 17 – 20 shows images of the 3D model from different angles on the left with an approximately corresponding picture from the test site on the right.

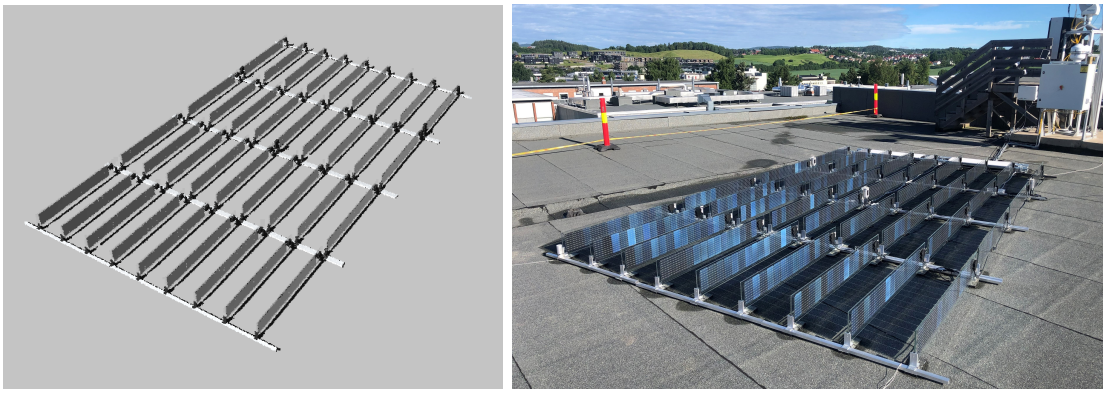

Figure 17: *The test site showed from the south-east for the 3D model (left) and the test site (right).*

Figure 18: *The test site showed from the south for the 3D model (left) and the test site (right).*

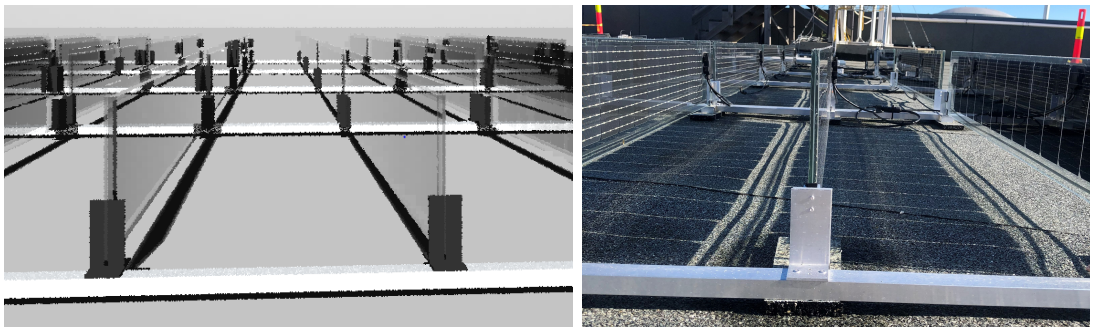

Figure 19: *A closeup of the solar panels from the south showed for the 3D model (left) and the test site (right).*

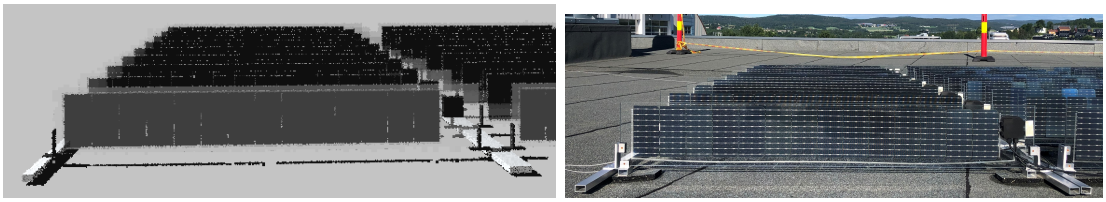

Figure 20: *The solar panels from the east side showed for the 3D model (left) and the test site (right).*

3.3 Collecting data

At the test site, there are multiple instruments for measuring different types of irradiance. The instruments were mounted in the last half of June and the beginning of July 2022. On the 30^{th} of June all the instruments were up and running except the instrument for measuring DHI which was up and running on the 6^{th} of July. Figure 21 shows the pyranometers and pyrheliometer on the test site.

a) b)

Figure 21: *On picture a is the pyranometer (1) with an installed shading ball to measure DHI and the pyranometer (2) measuring GHI. The shading ball and the pyrheliometer (3) measuring the DNI are installed on a tracker. In picture b is the two pyranometers, for albedo, that measure the upwards and downward irradiance.*

Pyranometer

If installed horizontally, the pyranometer is a radiometer that measures the global horizontal irradiance [W/m^2], GHI, with a view of 180°. By adding a shading ball to a Sun tracker, the pyranometer can be used to measure diffuse irradiance, DHI, i.e., all radiation except the irradiance around the Sun as shown in Figure 21. [17]

When it comes to the technology in pyranometers, it uses a thermoelectric or a photoelectric detector as the pyrheliometer, but a double glass is protecting the detector. [17, 46] The pyranometer reacts when there are temperature changes in a black surface due to incoming irradiance heating up the surface. This forces a voltage signal from the pyranometer that is proportional to the irradiance [47].

The pyranometers used for measuring GHI and DHI on the test site are of the type SMP10 from Kipp & Zonen. The devices are shown to the left as the numbers 1 and 2 in Figure 21, where there in front of pyranometer 1 is mounted a shading ball. This pyranometer has a spectral range of 285 nm - 2800 nm with a response time of less than 2 seconds as shown in the datasheet in Appendix A.

This is also the type of pyranometer used to measure the albedo on the test site, shown to the right in Figure 21. To measure the albedo, two pyranometers are used. Both the pyranometers are mounted horizontally, but one facing upwards and measuring the incoming irradiance, while the other one is facing downwards measuring the reflected irradiance from the ground. From the irradiance measurements, the albedo can be calculated with equation 4.

Pyrheliometer

To measure the DNI, the direct solar irradiance, pyrheliometers with a view of 5° are used to measure the irradiance [W/m^2] for a 5° angle around the Sun. This view angle is common for new pyrheliometers [46]. Since this device always needs to face the Sun, pyrheliometers are mounted to a Sun tracker that needs monitoring for accurate measurements. [17]

In the pyrheliometer, there is a sensor connected to a thermoelectric or a photoelectric detector. The pyrheliometer produces an electrical signal from the heat of the incoming irradiance. [17, 46]

For measuring the DNI on the test site studied in this thesis, a pyrheliometer of the type SHP1 from Kipp & Zonen was used. This device is shown on the left in Figure 21 as number 3. The spectral range of the pyrheliometer is 200 nm - 4000 nm with a response time of less than 5 seconds as shown in the datasheet in Appendix B.

Tracker

The tracker used for the pyrheliometer and the shading ball is of type Solys2 sun tracker from Kipp & Zonen. An advantage of this tracker is that there is an integrated GPS receiver so there is no need for a computer or software. The GPS also receives time and location data so the time adapts to local time itself. [48]

Reference cells

Reference cells are devices used to measure irradiance [W/m^2], but they work differently than a pyranometer and a pyrheliometer. A reference cell is built up like a solar cell, and therefore, gives an indication of how much irradiance the solar panels can use to generate power. In reference cells the current is measured by looking at the voltage over a resistor, then the STC is used to calibrate the voltage. [47]

The reference cells used on the test site are of the type Si-RS485TC-2T-v-MB from IMT (Ingenieurbüro Mencke & Tegtmeyer) solar [49], shown in Figure 22. These measure the incoming irradiance with a measurement uncertainty of ±2.5 % ±5 W/m^2. The spectral range of these reference cells is approximately 400 nm - 1100 nm [49], which is less than for the pyranometer and pyrheliometer due to the structure of a solar cell. They also measure the temperature which gives an indication of the temperature of the solar cells in the PV system.

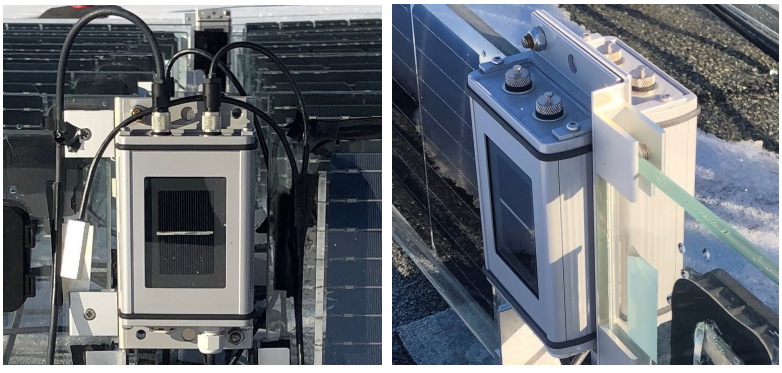

Figure 22: *The reference cells at the test site from the front (left) and the side (right).*

Inverter

The inverter used on the test site is a SolarEdge SE2200H inverter, some key information is shown in Table 3.

Table 3: *Key information from the datasheet shown in Appendix C for the SolarEdge SE2200H inverter.*

OUTPUT	
Rated AC power	2200 VA
Maximum AC power	2200 VA
AC output voltage	220/230 V
Maximum continuous output current	10 A
INPUT	
Maximum DC power	3400 W
Maximum DC input voltage	480 V
Nominal DC input voltage	380 V
Maximum inverter efficiency	99.2 %
Maximum input current	6.5 A

3.4 Quality and uncertainty of data

Precise and good measurements from the radiometers are important to ensure good quality and reliability of data. Therefore, performing quality control of the radiometers is important to detect any errors and issues with the data logger, the power, the sensors, etc. When problems with the measurements are detected early on, the risk of losing data decreases, and evaluating the uncertainty in data gets easier. [17]

The reliability of data increases with the number of installed radiometers measuring equivalent irradiance. Multiple radiometers with equivalent irradiance measurements are an advantage as the other radiometers can be used if data from one or some radiometers is lacking. Having multiple radiometers is expensive, and many sites only have one installed radiometer for each angle variation, or not any at all. [17]

The measurements retrieved from a radiometer can be affected by several factors. One is measurement uncertainty in the radiometers. Soiling such as dust and pollen, which can cover the radiometers is another factor. For a PV system in Kapp in Norway, it has been shown that losses in the annual energy production due to soiling were 0.41 % [50]. Hence, soiling is a negligible factor. On the other hand, snow was found to affect annual energy production with 2.20 % [50]. Therefore, maintenance of the radiometers is needed to prevent underestimation of the irradiance measurements. If not accounted for and maintained, these factors cause uncertainty in the data. [17] For the data used in this thesis, the measurement uncertainty has been taken into account with the method described in Section 3.4.1, but losses due to soiling and snow have been omitted.

3.4.1 Uncertainty analysis

As mentioned, measured GHI, DHI, DNI, and albedo used to simulate the irradiance on the PV system in bifacial_radiance was retrieved from the radiometers at the test site. While the measurement uncertainty in the reference cells is defined in the datasheet to be ±2.5 % ±5 W/m^2, the measurement uncertainty in the pyranometer and pyrheliometer needed to be analyzed. The uncertainty analysis used in this thesis and described in this section follows the approach outlined in Ref. [20]. The method was developed using parameters from the data sheets

and calibration sheets for the specific radiometers on the test site together with JCGM100:2008 GUM, which is a document that describes how to express the uncertainty in measurements [20].

During the uncertainty analysis, there were made some assumptions for simplification. A constant sensitivity in the pyranometer was assumed, and spectral selectivity and uncertainty in the data logger were not taken into account. Tilt response was also neglected in the analysis by assuming correctly mounted solar panels. Important data from the data sheet and the calibration certificate for the pyranometer and pyrheliometer used on the test site is defined in Table 4 with the corresponding parameter defined in the equations below. These values are defined as the maximum values. [20]

Table 4: *The technical specifications of the pyranometer Kipp&Zonen SPM10 and the pyrheliometer Kipp&Zonen SHP1 on the test site [20].*

Technical specification	**Kipp&Zonen SPM10**	**Kipp&Zonen SHP1**	**Parameter**
Sensitivity	10.91 μV/W/m^2	9.08 μV/W/m^2	S
Measurement uncertainty	1.39%	-	S
Non-stability (change/year)	$<$ 0.5 %	$<$ 0.5 %	S
Non-linearity (0-1000 W/m^2)	$<$ 0.2 %	$<$ 0.2 %	S
Directional response (up to 80° with 1000W/m^2)	$<$ 10 W/m^2	-	I
Offsets:			
$\rightarrow$ Thermal radiation (200 W/m^2)	$<$ 7 W/m^2	-	I
$\rightarrow$ Temperature dependence (5 K/h)	$<$ 2 W/m^2	1 W/m^2	I
Temperature dependence:			
$\rightarrow$ Temperature range	$<$ 1 % (-20 to 50°C)	0.5 % (-30 to 60°C)	S
$\rightarrow$ Temperature range	$<$ 2 % (-40 to 70°C)	1 % (-40 to 70°C)	S

For the pyranometer and pyrheliometer used at the test site, the calibration certification states a coverage factor of k = 2. This means an uncertainty with a confidence interval of 5 % and 2 standard deviations. The uncertainty in each component needed to be converted into the limits of ISO9060, which is a document including the classification and specification for instruments that measure GHI and DHI. Also, an a-priori distribution was used to calculate the standard uncertainty for the components. Since the values in Table 4 are the maximum values, a rectangular distribution was applied to the data. [20] The standard uncertainty, u, for the rectangular and normal distribution is shown in defined in equation 18 and 19, respectively

$$u = \frac{a}{\sqrt{3}}, \tag{18}$$

$$u = \frac{a}{3}, \tag{19}$$

where a is the individual component uncertainty. To determine the measurement uncertainty, a Type B evaluation of standard uncertainty from JCGM 100:2008 GUM was used [20]. For this, the measured solar irradiance I [W/m^2] was calculated as followed

$$I = \frac{V}{S}, \tag{20}$$

where S is the sensitivity [μV/W/m^2] of the instrument from the calibration certificate and V is the voltage [V] of the pyranometer.

The uncertainty analysis of the irradiance measurements was done in two parts. The first one was looking at the primary variable uncertainty, while the second part consisted of looking at the direct uncertainty for the measured solar irradiance. [20] The standard uncertainty was then defined by looking at the measured solar irradiance, I, and taking the sum of all the sources of uncertainty as shown in equation 21

$$u_c(I) = \sqrt{\sum_k u^2(I) + \left(\frac{\partial I}{\partial V}\right)^2 u^2(V) + \left(\frac{\partial I}{\partial S}\right)^2 u^2(S)}. \tag{21}$$

Here the standard deviation of I, S and V is defined by $u^2(I)$, $u^2(S)$ and $u^2(V)$. $(\partial I/\partial V)^2$ and $(\partial I/\partial S)^2$ are the sensitivity coefficients for the parameters V and S, respectively. The standard uncertainty of these two parameters was calculated by looking at the sum of the uncertainty sources i and j as shown in equation 22 and 23 [20]

$$u(S) = \sqrt{\sum_i u_i^2(S)}, \tag{22}$$

$$u(V) = \sqrt{\sum_j u_j^2(V)}. \tag{23}$$

Lastly, the expanded uncertainty (δ) for the irradiance measurements was calculated by looking at the coverage factor, k, and the standard uncertainty ($u_c(I)$) as shown in equation 24

$$\delta = k u_c(I). \tag{24}$$

Since the albedo at the test site is measured with two pyranometers, the same method as described above was used to calculate the uncertainty in the incoming and reflected irradiance. When assuming the uncertainty in incoming and reflected irradiance to be random and independent [51], the albedo uncertainty ($\delta\alpha$) was estimated with equation 25

$$\delta\alpha = \frac{1}{I_{up}}\sqrt{\left(\frac{I_{down}}{I_{up}}\delta I_{up}\right)^2 + \delta I_{down}^2}, \tag{25}$$

where δI_{up} and δI_{down} are the uncertainty in the incoming and reflected irradiance measured by the pyranometers facing upwards and downwards, respectively.

3.5 Performance of the 3D model

3.5.1 Simulating the irradiance

Simulating the irradiance with the 3D model was done by implementing a weather file including GHI, DNI, DHI, and albedo measurements from the test site with

the column names used in a TMY (Typical Meteorological Year) file. The reason for TMY is that bifacial_radiance expects the format of the weather file to be TMY or EPW (EnergyPlus). The header of the weather file includes information about the location such as latitude, longitude, altitude, and timezone.

Because the radiometers were installed in the summer of 2022, a full year of data had not yet been documented. Also, due to a lightning strike close to the test site on the 17^{th} of August 2022, some data was missing on a 5-minute interval until October. Therefore, the time periods with measured data in 2022 were the 6^{th} of July – the 16^{th} of August and the 6^{th} of October – the 31^{st} of December. Since bifacial_radiance expects a full year of data, the time periods with no measured data were filled with clear-sky data. By implementing data from the test site into bifacial_radiance, the simulated irradiance could be compared to measured irradiance from the reference cells on the test site. The simulations were repeated for a period in 2023. Since the measured DNI were moved to the same logger as GHI, DHI, and albedo in the middle of January 2023, data for the period the 18^{th} of January to the 31^{st} of March was implemented into the weather file.

Validating the 3D model was carried out by simulating the irradiance on an hourly interval for selected days. If not defined, bifacial_radiance expects that the Sun position for each timestamp in the important weather file is right-labeled, i.e. with a shift of -30 minutes so that 12:00 is the 11:30 Sun position. Hence, the weather file imported into bifacial_radiance with the measured data, included instantaneous values for the timestamps 11:30, 12:30, 13:30, etc., and the timestamp was converted to 12:00, 13:00, 14:00, etc. As the measured data had a 5-minute interval, the instantaneous values symbolizing the data for an hour were based on data for 5 minutes. Instantaneous values were used to eliminate the chance of using the wrong Sun position for parts of the data.

Simulating the irradiance on an hourly interval with bifacial_radiance is time-consuming due to the complex and detailed model, and backward ray tracing. Thus, simulating the irradiance for a longer period of time on an hourly interval is not time efficient. Instead, a cumulative sky was created in bifacial_radiance to simulate the irradiance for a longer period as the computation time is reduced. The cumulative sky was created by using the Perez sky model to estimate the irradiance in the center of the 145 patches the sky dome is divided into. This was done for all timestamps on an hourly interval before the irradiance distribution was aggregated to one value for the period simulated. [24] This method is also used when simulating for example monthly and annual irradiance.

Due to the lightning strike on the 17^{th} of August 2022 and that the DNI was moved to the same logger as GHI, DHI, and albedo in the middle of January 2023, there were specific periods where a cumulative sky was used to simulate the irradiance. These are listed below.

- The 6^{th} – 31^{st} of July 2022
- The 1^{st} – 16^{th} of August 2022
- The 6^{th} – 31^{st} of October 2022
- The 1^{st} – 30^{th} of November 2022
- The 1^{st} – 31^{st} of December 2022
- The 18^{th} – 31^{st} of January 2023
- The 1^{st} – 28^{th} of February 2023
- The 1^{st} – 31^{st} of March 2023

3.5.2 Angle of incidence

Pvilb is a software for studying the performance of PV systems and contributes with many implementations to simulate the generated power and energy from solar systems. There are algorithms for the irradiance on a clear-sky day, solar positions, bifacial systems, DC power, and inverter models to mention something. [31]

The angle of incidence (AOI), the angle between the direct incoming irradiance and the surface of a solar panel, causes losses in the received irradiance on the solar panel. For the solar panels from Over Easy Solar AS with a glass-glass structure, such losses can be caused by reflection and absorption when the irradiance reaches the glass. These losses are not taken into account by bifacial_radiance, and therefore, pvlib was used to study the impact losses due to AOI has on the simulated irradiance. The process, and functions used from pvlib are shown in the flowchart in Figure 23.

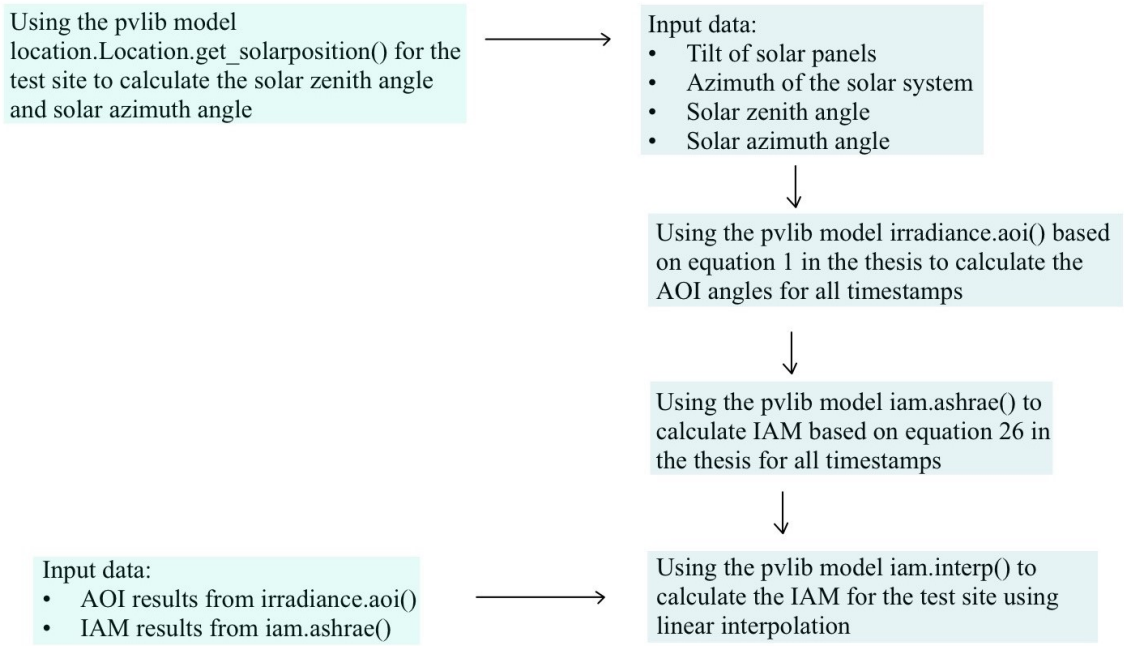

Figure 23: *Flowchart of the process of calculating the incident angle modifier (IAM) by using pvlib to correct the simulated irradiance for losses due to angle of incidence (AOI).*

With the model irradiance.aoi from v.0.9.5 of pvlib [31], the AOI of a PV system was estimated. Then the AOI could be used to retrieve the corresponding incident angle modifier (IAM) with the model transmission model from American Society of Heating, Refrigeration, and Air Conditioning Engineers (ASHRAE), iam.ashrae from v.0.9.5 of pvlib [31] based on equation 26

$$IAM = 1 - b(sec(AOI)) - 1). \tag{26}$$

In this equation b is an adjustment parameter used to adjust IAM as a function of AOI. [31] Then the simulated irradiance from bifacial_radiance could be adjusted with the IAM factor.

With these models, the IAM factor for AOI angles below 90° are retrieved, but for bifacial solar panels mounted vertically facing east/west, the panels can receive

diffuse irradiance even though they do not receive direct irradiance. Hence, there can be losses when the diffuse irradiance reaches the glass of the solar panels as well. Consequently, a linear interpolation was used to retrieve IAM factors for the timestamps where the front and the rear side of the solar panel only received diffuse irradiance.

3.6 Simulating the power

To simulate the generated power from the test site, models implemented in pvlib were used. A flowchart of the process and models used to simulate the DC and AC power generated from the PV system is shown in Figure 24.

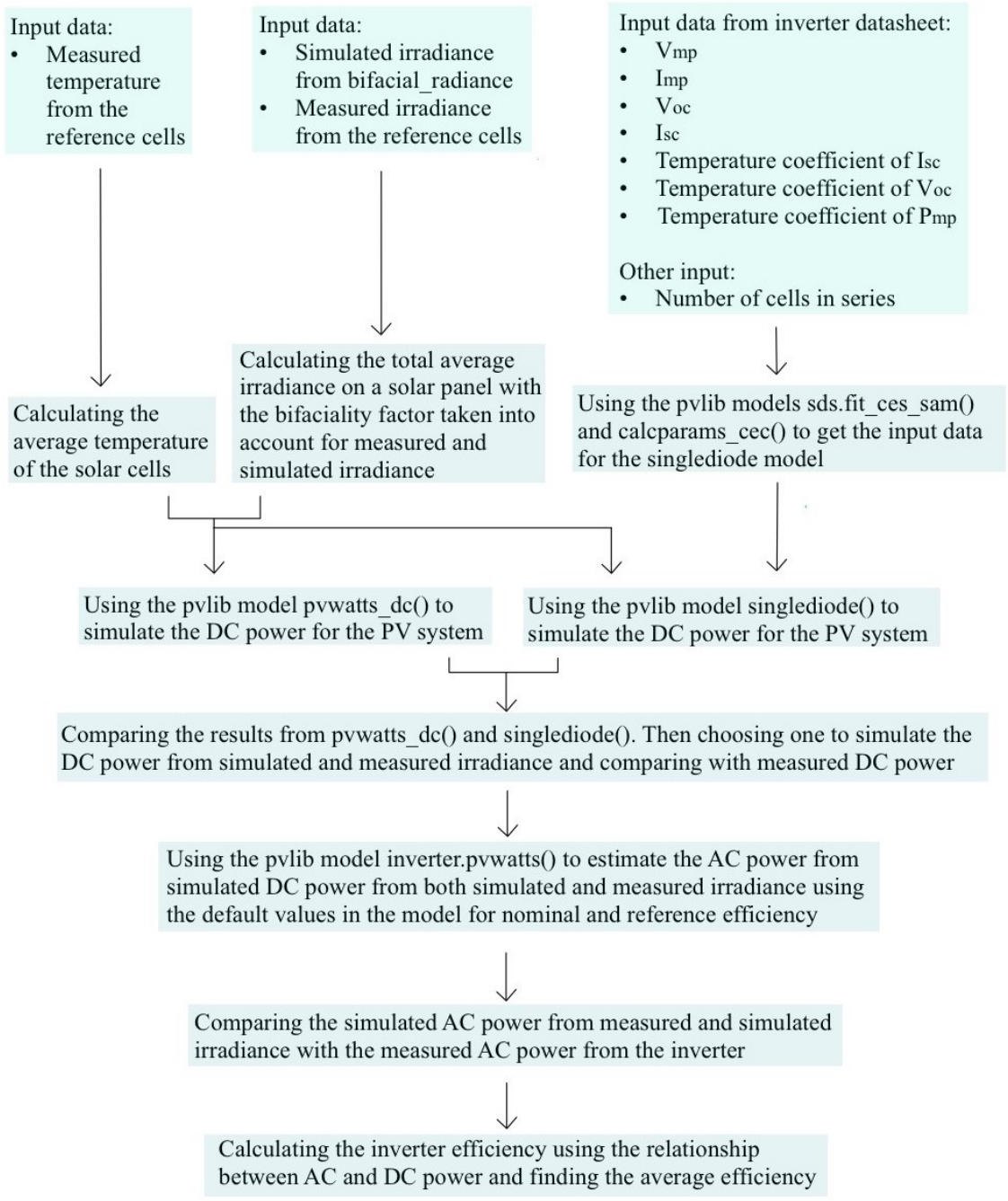

Figure 24: *Flowchart of the process of estimating the power production from simulated irradiance in bifacial_radiance and measured irradiance.*

From pvlib v.0.9.5 [31] the two models pvwatts_dc [30] and singlediode were tested to simulate the DC power before choosing one to simulate the DC power for all the days. The model pvwatts_dc from NREL is based on equation 5 while the singlediode model is based on the single diode equation shown in equation 6.

For both models, measured temperatures from the reference cells were used to estimate the average temperature for the solar cells on the test site, assuming equal temperatures on the front and rear side. For both measured irradiance and simulated irradiance from bifacial_radiance, the total average irradiance for one solar panel, with the bifaciality factor taken into account was calculated. For simplification, it was assumed that all solar cells on the test side had the same temperature and that all the solar panels received the same irradiance.

After selecting one model, the DC power was converted to AC power by using NREL's inverter model inverter.pvwatts, based on equation 11, from v.0.9.5 of pvlib [31]. For the variables η_{nom} and η_{ref} the default values of 96.00 % and 96.37 % were used, respectively. The relationship between AC and DC power was then used to estimate the inverter efficiency.

4 Results & discussion

In the following section, the results from performed analyses are presented together with a discussion of the findings. First, the simulated irradiance using the 3D model on a daily level and a cumulative sky compared to measured irradiance are presented for selected days and months. The results are discussed on an ongoing basis and possible factors that may affect simulated and measured irradiance are addressed. In the end, the simulated power and energy from the test site when using simulated and measured irradiance are presented and discussed for selected days and months, respectively.

4.1 Simulated irradiance compared to measured irradiance

The 3D model in bifacial_radiance was used to simulate the irradiance for clear-sky days, overcast days, and days with varying weather. Then the results were compared with measured irradiance from the reference cells on the test site. Four days were simulated for each type of irradiance condition to cover all seasons in Norway. The results for all three reference cell positions in the test site are shown in Appendix E.

In Section 4.1.1 – 4.1.6, the simulated irradiance compared to the measured irradiance for selected days and months is shown and discussed. The measurement uncertainty in simulated and measured irradiance is shown as well. The measurement uncertainty in simulated irradiance due to the input values GHI, DHI, DNI, and albedo has been estimated with the method described in Section 3.4.1, while the measurement uncertainty for the measured irradiance from the reference cells is defined to be ±2.5 % ±5 W/m^2, mentioned in Section 3.4.1 as well.

4.1.1 Time interval in data used to simulate the irradiance

Two selected days in 2022 are the 12th of August and the 23rd of December. Apart from the variation in GHI before 7:00 AM and after 5:00 PM the 12th of August and before 9:00 AM and after 1:30 PM the 23rd of December, these days are relatively clear-sky days as shown in Figure 25.

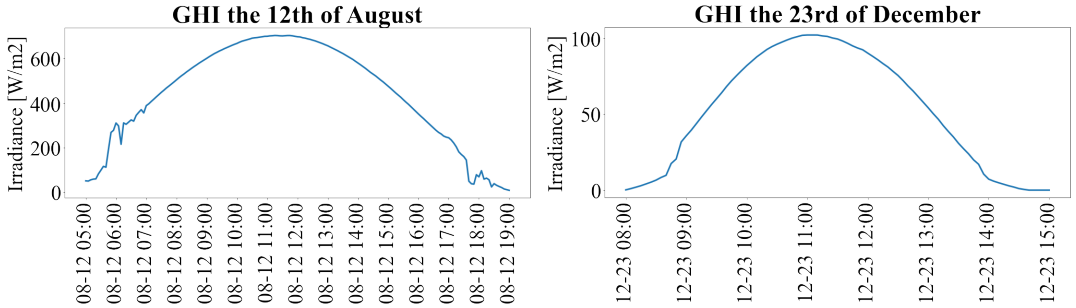

Figure 25: *GHI for the 12th of August and the 23rd of December 2022. As the irradiance is higher during the summer, the scale along the y-axis of the two graphs is different.*

As simulating the irradiance for a day in bifacial_radiance is time-consuming, the simulations were performed using an hourly interval with instantaneous values for GHI, DHI, DNI, and albedo as described in Section 3.5. Depending on the length of

the day, simulating one day took approximately 40 minutes. Simulated irradiance compared to measured irradiance for reference cells 1 and 2, with measurement uncertainty, the 12^{th} of August and the 23^{rd} of December are shown in Figure 26.

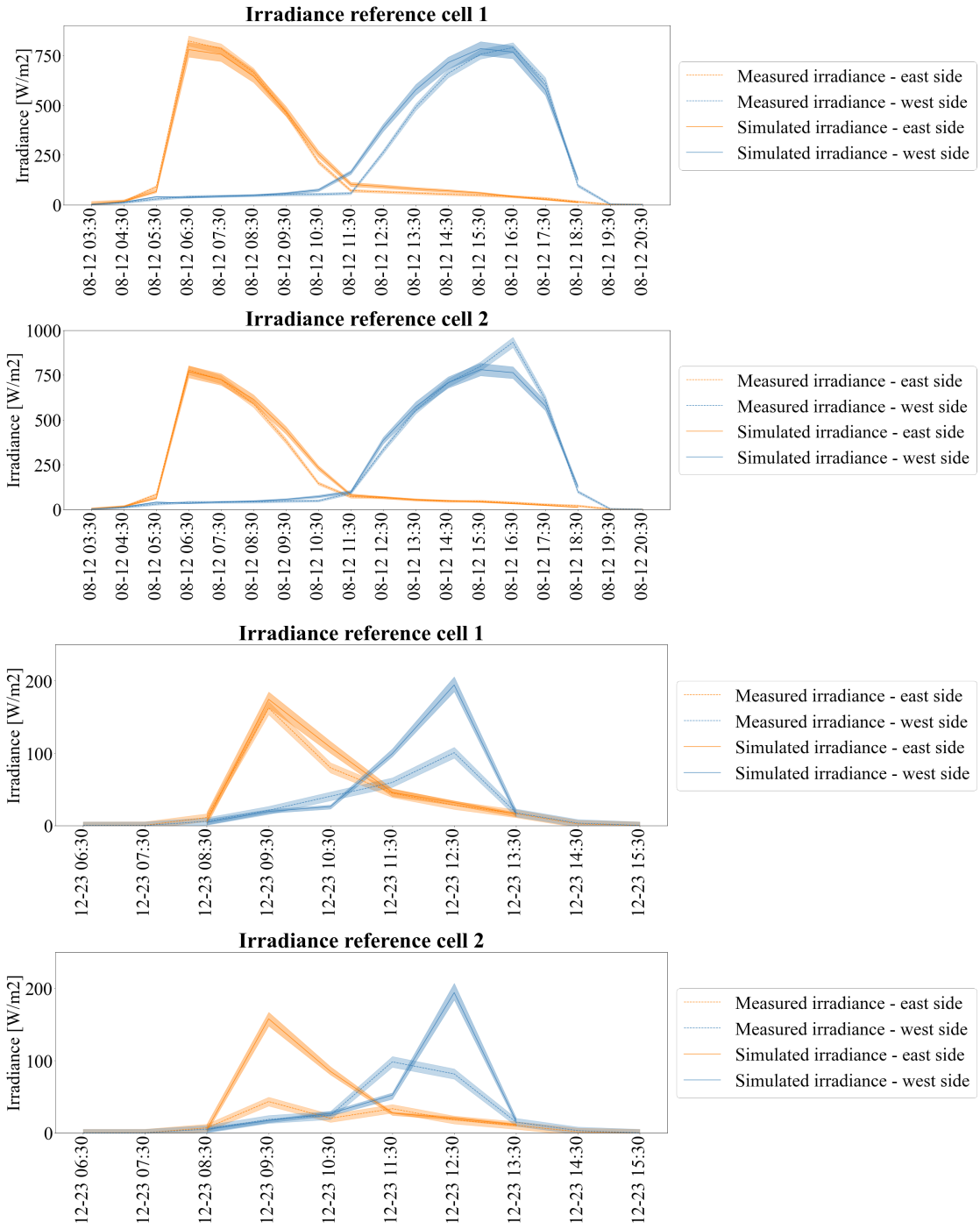

Figure 26: *Simulated and measured irradiance for reference cells 1 and 2 the* 12^{th} *of August and the* 23^{rd} *of December 2022. The measurement uncertainty in measured and simulated irradiance is displayed as a shaded area.*

As the figure shows, for the 12^{th} of August there is good compliance between the measured and simulated irradiance, but there are areas where the graphs are outside the uncertainty area of one another. One example is between 10:30 AM and 3:30 PM for reference cell 1. Also, for reference cell 2 there is a spike in the measured irradiance at 4:30 PM. This spike may be caused by direct reflection from the aluminum rails along the roof, people working or walking around the

test site, or objects brought to the roof temporarily. This has not been taken into account in the simulations. For the 23^{rd} of December on the other hand, there is more deviation between the measured and simulated irradiance compared to the 12^{th} of August, and the simulated irradiance is overestimated. The exception is the east side of reference cell 1 where the compliance is good. As the irradiance simulated with bifacial_radiance is the result of instantaneous values on an hourly interval, a simulation for these two days was performed with a 5-minute interval in data to see if the timestamp could explain some of the deviations in Figure 26. The results are shown in Figure 27.

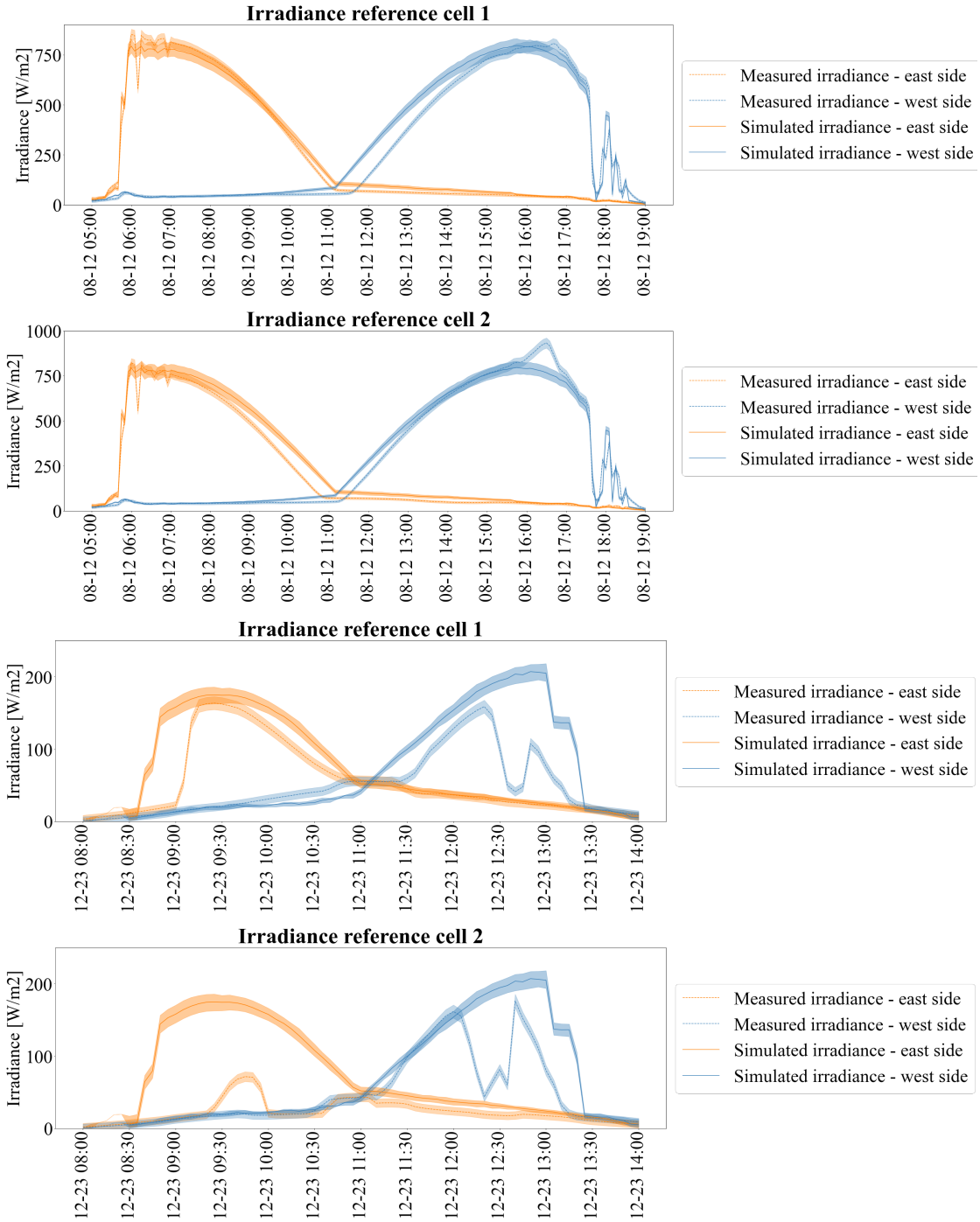

Figure 27: *Simulated and measured irradiance for reference cells 1 and 2 the 12^{th} of August and the 23^{rd} of December 2022 on a 5-minute interval. The measurement uncertainty in measured and simulated irradiance is displayed as a shaded area.*

For the 12^{th} of August, the trends between the simulated irradiance at the hourly interval and 5-minute interval match well as Figure 26 and 27 show. The timestamps in the middle of the day where the simulated and measured irradiance is outside the uncertainty of one another happen at the same time for both hourly and 5-minute intervals. The exception is before 7:00 AM and after 5:00 PM where the use of hourly intervals does not catch the variation in irradiance. These variations in irradiance are captured using a 5-minute interval. Also, the spike at 4:30 PM for reference cell 2, is captured for both hourly and 5-minute intervals. This indicates that bifacial_radiance has the strength to deliver accurate estimations of the irradiance regardless of the weather if provided with accurate input data.

For the 23^{rd} of December, there are more deviations even though the trends between hourly and 5-minute intervals on the west side seem to match. For reference cell 1, the simulation starts half an hour before the measured data at 8:30 AM using a 5-minute interval, and in the afternoon the measured data is more unstable than the simulated irradiance. Hence, the timestamp affects the captured details in irradiance, but it does not explain the deviations shown in Figure 26 and 27. As for the 12^{th} of August, it is clear that the hourly interval in input data does not catch all variations in irradiance for the 23^{rd} of December. Still, it is time-consuming to run many simulations at a 5-minute interval as simulating one day takes several hours. Thus, an hourly interval was chosen for the rest of the simulated days. Regardless, the simulated irradiance is compared to measured data with the corresponding timestamp. Therefore, hourly intervals should give an indication of the correspondence between measured and simulated irradiance when using bifacial_radiance.

4.1.2 Shading on the test site

The instability in GHI in the morning and the afternoon in Figure 25 seem to correspond with the instability in the irradiance as shown in Figure 27. The exception is after 12:00 PM the 23^{rd} of December, where there is a deviation in simulated and measured irradiance even though it is clear-sky until approximately 2:00 PM. The cause of this deviation was not established, but as there is better compliance between simulated and measured irradiance for the 12^{th} of August, shading in the PV system may be a factor affecting the deviation between simulated and measured irradiance. The shading can be due to objects north and south of the PV system at the test site as shown in Figure 28.

Figure 28: *Objects north (left) and south (right) of the PV system.*

As the 3D model has been simplified to only include the PV system and the rails along the roof as shown in Figure 17 – 20, possible shading from the objects surrounding the PV system was neglected. The objects north of the PV system probably won't cause shading on the test site and the reference cells significantly, and hence won't affect the measured irradiance. On the other hand, the objects to the south may cause shading on the PV system and the reference cells, especially in the winter and the 23^{rd} of December. The reason is that the low altitude of the Sun may cause larger shadows from the objects than it does during the summer. This is documented by Figure 29 which shows shading on the PV system and the reference cells due to the surrounding objects in the south. Objects inside the PV system, such as the solar panels, also seem to cause shading on the reference cells. As the surrounding objects were neglected in the 3D model, the reference cells in the model won't experience the same shading as the test site, but they can suffer from shading due to the solar panels. This may explain the overestimating in simulated irradiance compared to the measured irradiance for the 23^{rd} of December, and why the simulated irradiance starts to increase an hour before the measured irradiance at 10:30 AM for reference cell 1 the 12^{th} of August on the west side in Figure 26. For the 23^{rd} of December, shading may also explain why the simulated irradiance starts half an hour before the measured irradiance using a 5-minute interval for reference cell 1 on the east side and some of the deviations during the day.

Figure 29: *A picture of the test site taken by a webcam from the north the* 23^{rd} *of December 2022 at 11:00 AM. The position of the reference cells is marked with the numbers 1,2 and 3 corresponding to Figure 15.*

4.1.3 Snow on the test site

The main factor that may explain the deviation shown for the 23^{rd} of December is snow. As shown in Figure 29 there is much snow on the roof which covers the solar panels and seem to cover the reference cells marked with number 1,2, and 3. This results in a lower measured irradiance from the reference cells than from the radiometers as they are mounted higher above the ground as Figure 28 shows. Still, the radiometers may have some snow coverage, but not as much as the test site. Even though the 23^{rd} of December is a clear-sky day, if the snow did not melt or just to some degree, simulated irradiance might have been compared to underestimated measured irradiance due to snow coverage, and hence explain the large deviation this day. In addition, the snow might cause additional shading to the PV system.

Another day where the irradiance has been simulated and there was snow on the test site, but not enough snow to cover the reference cells is the 22^{nd} of February 2023. The simulated irradiance compared to the measured irradiance for the 22^{nd} of February, an overcast day, is shown in Figure 30.

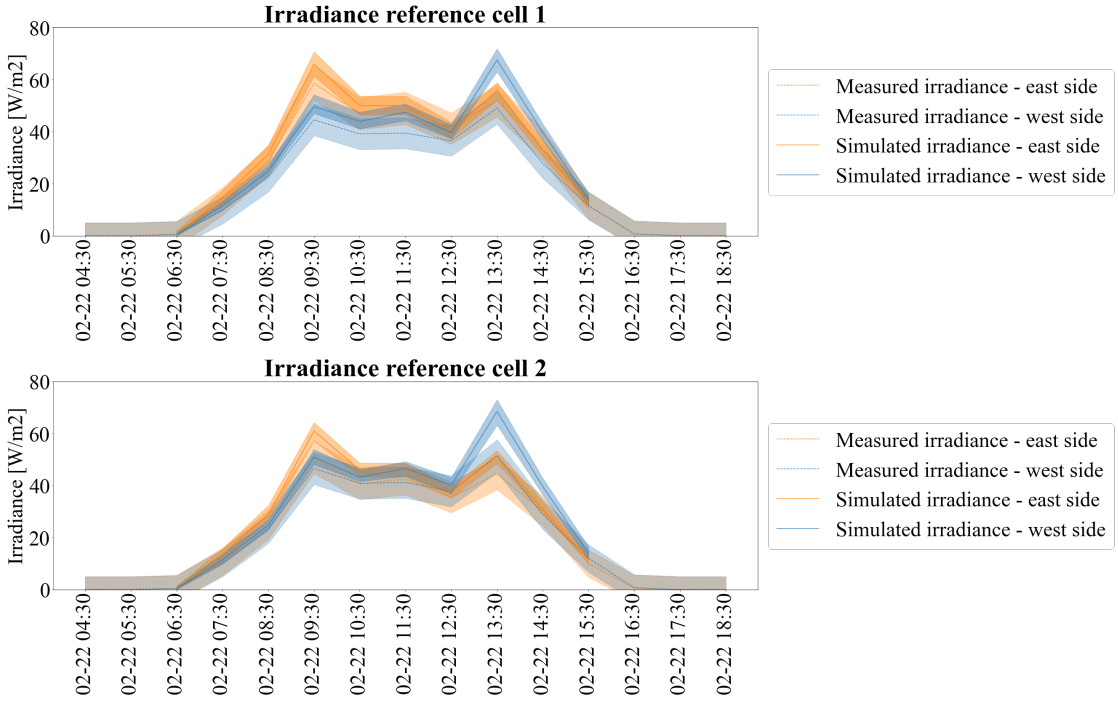

Figure 30: *Simulated and measured irradiance for reference cells 1 and 2 the 22^{nd} of February 2023. The measurement uncertainty in measured and simulated irradiance is displayed as a shaded area.*

From the website SeNorge [52], there was approximately 2 cm of snow at Kjeller where the test site is located the 22^{nd} of February. This is less than the 23^{rd} of February, which is shown in Figure 31. Hence, 2 cm of snow is not enough to cover the reference cells, eliminating the risk of underestimated measured irradiance from the reference cells.

Figure 31: *A picture of the test site taken by a webcam from the north the 23^{rd} of February 2023 at 10:58 AM.*

As Figure 30 shows, compared to the 23^{rd} of December, the 22^{nd} of February has almost no deviation between simulated and measured irradiance. It seems that simulated and measured irradiance is inside the uncertainty of one another at all timestamps except for the west side between 12.30 PM and 2:30 PM. In other words, the thin layer of snow this day probably did not affect the measured irradiance. Hence, if not taken into account, the uncertainty in the simulated irradiance from bifacial_radiance increases as soon as snow covers the solar panels and the reference cells, but not the radiometers.

4.1.4 Factors when creating the 3D model affecting the irradiance

As discussed in Section 4.1.2 and 4.1.3, shading and snow are factors that may affect the deviation between simulated and measured irradiance significantly, especially as the objects surrounding the test site were not implemented in the 3D model. Still, there may be more factors affecting the simulated irradiance and hence, cause deviation between simulated and measured irradiance.

The deviations between simulated and measured irradiance may be caused by the position of the instruments measuring the irradiance. While the measured irradiance has been retrieved from the reference cells in the PV system as shown in Figure 29, the irradiance used as input to simulate the irradiance with the 3D model has been retrieved from the radiometers north of the PV system as shown in Figure 28. As this figure show, the radiometers are mounted higher above the roof than the reference cells. Thus, it is possible that the reference cells suffer from shading due to surrounding objects, while these shadows may not affect the pyranometers and pyrheliometers as much, and consequently the input irradiance to bifacial_radiance. Still, the reference cells in the 3D model may be shaded for some timestamps, but maybe not at the same time as the reference cells on the test site due to the surrounding objects.

The reference cells in the 3D model were placed to correspond to the positions at the test site. In the 3D model, the reference cells are symbolized by black boxes, and the sensors to simulate the irradiance have been placed a small distance from the box on the west and east side marked with the 2 and 3 in Figure 32, respectively.

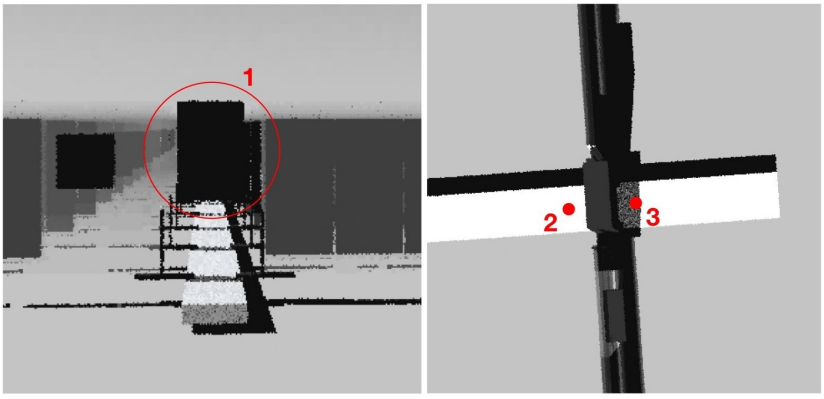

Figure 32: *Illustration of a reference cell (1) in the 3D model and a bird-view showing the position of the sensors to the west (2) and to the east (3) of the reference cell.*

The reference cells in the 3D model have the same dimensions as the ones on the test site, thus the sensors in the 3D model are not placed inside the dimensions of

the reference cells on the test site. Also, there may be an uncertainty in the exact placement of the sensors in the 3D model compared to the test site according to the height above the ground and in the north/south direction. This, in addition to the objects surrounding the test site, can be a reason for the deviation between measured and simulated irradiance because the reference cells on the test site and the sensors in the model experience shading on different timestamps. An example is the 12^{th} of August, in Figure 26 when the simulated irradiance on the east side starts to increase at 10:30 AM, but the measured irradiance starts approximately an hour later. Still, the simulated and measured irradiance match better for other days such as the 22^{nd} of February.

Other possible explanations for the deviation between measured and simulated irradiance can be the materials used while creating the 3D model. As mentioned, the reference cells are symbolized by black boxes in the model, but the reference cells on the test site are not black, as they are built like solar cells as shown in Figure 22. In other words, the materials in the model are not identical to the materials on the test site when it comes to color, material properties, and albedo. This may explain possible reflection from objects inside and surrounding the test site, such as the spike around 4:30 PM for reference cell 2 on the 12^{th} of August in Figure 26. These reflections may not be caught by the 3D model. Still, as mentioned this spike may also be caught by reflection from objects or people on the roof as well.

For 2022, the DNI measurements were retrieved from another logger than GHI, DHI, and albedo. Even though the timestamp in the indexes matches, there may be some differences in exactly when the data is logged and how they are aggregated to get irradiance on 5-minute intervals. Small differences such as these may cause small deviations in the light generated in bifacial_radiance compared to the real world which can give some deviations in the results. Since DNI were moved to the same logger as GHI, DHI, and albedo in the middle of January 2023 this uncertainty was eliminated, therefore, the deviation in the results for the 22^{nd} of February in Figure 30 cannot be explained by how data was retrieved.

There are also physical differences between the light situation used in the 3D model and the light in the real world. Even though the light in bifacial_radiance is created from measured values for the correct latitude and longitude, it will not be exactly the same due to the Perez sky model used to create the sky in the model. Perez is one of the commonly used transposition models, and it has been found that Perez is one of the models with the overall lowest uncertainty at Kjeller [53]. The relative root mean biased deviation and the mean squared deviation using the Perez transposition model at Kjeller have been found to be 2.0 % and 8.6 %, respectively [53]. Still, how the Perez transposition model works for vertically mounted PV systems in the Nordic climate have not been studied in this thesis.

4.1.5 Evaluation of the 3D model for daily simulated irradiance

Overall, with the simplifications in materials and the included objects in the model, bifacial_radiance simulates the irradiance with high accuracy as it does most of the day for the 12^{th} of August and the 22^{nd} of February. Nonetheless, there are some deviations for most days at some timestamps such as between 10:30 AM and 2:30 PM on the east side for the 12^{th} of August. On the other hand, there are days

with larger deviations in the results, hence, the uncertainty in simulated irradiance increases when there is snow and shading from surrounding objects on the test site as these factors are not included in the 3D model. To retrieve more accurate results for all seasons and irradiance conditions, the 3D model could have been more detailed by for example adding the surrounding objects for more accurate shading in the 3D model, and ensuring that the materials in the model correspond better to the test site. However, the results with the simplified 3D model give a rough estimate of the expected irradiance for a PV system when simulated with bifacial_radiance. To further develop the 3D model and use an hourly interval to simulate the irradiance for a longer period of time is time-consuming and not efficient.

4.1.6 Aggregated simulation using cumulative sky

As described in Section 3.5, a cumulative sky was created in bifacial_radiance to get an overview of the simulated irradiance for a longer period of time as this method is less time-consuming. The irradiance was simulated for the time periods listed in Section 3.5 and the results are shown in Figure 33 for reference cell 1, with the measurement uncertainty shown as error bars. For reference cells 1, 2, and 3, see Appendix E.

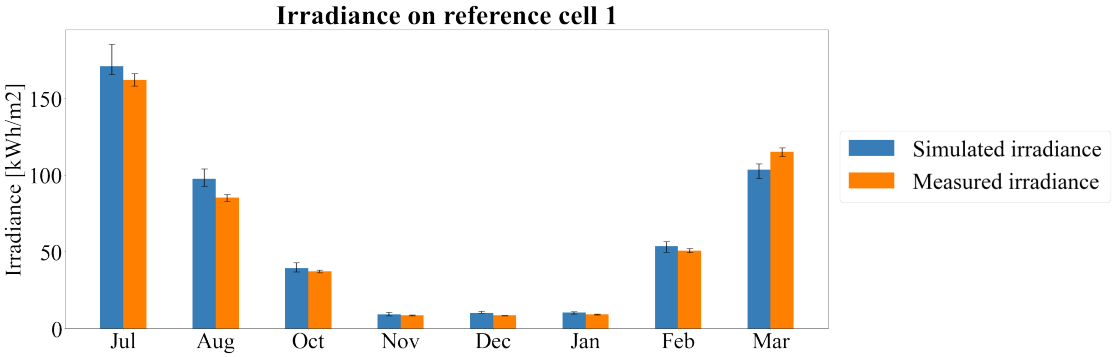

Figure 33: *Simulated irradiance compared to measured irradiance with measurement uncertainty using a cumulative sky for reference cell 1.*

As Figure 33 shows, the simulated irradiance is overestimated for all months except March where the simulated irradiance is underestimated. Still, for most months, the results are within the uncertainty of one another. As the deviation between simulated and measured irradiance varies between the months, the percentage difference between simulated and measured irradiance was calculated and is shown in Table 5. In this table, the measurement uncertainty has been omitted. Hence, there is a possibility that the percentage difference may be higher or lower than what is shown in Table 5.

Table 5: *The percentage difference between simulated and measured irradiance for reference cell 1 when using a cumulative sky.*

	Jul	**Aug**	**Oct**	**Nov**	**Dec**	**Jan**	**Feb**	**Mar**
Deviation	5.23 %	13.53 %	5.06 %	6.45 %	16.54 %	11.67 %	5.68 %	10.67 %

From Table 5, the percentage difference between simulated and measured irradiance varies in the range of 5.06 % – 16.54 %, with the lowest difference in October

and the largest difference in December. Factors such as shading, snow, materials, and positioning of the reference cells, as discussed in Section 4.1.2 – 4.1.4, are factors that may affect the simulated irradiance using a cumulative sky as the same 3D model has been used. These factors can therefore be some of the explanations for the overestimating and underestimating shown in Figure 33 and in Table 5.

A higher deviation between simulated and measured irradiance during the winter is expected as snow may cover the test site and the reference cells. The higher deviation in August, on the other hand, stands out from July and October. In addition to the factors discussed in Section 4.1.2 – 4.1.4, some of the solar panels on the test site were replaced during the summer of 2022. Hence, people and temporary objects may have been on the roof during August causing shading on the test site or direct reflection captured by the radiometers or the reference cells. Still, why the deviation is higher this month has not been established during the work of this thesis.

When using a cumulative sky, as for simulating a day, the 3D model and bifacial_radiance give a rough estimate of the expected irradiance to a PV system compared to the measured irradiance when considering that the factors such as additional shading, snow, materials, etc. have not been taken into account. Overall, for a vertical PV system in the Nordic climate, bifacial_radiance seems to work for all seasons when using a cumulative sky, but the uncertainty in the simulated irradiance increases when snow covers the PV system as this is not captured in the input data, and by the software. Still, the results between measured and simulated irradiance could have been more accurate if the factors in Section 4.1.2 – 4.1.4 had been considered when developing the 3D model.

4.2 The impact of selected factors on simulated irradiance

4.2.1 Orientation of the 3D model

When creating the 3D model, the orientation of the PV system was set to 90°, directly towards the east. Simulating the irradiance with this orientation gave good results for the summer, but in the winter the deviation between simulated and measured irradiance increased. Therefore, to get a 3D model corresponding with the test site, the orientation of the test site was investigated.

First, a compass was used to find the orientation of the PV system on the test site. In most positions, the compass showed 78°, but there were some exceptions where the compass showed 89° and 101°. There are many objects on the roof where the test site is mounted, and there are direct currents generated from the solar systems that may have affected the orientation shown on the compass. Consequently, there is an uncertainty in the compass measurements. Coincidentally, Google Earth Pro [43] had been updated so that the test site was shown on the roof. Hence, using the tools in Google Earth Pro gave an orientation of approximately 86° according to the north, as shown in Figure 13.

Simulating the irradiance was performed for orientations at 90°, 86°, and 78° for the 12^{th} of August 2022 and the 26^{th} of January 2023. The simulated irradiance compared to the measured irradiance for reference cell 1 at the test site is shown in Figure 34. For reference cells 1, 2, and 3 see Appendix F.

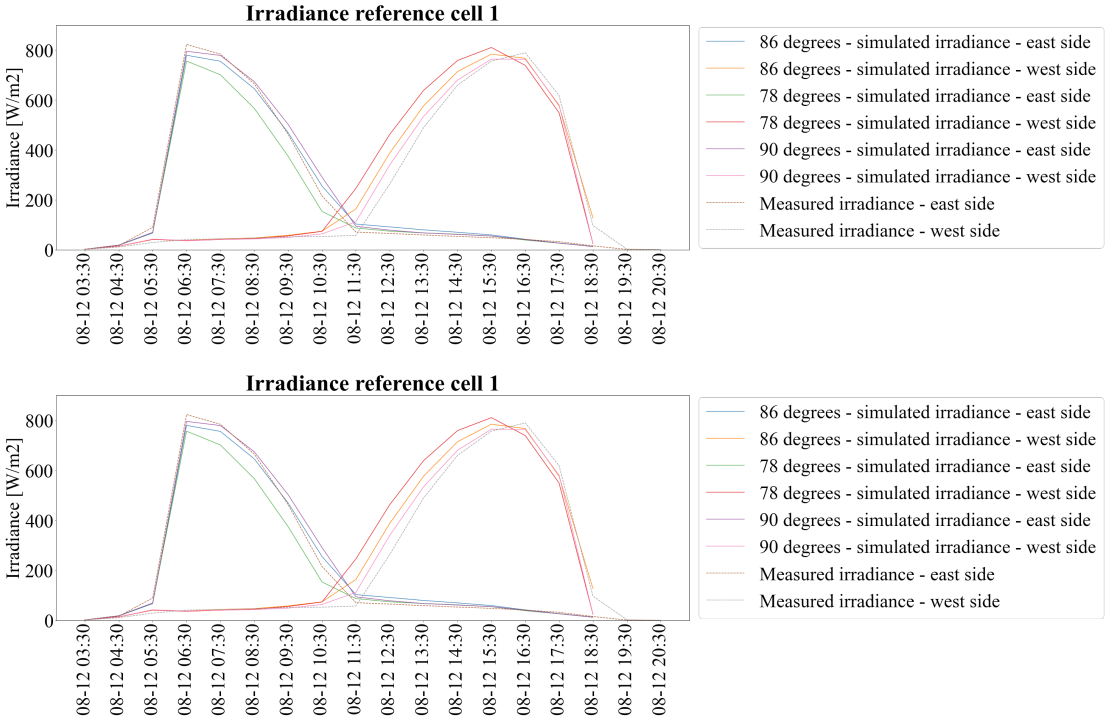

Figure 34: *Simulated irradiance for reference cell 1 the* 12^{th} *of August 2022 and the* 26^{th} *of January 2023 for the three orientations 78°, 86°, and 90° compared to measured irradiance.*

As the figure shows, for both the 12^{th} of August and the 26^{th} of January, there is some deviation between the simulated irradiance for the orientations 90°, 86° and 78°. Compared to measured irradiance, the deviation increase when the orientation according to north decreases as the deviation between simulated irradiance for 78° and measured irradiance is larger than for the orientations 90° and 86°.

For both days on the east side, the simulated irradiance for an orientation of 86° gives the best results compared to measured irradiance, while an orientation of 90° gives the best results for the west side. Thus, the 4° difference in orientation is significant, and using the exact orientation of the test site when creating the 3D model is important for accurately simulated irradiance. Retrieving an exact orientation using Google Earth Pro is difficult as the resolution of the map gets grainy when zoomed in. Hence, there is some uncertainty in the orientation of 86°.

The measured orientation of 86° is for the solar panels on the test site, and it was assumed that the reference cells had the same orientation as the solar panels. This is not necessarily true and can be a source of error resulting in a deviation between simulated and measured irradiance. Also, placing the sensors for simulating the irradiance in the 3D model with the exact orientations and position at the test site is difficult as the sensors are positioned outside the reference cells as described in Section 4.1.4. This may have caused some deviations in the simulated irradiance as well.

As the altitude of the Sun and the day length varies through the year, using the correct orientation of the PV system and the objects in the 3D model is important to achieve accurate shading and irradiance results for the specific location. An orientation of 86° was chosen when simulating the irradiance due to the results

in Google Earth Pro, but there is an uncertainty in this value. A few degrees can have a significant impact on the simulated irradiance as shown in Figure 34. Thus, the orientation of the solar panels and the reference cells is a parameter one should validate further, for example by using measurements from the test site and trigonometry.

4.2.2 Angle of incidence

bifacial_radiance does not take losses due to AOI into account when simulating the irradiance and therefore, the results shown in Section 4.1.1 – 4.1.6 are without these losses. On the other hand, as the reference cells are built like solar cells, losses due to AOI are taken into account when the irradiance reaches the reference cells. Therefore, the simulated irradiance is expected to be a bit higher than the measured irradiance, and losses due to AOI may be a factor that can explain some of the deviations between simulated and measured irradiance for the simulated days and months in Section 4.1.1 – 4.1.6.

The impact taking the losses due to AOI into account has on the simulated irradiance was tested with the method described in Section 3.5.2. The results were then compared to the measured irradiance and the simulated irradiance without the losses taken into account. For reference cell 1, the results for the 12^{th} of August 2022 and the 26^{th} of February 2023 are shown in Figure 35.

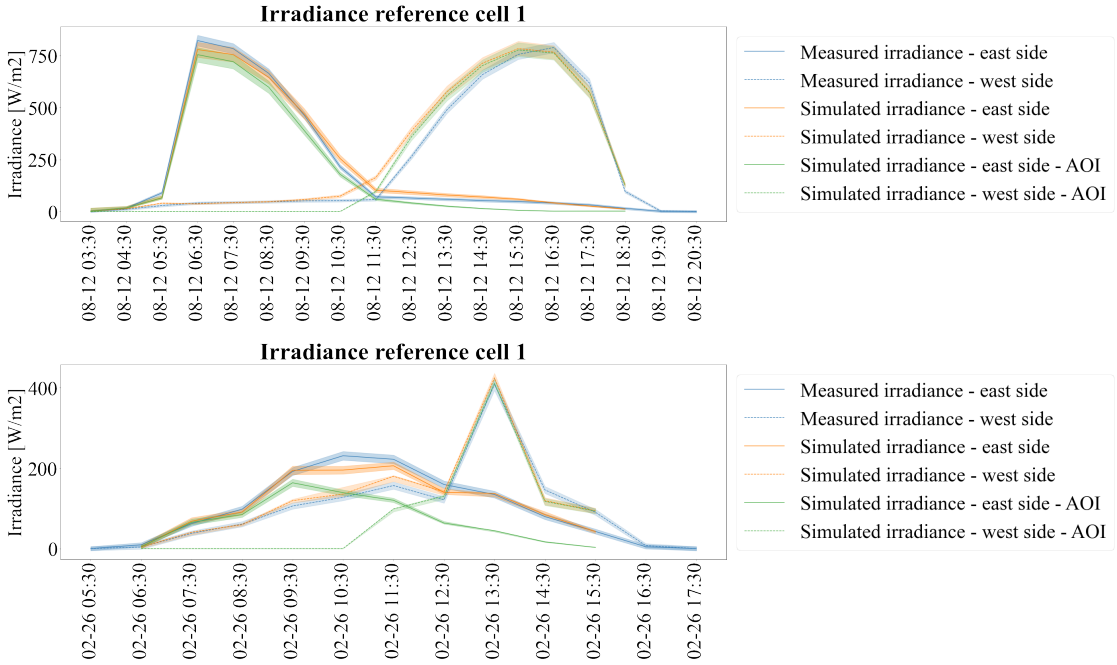

Figure 35: *Measured irradiance compared to the simulated irradiance with and without the losses due to angle of incidence (AOI) taken into account for reference cell 1. The case where the losses due to AOI have been taken into account are labeled "Simulated irradiance - east/west side - AOI". The days shown are the* 12^{th} *of August 2022 and the* 26^{th} *of February 2023 with measurement uncertainty.*

For the 12^{th} of August, the simulated irradiance when taking losses due to AOI into account is lower than the simulated irradiance without the losses taken into account. The exception is before 6:30 AM on the east side and after 3:30 PM on the west side the 12^{th} of August where the losses seem to have a negligible effect

on the irradiance. As is the case for 26^{th} of February where the losses seem to have a negligible effect on the irradiance before 8:30 AM and after 12:30 PM on the east and west sides, respectively. Hence, the losses due to AOI seem to increase as the AOI increases towards 90°, which is the case from the morning to the Sun passes south for the east side of the solar panels. For the west side, on the other hand, the losses due to AOI seem to decrease as the Sun passes south towards the evening as the AOI decreases.

Before the Sun passes south, the west side of the solar panels only receives diffuse irradiance, while the east side of the panels receives both direct and diffuse irradiance due to the vertical mounting. The opposite is the case when the Sun has passed south. The Sun passes south at approximately 11:30 AM for the 12^{th} of August. When the solar panels only receive diffuse irradiance, towards the evening for the east side and in the morning for the west side, the deviation between measured irradiance and simulated irradiance with losses due to AOI was taken into account is larger, probably because the estimated AOI from the pvlib model irradiance.aoi exceeds 90°. How losses in irradiance due to the angle between the irradiance and the surface of the solar panels when the east and the west side only receive diffuse irradiance were not studied further. Regardless, as Figure 35 shows, AOI has an impact on the irradiance, but how the losses impact the irradiance when only diffuse light reaches the solar panels needs to be validated further.

Still, for some timestamps the irradiance when taking AOI into account is lower than the measured irradiance such as the 26^{th} of February at 10.30 PM, while it for other timestamps is higher such as the 12^{th} of August at 1:30 PM. Therefore taking the losses due to AOI into account will not explain all the deviation between measured and simulated irradiance shown in Section 4.1.1 – 4.1.6. For simplicity, the results for simulated irradiance without the losses due to AOI were used to simulate the power output.

4.2.3 Albedo

Since the albedo is a parameter dependent on several parameters as mentioned in Section 2.1.4, it is not optimal to use a constant value throughout a day or for a longer period of time. Hence, the daily albedo with measurement uncertainty for different seasons at the test site is shown in Figure 36.

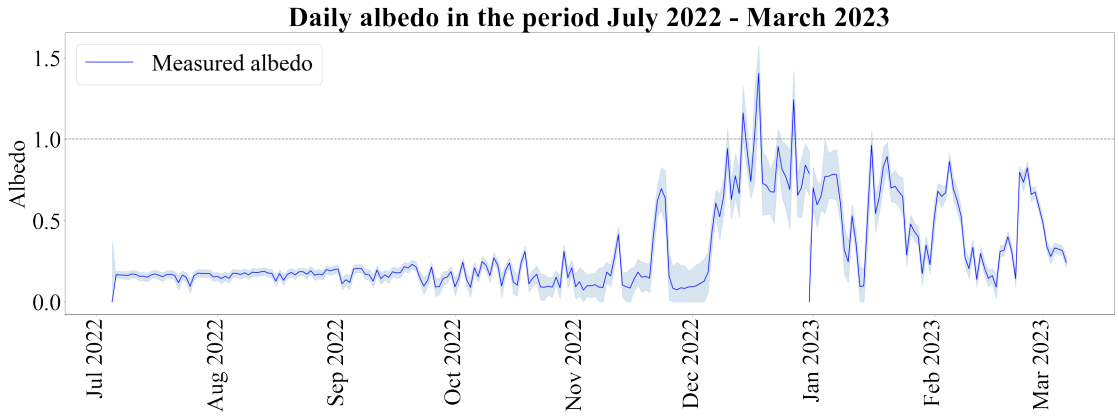

Figure 36: *Daily measured albedo values for the period July 2022 to the beginning of March 2023 with measurement uncertainty.*

The measured upwards and downward irradiance used to calculate the albedo from the test site are on a 5-minute interval. Therefore, the daily albedo shown in Figure 36 was estimated by summarizing the upwards and downward irradiance before using equation 4. The corresponding measurement uncertainty was estimated using equation 18 – 24 from the method described in Section 3.4.1, on the upwards and downwards irradiance with a 5-minute interval. Thereafter, the results were summarized before and the uncertainty in albedo was calculated with equation 25.

As Figure 36 shows, there are some days in December when the measured albedo is above 1, which is not physically possible. Figure 37 shows the albedo on a 5-minute interval for the 17^{th} of December and the 18^{th} of December 2022, an overcast day and a day with Sun and some variations in the weather, respectively. Also, the incoming and reflected irradiance used to calculate the albedo is shown, together with the measurement uncertainty.

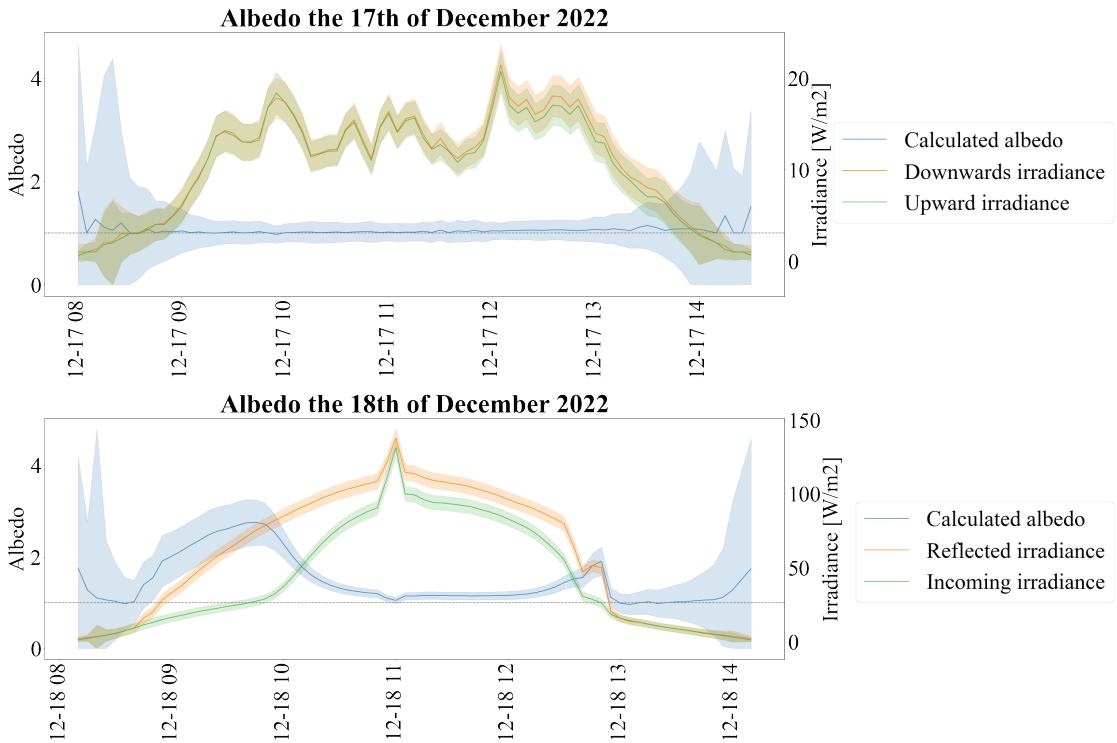

Figure 37: *Daily variations in the albedo, upward irradiance, and downward irradiance for the* 17^{th} *and the* 18^{th} *of December 2022 with measurement uncertainty.*

For the 17^{th} of December in Figure 37, the albedo is around 1 as the irradiance measured by the upwards and downwards pyranometer is approximately the same the whole day. For the 18^{th} of December on the other hand in Figure 37, the albedo is constantly above 1 because the reflected irradiance is greater than the incoming irradiance. At 11:00 AM this day, there is a spike in incoming and reflected irradiance. Establishing the cause of this spike has not been done, but variations in GHI, DHI, and DNI due to the weather and clouds are likely the cause. On both days the measurement uncertainty in albedo varies throughout the day. Still, a high albedo is expected for both the 17^{th} and the 18^{th} of December due to the amount of snow these days as shown in Figure 38. Snow has a high albedo, as shown in Table 1, and results in more reflected irradiance from the ground.

Figure 38: *A picture of the test site taken by a webcam from the north the* 17^{th} *of December 2022 at 2:00 PM.*

Even though the albedo is high the 17^{th} and the 18^{th} of December, the albedo can never exceed 1. Hence, the pyranometer measuring the reflected irradiance may detect irradiance reflected from other objects and surfaces nearby the pyranometer. Due to the amount of snow, this is less likely as most of the objects on the roof are covered in snow. Therefore, a more likely explanation is that the downward pyranometer, in addition to reflected irradiance, detects direct irradiance due to the low altitude of the Sun in Norway during the winter. Also, the pyranometer measuring incoming irradiance, in Figure 39 may be covered in a thin layer of snow as it faces upwards. Consequently, the measured incoming irradiance may be underestimated, resulting in a smaller difference between the upwards and downwards irradiance or that the downward pyranometer detects more irradiance than the upward pyranometer as shown in Figure 37.

Figure 39: *The pyranometer (1), pyrheliometer (2), and albedometer (3) relative to the test site.*

From Figure 36, the daily albedo is relatively constant for the period July – September, before the variations increase towards the winter. The variations in albedo may increase due to more variations in the weather such as rain, frost, and snow. Hence, using a constant value for the albedo for a longer period of time will probably have an impact on the simulated irradiance, especially in the winter. Using a constant albedo for all seasons will not be representative, not even for a day. As Figure 40 shows, the albedo for the 12^{th} of August 2022 and the 26^{th} of February 2023 on a 5-minute interval varies throughout the day. Also, the mea-

surement uncertainty in albedo varies with approximately ±0.25 and ±0.5 from the measured values for August and February, respectively.

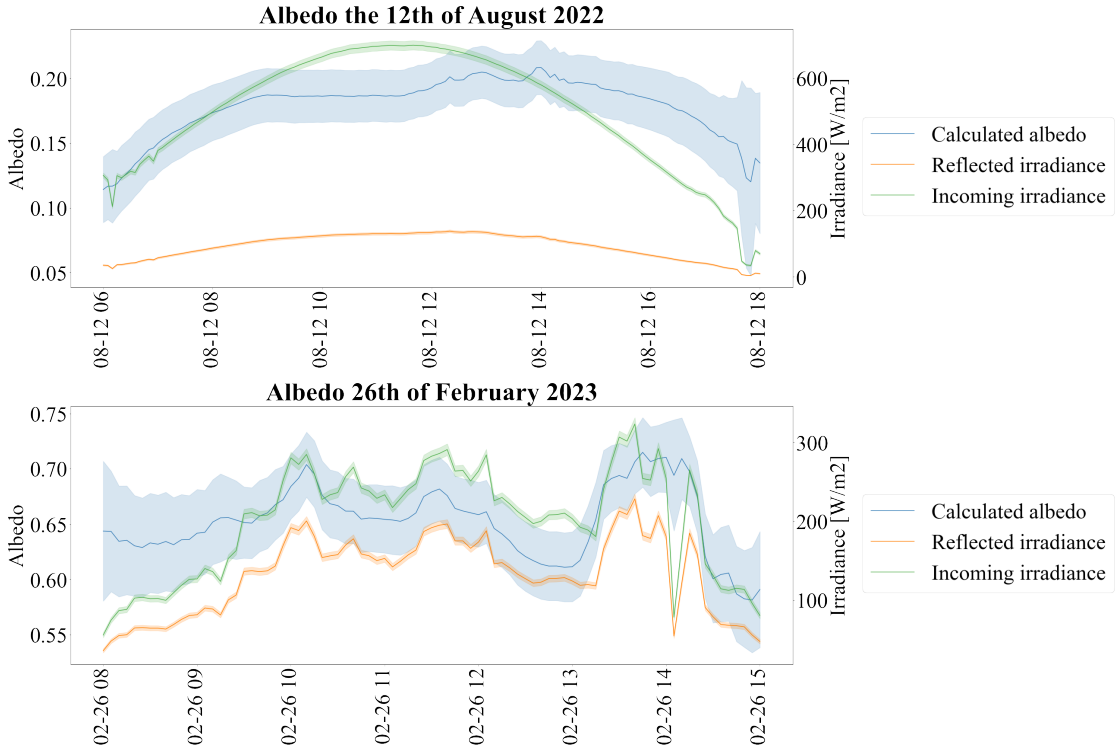

Figure 40: *Daily variations in the albedo, upward irradiance, and downward irradiance for the* 12^{th} *of August 2022 and the* 26^{th} *of February 2023 with measurement uncertainty.*

For both the 12^{th} of August and the 26^{th} of February, the measurement uncertainty in albedo is significant and will probably have an impact when simulating the irradiance using the 3D model. The reflected irradiance from the ground is dependent on the amount of diffuse irradiance, weather, and the AOI. As mentioned in Section 2.1.4, rain can decrease the albedo of a material due to lower reflection of the irradiance. The roughness of the material also lowers the albedo as the irradiance reaching rough surfaces gets more scattered when reflected, while the albedo increases with smooth and glossy surfaces. These factors can explain the variation in albedo for the 12^{th} of August. For the 26^{th} of February on the other hand, there was a layer of snow on approximatly 11 cm [52] on the roof affecting the albedo as it does for the 17^{th} and 18^{th} of December in Figure 37. Thus, using a constant albedo may cause more uncertainty when simulating the irradiance for one day, and it was concluded to use the albedo for each timestamp when simulating the irradiance for all the days in Section 4.1.1 – 4.1.4 and Appendix E.

It is complicated to keep track of the factors that may affect the albedo and eliminate them to retrieve accurate albedo for the test site. The mounting of the albedometer may also affect the measured irradiance upwards and downwards. The closer to the ground the albedometer is installed, the more shadow may be detected by the downward pyranometer. These results may cause an underestimation of the measured irradiance because of an increased view angle between the pyranometer and the shaded area. Installing the albedometer too high makes it prone to detect reflected irradiance from the environment and other materials than the surface underneath, as well as direct irradiance. [54] If the albedometer at the test site was mounted correctly, too high or too low has not been studied.

4.2.4 How albedo affects the measurement uncertainty

As mentioned, the measurement uncertainty in measured GHI, DHI, DNI, and albedo has been estimated with the method in Section 3.4.1, while the measurement uncertainty of the reference cells is defined to be ±2.5 % ±5 W/m^2. This measurement uncertainty is displayed as a shaded area around the simulated irradiance and measured irradiance in Figure 26, 27, and 30.

As Section 4.2.3 describes, the albedo is dependent on several factors such as weather, snow, and amount of diffuse and direct irradiance. Therefore, only taking the measurement uncertainty due to the albedo into account when simulating the irradiance was investigated to see the impact albedo alone had on the measurement uncertainty. The results for reference cell 2 the 12th of August 2022, and the 22nd of February 2023 are shown in Figure 41. The results for all the reference cells are shown in Appendix G.

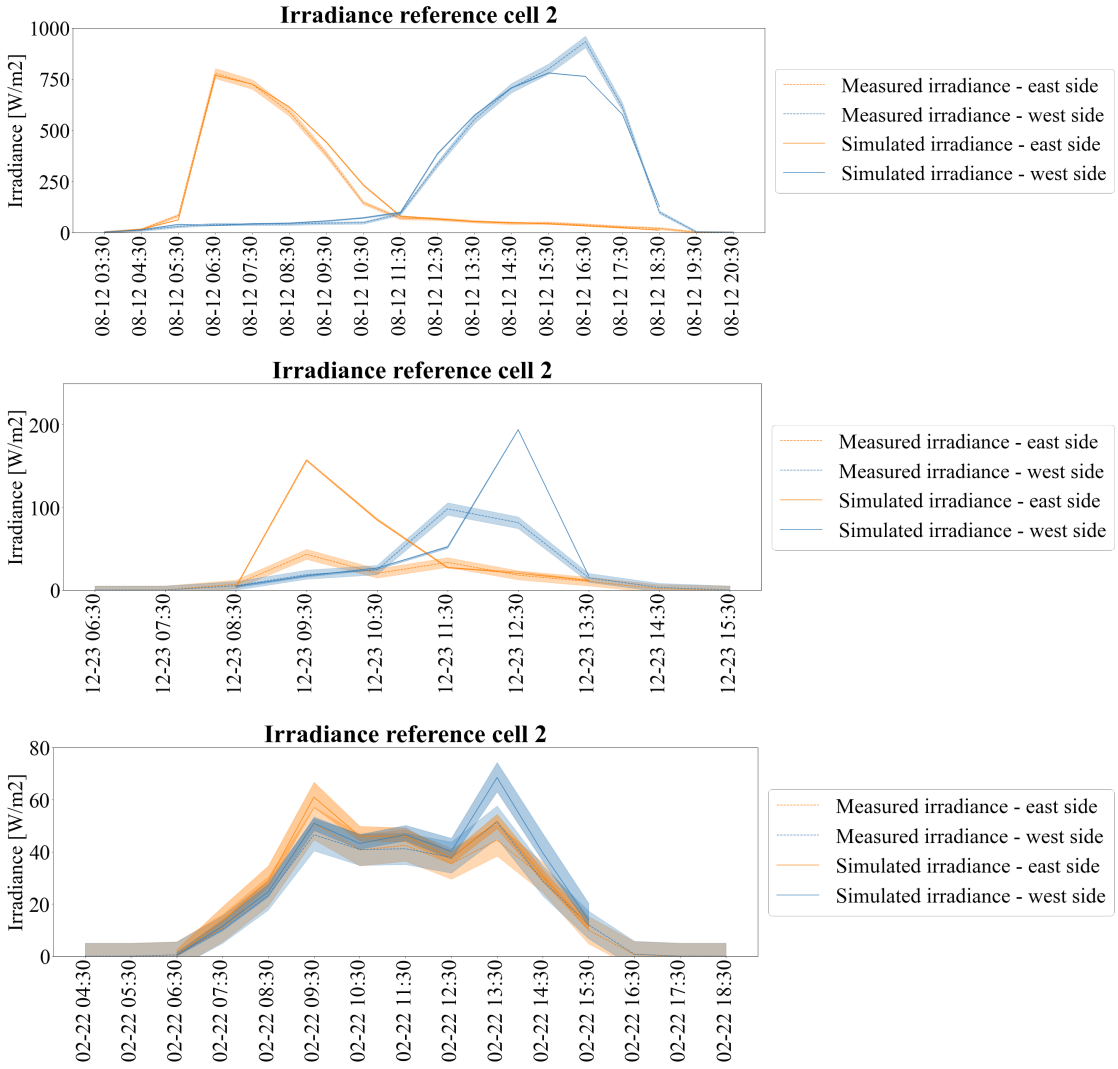

Figure 41: *Simulated and measured irradiance for reference cell 2 the 12th of August 2022, the 23rd of December 2022 and the 22nd of February 2023. The measurement uncertainty in simulated and measured irradiance is displayed as a shaded area, but the measurement uncertainty for simulated irradiance is only due to albedo.*

As Figure 41 shows, the measurement uncertainty due to albedo for the simulated irradiance is different compared to the measurement uncertainty in Figure 26, 27, and 30. For the 12^{th} of August and the 23^{rd} of December the measurement uncertainty in simulated irradiance from Figure 41 seems almost negligible compared to Figure 26 and 30. The measurement uncertainty for the 22^{nd} of February on the other hand seems to be almost the same compared to the measurement uncertainty shown in Figure 30.

As Figure 40 shows, the albedo for the 12^{th} of August is low and varies between 0.1 and 0.2 as the bitumen on the roof has some texture and a low albedo. For the 26^{th} of February on the other hand, the albedo varies between 0.6 and 0.7 due to a layer of snow on the roof at approximately 11 cm [52]. Due to the low albedo for the 12^{th} of August, the ground reflection is low and the irradiance contribution from the ground is low. During the summer, the irradiance is high and therefore, the measurement uncertainty increases significantly when GHI, DHI, and DNI are taken into account as well.

For the 22^{nd} of February, with higher ground albedo such as the 26^{th} of February due to snow and lower irradiance, the irradiance contribution from the ground may be higher due to more reflection. Consequently, albedo contributes more to the measurement uncertainty than GHI, DHI, and DNI, and hence, the deviation in the measurement uncertainty for simulated irradiance in Figure 41 and 30 seem approximately the same for the 22^{nd} of February. On the other hand, for the 23^{rd} of December, the irradiance is low and there is snow covering the test site resulting in a high albedo. As this day is a clear-sky day, the irradiance may be higher than for the 22^{nd} of February. This may be an explanation too why albedo seems to contribute to lower measurement uncertainty for the 23^{rd} of December than for the 22^{nd} of February. Hence, how much albedo alone contributes to the measurement uncertainty varies with the day, irradiance condition, and season. Resultingly, it is important to consider GHI, DHI, DNI, and albedo when estimating the measurement uncertainty as these variables have been used as input into bifacial_radiance.

4.3 Power output from the test site

Simulating the generated DC and AC power was carried out for the days where the irradiance was simulated on an hourly interval. All the results are shown in Appendix H, while some selected days and months are shown in the following section. For all results shown, the power has been estimated using both simulated irradiance from bifacial_radiance and measured irradiance from the reference cells at the test site. The measurement uncertainty shown in the results is due to GHI, DHI, DNI, and albedo such as in Section 4.1.1 - 4.1.6.

4.3.1 Models to simulate the DC power

As mentioned in Section 3.6, the pvlib models pvwatts and singlediode were tested when simulating the DC power. The singlediode model requires input about the solar panels on the test site as shown in equation 6. The pvwatts model on the other hand requires less input as shown in equation 5. Therefore, the singlediode model may be more accurate as the input parameters in equation 6 are updated

for all timestamps in the period where the DC power is simulated. Consequently, variations in PV efficiency can be caught when there are changes in the irradiance. This may not be the case for pvwatts, as no information about the solar panels is implemented in the model. The only parameters in pvwatts updated for each timestamp are irradiance and temperature.

The generated DC power from the PV system, when using the simulated irradiance from bifacial_radiance, was simulated with both pvwatts and singlediode. The results from these models are shown for the 12^{th} of August 2022 in Figure 42.

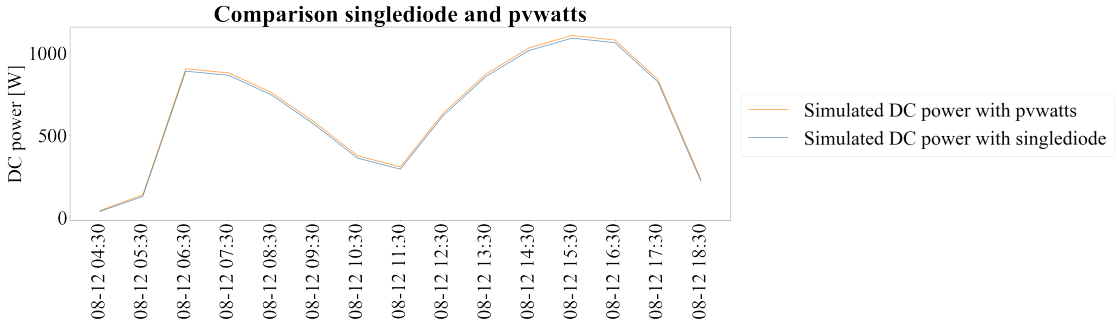

Figure 42: *Simulated DC power with the use of pvwatts and singlediode from the simulated irradiance from bifacial_radiance for the* 12^{th} *of August 2022.*

As the figure shows, there is a small difference between the two models, but compared to singlediode, pvwatts is overestimating a little. Even though the deviation between these two is small, a deviation of a few percent may be significant for the results, especially for low irradiance. The DC power has been simulated using instantaneous irradiance values on an hourly interval. Thus it may be difficult to evaluate the actual accuracy of the two models as the variation in irradiance in the morning and the afternoon for the 12^{th} of August is not caught using hourly intervals as shown in Figure 26 and 27. Hence, using irradiance on 5-minute intervals could have shown more variations between the two models, but this was not tested. For the results shown in Section 4.3.2 and 4.3.3 and in Appendix H, the model singlediode was used to simulate the DC power.

4.3.2 The time interval in data used to simulate power

For the selected days shown in this Section 4.3.3, the simulated DC and AC power for the test site with measurement uncertainty is shown together with the inverter efficiency as a function of DC power. Note that the simulated and measured irradiance for all three reference cells, on both the east and the west side have been combined to estimate the total average irradiance on the solar panels. Therefore, underestimation and overestimation of simulated irradiance compared to measured irradiance balance each other out and may make the overall deviation between simulated and measured irradiance smaller.

The measured DC and AC power have been retrieved from the monitoring system belonging to the SolarEdge inverter on the test site. These data have been aggregated by the Solaredge monitoring system at 15-minute intervals. As the 15-minute interval is the lowest interval in the DC power for the PV system from SolarEdge, this is the interval used for the measured DC and AC power. Hence, the instantaneous values for DC and AC power at the timestamps 10:30 AM, 11:30 AM, etc., are based on data with a 15-minute interval. On the other hand, the

measured irradiance from the reference cells and the radiometers measuring GHI, DHI, DNI, and albedo used to simulate the irradiance was retrieved from meteocontrol Virtual Control Room (VCOM), a monitoring system for PV systems. The data have been aggregated by VCOM to a 5-minute interval which has been used in this thesis to select the instantaneous values for the timestamps 10:30 AM, 11:30 AM, etc. These data have been used to simulate irradiance and consequently the DC and AC power. Hence, there is an unfortunate difference in the data used for measured and simulated DC and AC power when comparing them. Not only due to data based on different time intervals, but also because the aggregation of data in SolarEdge and VCOM may be different when it comes to for example binning of data.

Simulated DC and AC power for the 22^{nd} of July 2022 with measurement uncertainty compared to measured DC and AC power plotted hourly is shown in Figure 43. The measurement uncertainty in measured DC and AC power has been disregarded.

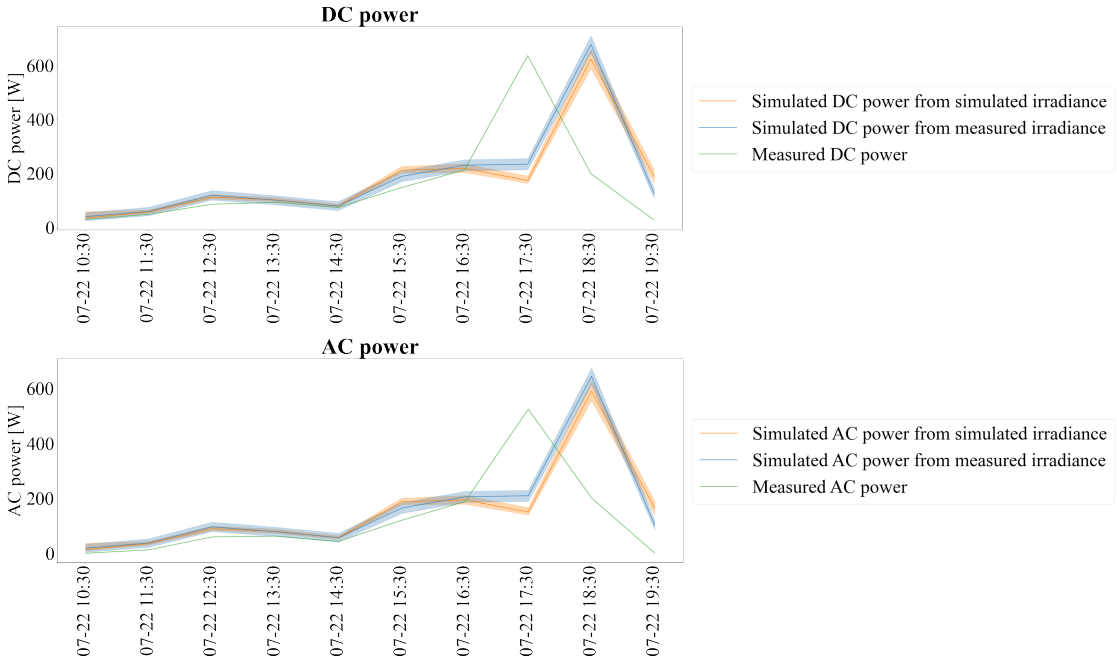

Figure 43: *The simulated DC and AC power from simulated and measured irradiance compared to measured DC and AC power for the* 22^{nd} *of July 2022. The measurement uncertainty in simulated power is displayed as a shaded area.*

The simulated irradiance compared to the measured irradiance for the 22^{nd} of July 2022 is shown in Appendix E. As Figure 43 shows, there is good compliance in the results as there is a low deviation between the simulated DC and AC power using simulated and measured irradiance. On the other hand, the spike in measured DC and AC power occurs at 5:30 PM, an hour before the spike in simulated DC and AC power. This can possibly be explained by the interval difference in measured and simulated DC and AC power, and how SolarEdge and VCOM aggregate the data. Still, except for this spike, there is good compliance between simulated and measured DC and AC power, and if the spike had been on the same timestamp, there would have been a low deviation between the results. The differences in using data on a 5-minute, 15-minute, and hourly interval are shown in Figure 44 for measured AC power and GHI the 22^{nd} of July.

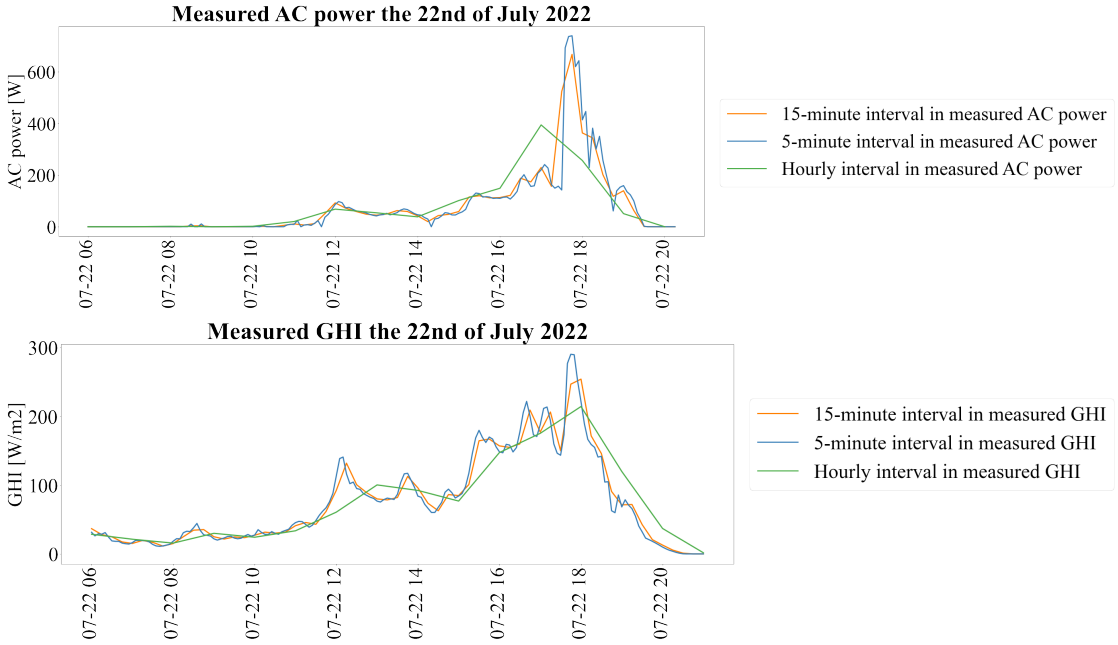

Figure 44: *Measured AC power and GHI using a 5-minute, 15-minute and hourly interval for the* 22^{nd} *of July 2022.*

As Figure 44 shows, there is a deviation in AC power and GHI based on the interval in data, and there is a small displacement between data with 5-minute and 15-minute intervals. Regardless, they follow the same trends and catch the same variations. When using hourly intervals in data, on the other hand, a lot of variation is lost. As Figure 44 shows, for AC power, the spike when using an hourly interval is moved to the left of the spike when using a 5-minute interval, and the spike is lower. For GHI, the spike using hourly intervals is right after the spike when using a 5-minute interval, and the measured irradiance is lower.

Due to the displacement between data on the 5-minute and 15-minute interval as shown for AC power in Figure 44, there is possible to lose information when plotting the timestamps 10:30 AM, 11:30 AM, etc. as shown in Figure 45. Even though there most of the time is a similar trend in data for a 5-minute and a 15-minute interval, plotting the hourly values for the timestamps 10:30 AM, 11:30 AM, etc. based on data with 5-minute intervals misses the spike right before 6:00 PM, but the spike is caught when selecting the timestamps from the data on a 15-minute interval. Hence, if the data compared are based on different time intervals, this can cause deviation in the results.

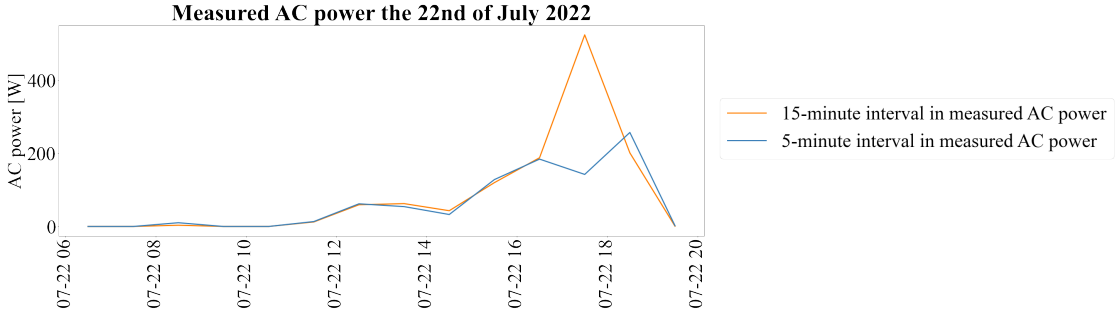

Figure 45: *Measured AC power on a 5-minute and 15-minute interval the* 22^{nd} *of July 2022 plotted for hourly for the timestamps 10:30 AM, 11:30 AM, etc.*

Therefore, to eliminate this source of error, it is important to compare data aggregated in the same way and based on the same interval. Unfortunately, this was discovered late, and not possible to include in this thesis as simulating the irradiance for all the days again would have taken too much time. Therefore for the timestamps 10:30 AM, 11:30 AM, etc., in this thesis, measured DC and AC power are based on a 15-minute interval while the simulated and measured irradiance, and hence, simulated DC and AC power, are based on a 5-minute interval.

4.3.3 Simulated power and inverter efficiency for selected days

A day where the power was simulated is the 12^{th} of August 2022. For this day comparing simulated and measured DC and AC power based on 5-minute and 15-minute intervals, respectively, seem to work. The trends in the results shown in Figure 46 mostly seem to have good compliance.

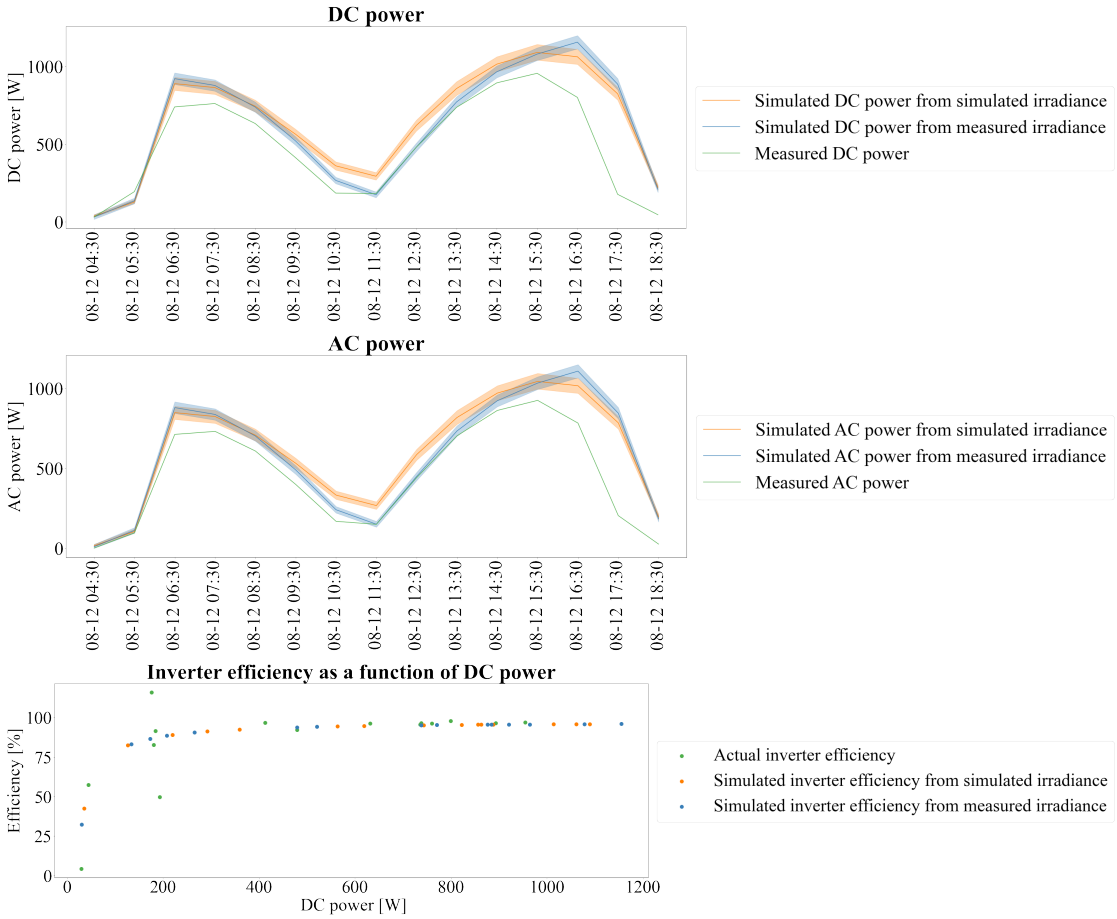

Figure 46: *Simulated DC and AC power from simulated and measured irradiance compared to measured DC and AC power for the* 12^{th} *of August 2022 with the inverter efficiency as a function of DC power. The measurement uncertainty simulated power is displayed as a shaded area.*

From Figure 46, there is a good compliance between simulated DC power when using simulated and measured irradiance. This is expected as there is good compliance between simulated and measured irradiance in Figure 26 most of the day, but there is some deviation between the timestamps 9:30 AM and 1:30 PM. Between these timestamps, there are deviations between the simulated power from simulated irradiance and measured power as well. As the simulated irradiance is

not identical to the measured irradiance, as shown in Figure 26, it is expected to be a deviation between simulated DC and AC power from simulated and measured irradiance due to the following error. The simulated power from using the simulated and measured irradiance is overestimated compared to measured DC and AC power. This may be expected because system losses such as shading, cable losses, degradation and quality of the solar panels, and inverter losses among other factors are not considered when simulating the power. These factors are taken into account in the measured DC and AC power as they affect the measured power registered by the monitoring system.

In the afternoon, the measured DC power starts to decrease an hour before the simulated DC power at 3:30 PM. As the simulated power from measured irradiance does not start to decrease at the same time as the measured power, the test site and the solar panels may suffer from shading, while the reference cells do not. In other words, the system losses, including shading are important factors to consider for more precise simulations. The same deviation between simulated and measured power is shown for the AC power simulated with the model inverter.pvwatts as a following error from the DC power.

For simplicity, it was assumed that all the solar panels on the test site received the same irradiance and the same temperature. When the solar panels from Over Easy Solar AS were tested in the lab at IFE, the bifaciality factor varied in the range of 75.6 % – 80.6 %, but the average of 78.6 % was used in the power simulations. Consequently, using the average value for bifaciality factor when estimating the total average irradiance, and assuming equal irradiance and temperature on all solar cells on the test site are possible explanations for some of the deviations between measured and simulated power.

On the other hand, the simulated inverter efficiency as a function of DC power corresponds well with actual inverter efficiency as shown in Figure 46. When the power is approximately 200 W, the actual inverter efficiency stands out as there is one point with an inverter efficiency above 100 % and one at approximately 50 %. These outliers from the efficiency curve are most likely measurement error as it only happens when the power is 200 W. Good compliance between simulated and actual inverter efficiency indicates that the pvwatts inverter model, based on equation 11 delivers accurate results, even though the default values for η_{nom} and η_{ref} were used and that the losses specific to the test site were not implemented. The default values for η_{nom} and η_{ref} may be different from the actual values for the inverter on the test site. Still, this does not seem to affect the results unless the difference between η_{nom} and η_{ref} from equation 11 is larger than in the default values. Thus, using the default values is a source of error.

The average value for the actual inverter efficiency is 84.40 %, while the average value for simulated inverter efficiency from simulated and measured irradiance is 90.06 % and 88.91 %, respectively. That the simulated inverter efficiency is higher is expected as the DC and AC power is higher than the measured power and due to the system losses not being taken into account. Still, the efficiency is lower than the expected inverter efficiency which typically is in the range 95 % – 98 %, depending on the inverter used [35]. The inverter efficiency shown in Figure 46 passes 75 % at approximately 200 W and increases with the generated power and irradiance. For low DC power, the efficiency is low.

From Table 3 the maximum DC power input to the inverter is 3400 W, but the rated DC power on the test site is 1440 W. For the efficiency of the inverter to be high, the DC power of the test site should be approximately the same as the rated inverter capacity of 3400 W. Hence, the inverter on the test site is suitable for a PV system more than doubled the test site studied here. In other words, the inverter is not optimal and it is underdimentioned. The result is a lower efficiency, where the maximum generated AC power is not achieved. The 23^{th} of December 2022 shown in Figure 47 is an example of one day where the generated DC power is low, and hence the efficiency is low. The measured DC power this day never reaches more than approximately 60 W – 70 W, resulting in a maximum inverter efficiency in the range of 50 % – 60 %.

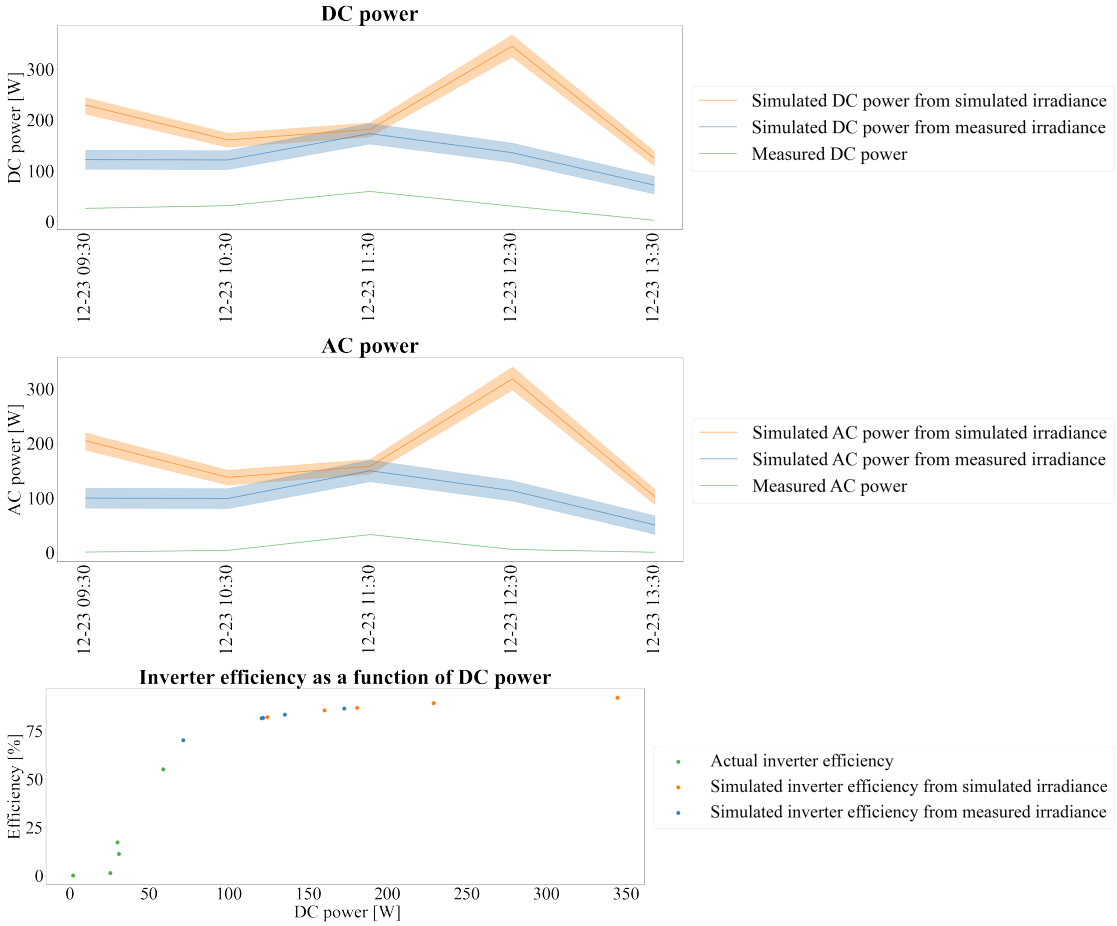

Figure 47: *Simulated DC and AC power from simulated and measured irradiance compared to measured DC and AC power for the 23^{rd} of December 2022 and the inverter efficiency as a function of DC power. The measurement uncertainty simulated power is displayed as a shaded area.*

As Figure 47 shows, the generated power is low with an average actual inverter efficiency of 16.95 %. The simulated efficiency from simulated and measured irradiance on the other hand is 87.28 % and 80.68 %, respectively. Hence, there is a large deviation between the results and between simulated and measured DC and AC power. A deviation between simulated DC and AC power from simulated and measured irradiance is expected as there is a difference in measured and simulated irradiance from Figure 26, due to snow covering the test site as shown in Figure 29. As the snow covers the solar panels, most likely a low amount of irradiance reaches the solar panels this day, and hence, the measured DC and AC power is low. Thus,

it is clear that weather conditions on the test site and accurate irradiance when simulating power, are important to achieve accurate DC and AC power estimates.

Overall, simulating the power using the singlediode and the inverter.pvwatts models give a rough estimate of the expected power output from a PV system and the inverter efficiency. Still, shading on the solar panels and snow covering the solar panels will cause uncertainty in the simulated power. Hence, system losses, accurate weather conditions, and accurate irradiance are important to take into account for better estimations and more accurate results.

4.4 Energy simulation using a cumulative sky

As for a daily basis, there may be a difference in how the data compared have been aggregated. The irradiance used as input in bifacial_radiance is on the hourly interval based on data with a 5-minute interval, which is then aggregated to create the cumulative sky. The measured energy from SolarEdge on the other hand has been retrieved on a daily basis and summarized to retrieve the energy for the wanted time period. How bifacial_radiance and SolarEdge aggregate the data and how that possibly affect the results have not been investigated in this thesis.

From simulating the power for specific days on an hourly interval in Section 4.3.3, the irradiance from cumulative sky results in one value for the whole period simulated. As the singlediode model used in Section 4.3.3 needs variation in the irradiance to estimate the power, this model cannot be used to simulate the DC energy. Consequently, the pvwatts model from pvlib was used to simulate the DC power for the irradiance retrieved with a cumulative sky as this model can be used to calculate the DC energy for one timestamp only. The simulated DC energy from simulated and measured irradiance compared to measured DC energy for the same time period are shown in Figure 48 with the measurement uncertainty for the simulated DC power displayed as error bars.

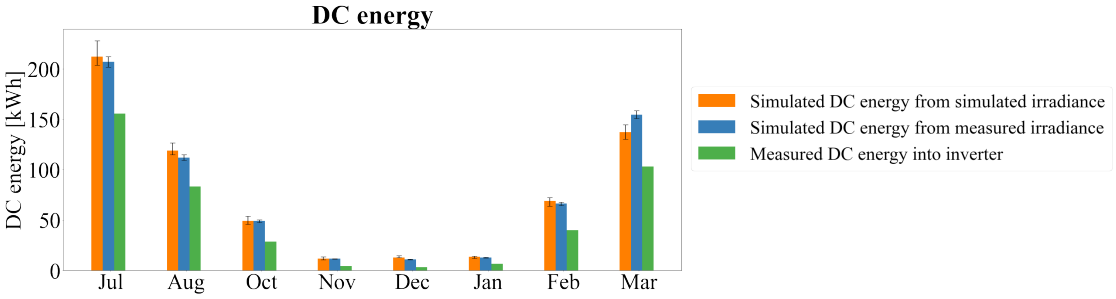

Figure 48: *The simulated DC energy from simulated and measured irradiance using a cumulative sky with the measurement uncertainty shown as error bars compared to measured DC energy.*

As Figure 48 shows, the simulated DC energy from both simulated and measured irradiance overestimates for all the months shown, but the deviation between the results varies. The percentage difference between simulated DC energy from simulated and measured irradiance, between simulated DC energy from simulated irradiance and measured DC energy, and between simulated DC energy from measured irradiance and measured DC energy is shown in Table 6.

Table 6: *The percentage difference between simulated DC energy from simulated and measured irradiance (SMI), between simulated DC energy from simulated irradiance and measured DC energy (SIM) and between simulated DC energy from measured irradiance and measured DC energy (MIM) when using a cumulative sky.*

	Jul	**Aug**	**Oct**	**Nov**	**Dec**	**Jan**	**Feb**	**Mar**
Difference SMI	2.37 %	5.97%	0.01 %	2.18 %	15.66 %	6.46 %	3.95 %	11.78 %
Difference SIM	30.62 %	35.31 %	52.61 %	89.82 %	119.58 %	68.50 %	53.23 %	28.42 %
Difference MIM	28.29 %	29.50 %	52.62 %	88.07 %	109.03 %	62.73 %	49.54 %	39.86 %

As Table 6 shows, the percentage difference between the results shown in Figure 48 varies. The deviation between the simulated DC energy from simulated and measured irradiance is overall low as a following error due to the deviation in simulated and measured irradiance from Table 5. For October the percentage difference between simulated irradiance from measured and simulated irradiance is 0.01 %, hence, the pvwatts model hits perfectly when simulating the DC energy for this case, but the percentage difference is higher for all other months with the maximum being 15.66 % in December.

Comparing the simulated and the measured DC energy on the other hand displays a larger deviation overall, with the percentage difference exceeding 100 % in December. As an example, the simulated DC energy from simulated irradiance results in a DC energy more than doubled the measured DC energy as the difference between the two is 119.58 %. A larger deviation between simulated and measured DC energy during the winter is expected as snow may cover the test site resulting in non or low irradiance on the solar panels and hence low measured power. The deviations may also be the result of shading which can affect the test site, but not the reference cells and the radiometers. Hence, the large percentage difference substantiates that system losses such as shading and losses due to snow, as well as accurate irradiance simulations, are important to consider to retrieve accurate estimations of the expected energy output.

The deviation between simulated DC energy in Figure 48 and measured DC energy can also be due to the use of the pvlib model pvwatts. If this was a cause for the deviation or not was investigated, but as there is one irradiance value for the entire period simulated, deviations in the irradiance throughout the months were neglected. Hence, there is a possibility that simulating the DC power daily for a month using singlediode as in Section 4.3.3, and then comparing it to measured DC energy would have resulted in more accurate results as variation in PV efficiency would have been included. On the other hand, this is time-consuming to perform. Thusly, how to estimate the power output with irradiance from bifacial_radiance needs to be studied further and system losses need to be considered to retrieve results with lower percentage difference.

The AC energy and the inverter efficiency have not been simulated because the inverter model used in Section 4.3.3 expects variations in the DC energy. The variation in DC energy is not present when using irradiance from a cumulative sky.

5 Conclusion

In this thesis, a test site at the Institute for Energy Technology (IFE) consisting of vertically mounted solar panels from Over Easy Solar AS has been studied. The goal was to evaluate the software bifacial_radiance, RADIANCE, and pvlib for simulating irradiance and power output using a 3D model. Factors that may be present while simulating the irradiance and affect the results, such as the orientation of the PV system, albedo, angle of incidence (AOI), and site-specific parameters like shading and snow are addressed as well. Measured GHI, DHI, DNI, and albedo retrieved from the test site were implemented to simulate the irradiance [W/m^2] and power output [W], making it possible to compare the results with measured data. A measurement uncertainty analysis was performed on the data from the test site, but losses due to soiling and snow were neglected.

The 3D model created in bifacial_radiance was developed from the cell level, resulting in a detailed model of the PV system, representing the test site. Objects surrounding the PV system were neglected, and the materials of the objects in the model, such as the reference cells and the rails along the roof, are not identical to the materials on the test site in terms of material properties, reflectance, and albedo. The 3D model was used to simulate the irradiance on the PV system for the three reference cell positions on the test site. The results show good compliance between measured and simulated irradiance most days on a daily basis, but there are some deviations between the simulated irradiance, especially during the winter. For the simulated months August 2022 – March 2023, except September, the percentage difference between simulated and measured irradiance deviates in the range of 5.06 % – 16.54 %.

Shading from the objects surrounding the test site was neglected in the 3D model, but they may cause shading on the test site, especially in the winter due to the lower altitude of the Sun. Hence, neglected shading may cause a deviation in measured and simulated irradiance. Snow on the other hand may some days cover the test site and the reference cells, and therefore, result in non or low-measured irradiance from the reference cells. Consequently, the deviation between simulated and measured irradiance can increase, which makes snow a likely explanation for a percentage difference in the range of 10.67 % – 16.54 % during the months with snowfalls. Hence, it is harder to retrieve good results when there is snow covering the PV system. The 3D model uses irradiance data from the radiometers mounted higher above the roof than the reference cells, these can also be covered in snow, but the snow falls off easier.

Factors such as the positioning of the objects, orientation, and angle of incidence (AOI) have a significant impact on the simulated irradiance. The test site was assumed to have an orientation of 86° from Google Earth Pro. Not only is there uncertainty in this value, but placing all the objects in bifacial_radiance to the exact orientation is difficult. As a few degrees in orientation affect the irradiance, this may affect the performance of the 3D model. Losses due to AOI are hard to implement as the vertical mounting ensures irradiance on both sides of the solar panel the whole day. It is clear that this is a factor reducing the irradiance, and therefore, should be investigated more.

Lastly, albedo is an important parameter when simulating the irradiance. Hence, the albedo measured from the test site was used. The albedo is varying between 0

and 1, but for some days during the winter, the albedo at the test site exceeds 1. Therefore, the downward pyranometer measuring reflected irradiance also seem to detect direct irradiance for some days. This may affect the irradiance and result in a deviation between simulated and measured irradiance during the winter.

In other words, there are many factors present when simulating the irradiance. From the work done in this thesis, bifacial_radiance gives a rough estimate of the expected irradiance to a PV system as the largest percentage difference at 16.54 % between simulated and measured irradiance happens in December. Hence a simple detailed model of the PV system, where surrounding objects causing shading, snow, orientation, etc. have been neglected gives a good insight into the expected irradiance. If these factors are considered when developing the 3D model, bifacial_radiance has the potential to deliver more accurate irradiance simulations with a lower deviation from the measured irradiance. While bifacial_radiance is time efficient when simulating the irradiance for a longer period of time using a cumulative sky, the software is time-consuming when simulating the irradiance daily on an hourly interval.

The simulated DC and AC power output on a daily basis with the singlediode model from pvlib gives rough estimations of the DC and AC power, but there are deviations between simulated and measured power, especially during the winter. An important factor during the winter is snow as the solar panels receive non-to-low irradiance if covered in snow. As a result, there will be a large deviation between simulated and measured power, making it hard to estimate the generated power. Following errors from the simulated irradiance and system losses such as shading are also important factors that may cause deviation in the results as the PV system may suffer from shading when the irradiance from the radiometers and the reference cells does not suffer from shading.

From the simulated DC and AC power, the inverter efficiency reaches approximately 90 % when the generated DC power exceeds 200 W. This is lower than typical inverter efficiencies which are between 95 % and 98 %. The inverter on the test site is underdimentioned for the PV system as the installed capacity is 1440 W and the DC input in the inverter is 3400 W. Hence, the efficiency and the AC power could have been higher with a smaller inverter.

On a monthly basis when the irradiance from a cumulative sky was used, the results show a large deviation between simulated and measured DC energy. Between simulated DC energy from simulated irradiance and measured DC energy, the percentage difference ranges between 28.42 % and 119.58 %. Hence, for some months the energy model gives a rough estimation of the energy output, but as the percentage difference exceeds 100 % the results for some periods are not usable. The high percentage difference happens in months with snow, making snow an important parameter to consider for good estimations of the energy output. The percentage difference between simulated DC energy from measured irradiance and measured DC energy on the other hand is in the range 28.29 % – 109.03 %. As the measured irradiance is retrieved from reference cells in the PV system, the deviations make it likely that system losses such as shading and snow on the solar panels have a significant impact on the energy. Hence, implementing these factors is important to develop a more accurate model for simulating energy.

6 Further work

6.1 Data

Irradiance

The irradiance measurements used as input to bifacial_radiance were in 2022 retrieved from two data loggers, DNI from one and GHI, DHI, and albedo from another. Hence, there may be some differences in how data have been retrieved and aggregated to 5-minute intervals. Also, a lightning strike close to the test site the 17^{th} of August 2022 affected the logger registering DNI for some time. Hence, the DNI was calculated using equation 3 with measured data for GHI and DHI. Mostly there var good compliance between measured and calculated DNI, so the measured DNI was used in this thesis. Still, validating the measurements for GHI, DHI, DNI, and albedo further as well as investigating the uncertainty in logging and timestamps of data can result in stronger conclusions.

Data used when simulating the power and energy

The data retrieved from the monitoring systems SolarEdge and VCOM may as mentioned, be retrieved and aggregated differently. Also, the timestamps in the compared data are different due to the 15-minute interval from SolarEdge and the 5-minute interval in VCOM. This may affect the results, and therefore, the irradiance, power, and energy simulations should be validated using data with the same time interval. How the data is aggregated in the two monitoring systems should also be investigated to ensure the comparison of equal data for stronger conclusions.

6.2 The 3D model and simulating the irradiance

The 3D model created in bifacial_radiance in this thesis gives a rough estimate of the expected irradiance for a PV system. For more accurate irradiance results more details need to be implemented. Some proposals are mentioned below.

Orientation of the PV system

Ensuring that the 3D model is oriented as precisely as possible in relation to the test site is important for accurate irradiance simulation. Hence, the orientation of the solar panels and the reference cells on the test site needs to be validated. This can be done by for example using measurements from the test site together with trigonometry.

The 3D model

The objects surrounding the PV system can be included for more accurate shadings on the PV system, as well as update the materials to include the same material properties as the corresponding objects on the test site. Taking the shadings into account may improve the power/energy simulated as it seems that shading has an impact on the results.

Positioning the objects in the 3D model is time-consuming using bifacial_radiance, but validating the placement of the objects in relation to the test site is important for accurate results. Especially the positioning of the sensors used to simulate the irradiance as they are not in the exact same place as on the test site.

Angle of incidence

As bifacial_radiance does not take losses due to AOI into account, this needs to be manually added to the simulated irradiance from bifacial_radiance. Investigating and validating methods for simulating the irradiance when losses due to AOI are taken into account is important as it affects the irradiance. Also, how to take these losses into account when the solar panels only receive diffuse irradiance needs to be investigated further.

As these losses need to be added manually to the simulated irradiance for all the sensor positions in bifacial_radiance, generalizing a model calculating the losses due to AOI and taking them into account should be developed for time-efficiency.

Generalizing the 3D model

The 3D model in this master's thesis is site specific to the test site at IFE. Hence, for the model to fit other vertically mounted PV systems from Over Easy Solar AS, the model needs to be generalized. Generalizing the 3D model of the test site, such as the one in this thesis with solar panels and rails along the roof can be done easily. One way is to create a function for making the PV system where the materials of the components are defined according to a typical PV system from Over Easy Solar AS. The data specific to the site can be imported as input. This can give a rough estimate of the expected irradiance as discussed in this thesis.

For more accurate simulations, implementing the surrounding objects to retrieve the correct shading on and around the 3D model can be important. Adding these additional objects with the correct material and material properties to a generalized code is difficult as this is site-specific.

Time-efficiency

Simulating the irradiance using bifacial_radiance is time-consuming. Simulating the daily irradiance using a 5-minute interval in data takes several hours, and using hourly intervals takes approximately 40 minutes. Thus, simulating a longer period of time with this resolution takes a long time. Using a cumulative sky on the other hand is more efficient, but only gives one irradiance value for a longer period of time such as a week, a month, or a year. If one wants to simulate irradiance with for example an hourly interval for a longer period of time to retrieve the variations in irradiance more efficiently, other software should be validated. Some examples are Honeybee Radiance and ClimateStudio.

6.3 Simulating the power and energy

System losses

Taking system losses such as shading into account is important to retrieve more

accurate power and energy simulations. Shading on the PV system from objects surrounding the PV system will affect the generated power and energy and hence, have a significant impact on the results. The impact of such parameters is important to determine. Snow is also an important parameter that can cover the solar panels and reduce the generated power and energy. Such factors are necessary to take into account when simulating the power and energy of a PV system for areas where there is snow during the winter in order to retrieve accurate estimations. A better model for simulating the power and from simulated irradiance should be developed, either with a more complex model using pvlib or with other software.

Simulating AC power and energy

While it seems that the default values used in the inverter model for simulating AC power in this thesis work, implementing actual data about the inverter can give a better view of the results and result in better conclusions.

The inverter model used in this thesis does not work to simulate the AC energy for a longer period of time when a cumulative sky in bifacial_radiance is used to simulate the irradiance, as variation in DC energy is needed. Hence, investigating how AC energy can be simulated can be interesting.

References

[1] IEA. Renewable Electricity, 2022. Accessed: 2023-02-16.

[2] UN. Paris agreement, 2015. Accessed: 2023-04-20.

[3] B. D. Dimd, S. Völler, U. Cali, and O. M. Midtgård. A review of machine learning-based photovoltaic output power forecasting: Nordic context. *IEEE Access*, 10:26404–26425, 2022. DOI: 10.1109/ACCESS.2022.3156942. Accessed: 2023-04-16.

[4] E. Martiniussen. 22 ble et rekordår for norsk solenergi, 2023. Accessed: 2023-01-19.

[5] Energipluss. Solceller i Norge - solenergi effektivt i norsk klima, 2021. Accessed: 2023-04-18.

[6] NVE. Solkraft, 2023. Accessed: 2023-01-24.

[7] R. Guerrero-Lemus, R. Vega, T. Kim, A. Kimm, and L. E. Shephard. Bifacial solar photovoltaics – a technology review. *Renewable and Sustainable Energy Reviews*, 60:1533–1549, 2016. ISSN 1364-0321. DOI: `https://doi.org/10.1016/j.rser.2016.03.041`. Accessed: 2023-01-06.

[8] J. Stein, C. Reise, J. B. Castro, G. Friesen, G. Maugeri, E. Urrejola, and S. Ranta. Bifacial photovoltaic modules and systems: Experience and results from international research and pilot applications. 4 2021. DOI: 10.2172/1779379. Accessed: 2023-02-16.

[9] Over Easy Solar AS. About Over Easy, 2021. Accessed: 2023-01-03.

[10] Tryge Mongstad, Personal Communication.

[11] Over Easy Solar AS. Flat roof solar, 2021. Accessed: 2023-01-03.

[12] Over Easy Solar AS. Green roof solar, 2021. Accessed: 2023-01-03.

[13] Energisenteret. Sol. Accessed: 2023-02-14.

[14] O. Isabella, K. Jäger, A. Smets, R. van Swaaij, and M. Zeman. *Solar Energy: The Physics and Engineering of Photovoltaic Conversion, Technologies and Systems*. UIT Cambridge Ltd., 2016. ISBN 1906860327,9781906860325. Accessed: 2023-01-06.

[15] J. Kennewell and A. McDonald. The solar constant. Accessed: 2023-01-20.

[16] L. Gu and A. Robles-Kelly. Shadow modelling based upon rayleigh scattering and mie theory. *Pattern Recognition Letters*, 43:89–97, 2014. ISSN 0167-8655. ICPR2012 Awarded Papers.

[17] P. Pérez-Higueras and E. F. Fernández. High concebtrator photovoltaics. fudamentals, engineering and power plants, 2015. Accessed: 2023-01-06.

[18] M. Gul, Y. Kotak, T. Muneer, and S. Ivanova. Enhancement of albedo for solar energy gain with particular emphasis on overcast skies. *Energies*, 11 (11):2881, Oct 2018. ISSN 1996-1073. DOI: 10.3390/en11112881. Accessed: 2023-02-16.

[19] C. Wynn. An introduction to brdf-based lighting. *Nvidia Corporation*, 2000. Accessed: 2023-04-26.

[20] D. C. Martinsen. Performance modeling of bifacial pv power plants in a nordic climate. Master's thesis, NTNU, 2022. Accessed: 2023-02-23.

[21] Y. Qu, S. Liang, Q. Liu, T. He, S. Liu, and X. Li. Mapping surface broadband albedo from satellite observations: A review of literatures on algorithms and products. *Remote Sensing*, 7:990–1020, 01 2015. doi: 10.3390/rs70100990. Accessed: 2023-04-26.

[22] Y. Kotak, M. Gul, T. Muneer, and S. Ivanova. 04 2015. Investigating the Impact of Ground Albedo on the Performance of PV Systems. Accessed: 2023-02-16.

[23] A. Z. Ramírez and C. B. Muñoz. Albedo effect and energy efficiency of cities. 2012. Accessed: 2023-02-17.

[24] A. A. Shishavan. *Bifacial photovoltaic (PV) system performance modeling utilizing ray tracing*. PhD thesis, University of Iowa, 2019. Accessed: 2023-01-11.

[25] G. Lobaccaro, S. Carlucci, S. Croce, R. Paparella, and L. Finocchiaro. Boosting solar accessibility and potential of urban districts in the nordic climate: A case study in trondheim. *Solar Energy*, 149:347–369, 2017. ISSN 0038-092X. DOI: `https://doi.org/10.1016/j.solener.2017.04.015`. Accessed: 2023-03-10.

[26] A. Granlund, J. Narvesjö, and A. M. Petersson. The influence of module tilt on snow shadowing of frameless bifacial modules. In *36th European Photovoltaic Solar Energy Conference and Exhibition, Marseille, September 9-13, 2019*, pages 1650–1654, 2019. Accessed: 2023-04-02.

[27] A. Joshi, A. Khan, and A. Sp. Comparison of half cut solar cells with standard solar cells. pages 1–3, 2019. DOI: 10.1109/ICASET.2019.8714488. Accessed: 2023-03-14.

[28] A simulation study to evaluate and compare monofacial vs bifacial perc pv cells and the effect of albedo on bifacial performance. *Materials Today: Proceedings*, 46:5242–5247, 2021. ISSN 2214-7853. International Conference on Innovations in Clean Energy Technologies (ICET2020).

[29] O. R. Valmot. Den viktigste overgangen du ikke har hørt om, 2021. Accessed: 2023-05-02.

[30] A. P. Dobos. Pvwatts version 5 manual. 9 2014. DOI: 10.2172/1158421. Accessed: 2023-02-01.

[31] W. F. Holmgren, C. W. Hansen, and M. A. Mikofski. pvlib python: a python package for modeling solar energy systems. *Journal of Open Source Software*, 3(29):884, 2018. DOI: `https://doi.org/10.21105/joss.00884`. Accessed: 2023-02-23.

[32] A. El Tayyan. A simple method to extract the parameters of the single-diode model of a pv system. *Turkish Journal of Physics*, 37:121 – 131, 03 2013. doi: 10.3906/fiz-1206-4.

[33] K. V. Vidyanandan. An overview of factors affecting the performance of solar pv systems. *Energy Scan*, 27(28):216, 2017. Accessed: 2023-05-03.

[34] R. Mallwitz and B. Engel. *Solar power inverters*. 2010. Accessed: 2023-02-01.

[35] C.-Y. Park, S.-H. Hong, S.-C. Lim, B.-S. Song, S.-W. Park, J.-H. Huh, and J.-C. Kim. Inverter efficiency analysis model based on solar power estimation using solar radiation. *Processes*, 8(10):1225, Oct 2020. ISSN 2227-9717. DOI: http://dx.doi.org/10.3390/pr8101225. Accessed: 2023-05-09.

[36] R. Kopecek and J. Libal. Bifacial photovoltaics 2021: Status, opportunities and challenges. *Energies*, 14(8):2076, Apr 2021. ISSN 1996-1073. DOI: 10.3390/en14082076. Accessed: 2023-01-06.

[37] C. A. Deline, S. A. Pelaez, W. F. Marion, W. R. Sekulic, A. Michael Woodhouse, and J. Stein. Bifacial pv system performance: Separating fact from fiction, 7 2019. DOI: 10.13140/RG.2.2.23189.27365. Accessed: 2023-04-19.

[38] I. Shoukry, J. Libal, R. Kopecek, E. Wefringhaus, and J. Werner. Modelling of bifacial gain for stand-alone and in-field installed bifacial pv modules. *Energy Procedia*, 92:600–608, 2016. ISSN 1876-6102. Proceedings of the 6th International Conference on Crystalline Silicon Photovoltaics (SiliconPV 2016).

[39] J. Appelbaum. The role of view factors in solar photovoltaic fields. *Renewable and Sustainable Energy Reviews*, 81:161–171, 2018. ISSN 1364-0321. DOI: https://doi.org/10.1016/j.rser.2017.07.026. Accessed: 2023-04-14.

[40] D. Yang. Solar radiation on inclined surfaces: Corrections and benchmarks. *Solar Energy*, 136:288–302, 2016. ISSN 0038-092X. DOI: https://doi.org/10.1016/j.solener.2016.06.062. Accessed: 2023-03-14.

[41] K.N. Shukla, S. Rangnekar, and K. Sudhakar. Comparative study of isotropic and anisotropic sky models to estimate solar radiation incident on tilted surface: A case study for bhopal, india. *Energy Reports*, 1:96–103, 2015. ISSN 2352-4847. DOI: https://doi.org/10.1016/j.egyr.2015.03.003. Accessed: 2023-03-14.

[42] C. Demain, M. Journée, and C. Bertrand. Evaluation of different models to estimate the global solar radiation on inclined surfaces. *Renewable Energy*, 50:710–721, 2013. ISSN 0960-1481. DOI: https://doi.org/10.1016/j.renene.2012.07.031. Accessed: 2023-04-20.

[43] Google Earth Pro 7.3. *Kjeller, Norway*. 59,97314°N 11,05163°E. Accessed: 2023-03-04.

[44] D. Yang, Z. Ye, A. M. Nobre, H. Du, W. M. Walsh, L. I. Lim, and T. Reindl. Bidirectional irradiance transposition based on the perez model. *Solar Energy*, 110:768–780, 2014. ISSN 0038-092X. DOI: https://doi.org/10.1016/j.solener.2014.10.006. Accessed: 2023-01-24.

[45] S. A. Pelaez and C. Deline. bifacial_radiance: a python package for modeling bifacial solar photovoltaic systems. *Journal of Open Source Software*, 5(50): 1865, 2020. DOI: 10.21105/joss.01865 Accessed: 2023-01-19.

[46] M. Sengupta, A. Habte, S. Wilbert, C. Gueymard, and J. Remund. Best practices handbook for the collection and use of solar resource data for solar energy applications: Third edition. 4 2021. DOI: DOI: https://dx.doi.org/10.2172/1778700. Accessed: 2023-02-17.

[47] J. Meydbray, K. Emery, and S. Kurtz. Pyranometers and reference cells, what's the difference?: Preprint. 3 2012. URL: https://www.osti.gov/biblio/1038336. Accessed: 2023-01-24.

[48] SOLYS2 Sun Tracker. Accessed: 2023-01-24.

[49] Photovoltaic Reference Cells for PV Monitoring. Accessed: 18.01.2023.

[50] H. N. Riise and M. Øgaard and T. Nærland. Soiling and snow impact on a PV plant at a farm in Norway. *38th European Photovoltaic Solar Energy Conference and Exhibition*, 2021. Accessed: 2023-04-20.

[51] J. R. Taylor. *Introduction to Error Analysis: The study of uncertainties in physical measurements*. University Science Books,U.S., 1997. ISBN 9780935702750. Accessed: 2023-05-11.

[52] Meteorologisk institutt, Statens kartverk and Norges vassdrags- og energidirektorat. 2006. senorge.no. Accessed: 2023-05-05.

[53] D.C. Martinsen and M.B. Øgaard and M.M. Nygård and M. Syre Wiig and M. Di Sabatino and E.S. Marstein and H.N. Riise. Evaluation of Irradiance Decomposition and Transposition Models for a Nordic Climate. *8th World Conference on Photovoltaic Energy Conversion*, 2022. Accessed: 2023-04-20.

[54] H. Taha, D. J. Sailor, and H. Akbari. High-albedo materials for reducing building cooling energy use. 1992. Accessed: 2023-04-02.

A Datasheet for the pyranometer

KIPP & ZONEN

an OTT HydroMet brand

CMP10 | CMP11 | SMP10 | SMP11

Applications

Solar Monitoring for PV
Weather Services and Research
Climatology
Industrial Test Chambers

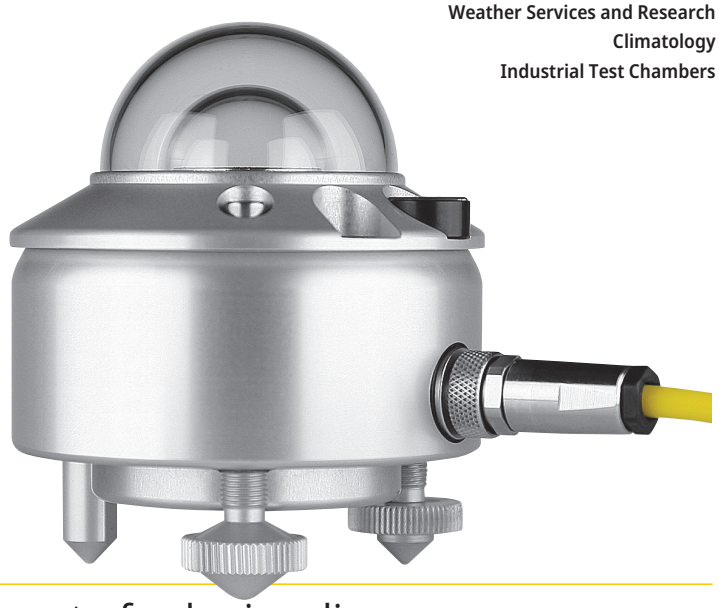

Pyranometer

For accurate measurement of solar irradiance

IEC61724 Class A
ISO 9060 Spectrally Flat Class A
The solar energy industry standard
Accurate and independent data for performance ratio calculations
Analog and digital outputs
5 year warranty

ISO 9060 & IEC 61724 Class A

Models CMP10, CMP11, SMP10 and SMP11 are the high quality pyranometers that are most commonly used in meteorological networks and solar energy applications around the world and all comply with Class A of ISO 9060 and IEC 61724.

Analog or digital outputs

CMP10 and CMP11 do not require any power. Incoming solar radiation generates a continuous millivolt output, which is converted in a data logger to irradiance in W/m² using the calibrated sensitivity. For easy integration into SCADA systems SMP10 and SMP11 have Modbus® RTU RS-485 serial communication, plus an amplified analog output. The sensitivity is stored inside for standardized outputs and they feature improved response time and better temperature compensation.

With or without drying cartridge

To prevent internal condensation, pyranometers are fitted with a desiccant to keep the internal humidity low and the accuracy high. CMP11 and SMP11 have an external drying cartridge with a desiccant that needs regular inspection and replacement every 3 to 6 months, depending on the local climate conditions. To save maintenance time and cost, CMP10 and SMP10 have internal desiccant that lasts up to 10 years.

5 Year Warranty

All pyranometers from Kipp & Zonen come with a 5 year warranty and we have service and calibration centers around the world.

OTT HydroMet

Technical Specifications

	CMP10 | CMP11	SMP10 | SMP11
Classification to ISO 9060:2018	Spectrally Flat Class A	Spectrally Flat Class A
Sensitivity	7 to 14 µV/W/m²	-
Impedance	10 to 100 Ω	-
Expected output range (0 to 1500 W/m²)	0 to 20 mV	-
Maximum operational irradiance	4000 W/m²	-
Analog output • V-version	-	0 to 1 V
Analog output range*	-	-200 to 2000 W/m²
Analog output • A-version	-	4 to 20 mA
Analog output range*	-	0 to 1600 W/m²
Serial output	-	RS-485 Modbus®
Serial output range	-	-400 to 4000 W/m²
Response time (63 %)	< 1.7 s	< 0.7 s
Response time (95 %)	< 5 s	< 2 s
Spectral range (20 % points)	270 to 3000 nm	270 to 3000 nm
Spectral range (50 % points)	285 to 2800 nm	285 to 2800 nm
Zero offsets (unventilated) (a) thermal radiation (at 200 W/m²) (b) temperature change (5 K/h)	 < 7 W/m² < 2 W/m²	 < 7 W/m² < 2 W/m²
Non-stability (change/year)	< 0.5 %	< 0.5 %
Non-linearity (100 to 1000 W/m²)	< 0.2 %	< 0.2 %
Directional response (up to 80 ° with 1000 W/m² beam)	< 10 W/m²	< 10 W/m²
Spectral selectivity (350 to 1500 nm)	< 3 %	< 3 %
Tilt response (0 ° to 90 ° at 1000 W/m²)	< 0.2 %	< 0.2 %
Temperature response	< 1 % (-10 °C to +40 °C)	< 0.3 % (-20 °C to +50 °C) < 0.3 % (-40 °C to +70 °C)
Field of view	180 °	180 °
Accuracy of bubble level	< 0.1 °	< 0.1 °
Power consumption (at 12 VDC)	-	V-version: 55 mW A-version: 100 mW
Supply voltage	-	5 to 30 VDC
Software, Windows™	-	SmartExplorer Software, for configuration, test and data logging
Detector type	Thermopile	Thermopile
Operating and storage temperature range	-40 °C to +80 °C	-40 °C to +80 °C
Humidity range	0 to 100 %	0 to 100 %
MTBF (Mean Time Between Failures)	> 10 years	> 10 years **
Ingress Protection (IP) rating	67	67
Recommended applications	Meteorological networks, PV panel and thermal collector testing, materials testing	High performance for PV panel and thermal collector testing, solar energy research, solar prospecting, materials testing, advanced meteorology and climate networks

Note: **The performance specifications quoted are worst-case and/or maximum values.**
*** adjustable with SmartExplorer Software | ** extrapolated after introduction in January 2012**

Dimensions

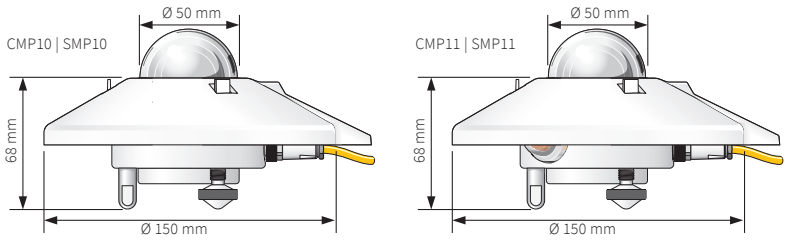

OTT HydroMet B.V. | solar-info@otthydromet.com | www.otthydromet.com

OTT HydroMet

KIPP & ZONEN
an OTT HydroMet brand

ME-KZ-RE-ds-CMP10_CMP11_SMP10_SMP11-EN_20220829

B Datasheet for the pyrheliometer

KIPP & ZONEN

CHP1 | SHP1

Applications

Weather Services and Research
Meteorology
Concentrated Solar Power

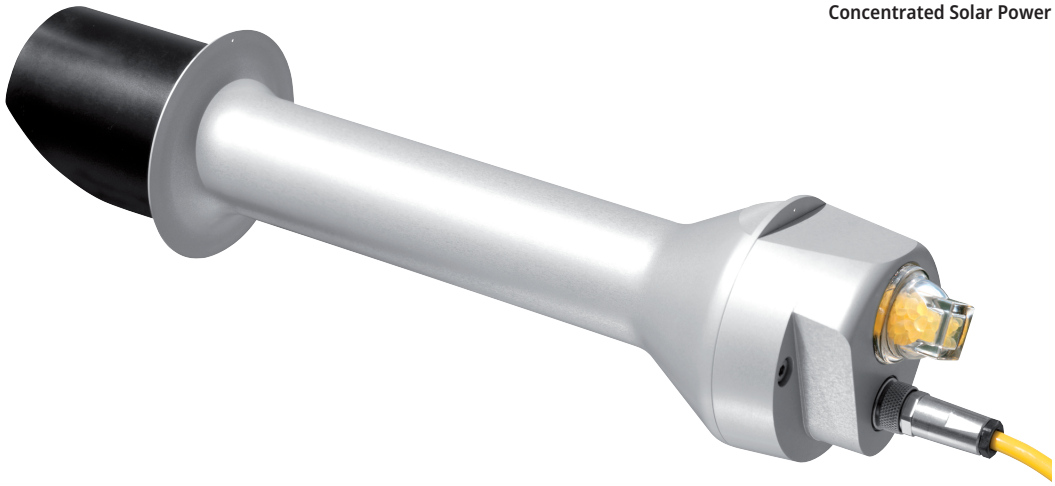

Pyrheliometer

For direct normal incidence solar radiation measurement

Most accurate DNI measurement for CSP
Used in the global BSRN network
ISO 9060 Class A
Analog and digital outputs
5 year warranty

Field of view of 5°

A pyrheliometer is an instrument designed specifically to measure DNI (Direct Normal Incidence) with a field of view of 5°. This is achieved by the shape of the collimation tube, with precision apertures, and the detector design.

Analog or digital outputs

CHP1 Pyrheliometer is a pyrheliometer that offers reliability and durability without requiring any power. The analog outputs allow easy connection to virtually any data logger. SHP1 has a Modbus® interface plus amplified analog output, improved response time and temperature corrected measurement data

Pyrheliometers mounted on sun trackers

A pyrheliometer needs to be pointed accurately at the sun at all times. Kipp & Zonen sun trackers provide a stable mounting to keep the pyrheliometer pointing at the sun to accurately measure DNI.

Meteorology Division of OTT HydroMet

Technical Specifications

	CHP1	SHP1
Classification to ISO 9060:2018	Spectrally Flat Class A	Spectrally Flat Class A
Sensitivity	7 to 14 µV/W/m²	-
Expected output range (0 to 1400 W/m²)	10 to 20 mV	-
Maximum operational irradiance	4000 W/m²	-
Analog output • V-version	-	0 to 1 V
Analog output range*	-	-200 to 2000W/m²
Analog output • A-version	-	4 to 20 mA
Analog output range*	-	0 to 1600 W/m²
Serial output	-	RS-485 Modbus® RTU
Serial output range	-	-400 to 4000 W/m²
Response time (63 %)	< 1.7 s	< 0.7 s
Response time (95 %)	< 5 s	< 2 s
Spectral range (50 % points)	200 to 4000 nm	200 to 4000 nm
Zero offsets (unventilated) (b) temperature change (5 K/h)	< 1 W/m²	< 1 W/m²
Non-stability (change/year)	< 0.5 %	< 0.5 %
Non-linearity (0 to 1000 W/m²)	< 0.2 %	< 0.2 %
Spectral selectivity (350 to 1500 nm)	< 1 %	< 1 %
Required sun tracker accuracy	< 0.5 ° from ideal	< 0.5 ° from ideal
Weight (excluding cable)	0.9 kg	0.9 kg
Slope angle	1 ° ±0.2 °	1 ° ±0.2 °
Temperature response	< 0.5 % (-20 °C to +50 °C)	< 0.5 % (-30 °C to +60 °C) < 1 % (-40 °C to +70 °C)
Field of view	5 ° ±0.2 °	5 ° ±0.2 °
Power consumption (at 12 VDC)	-	V-version: 55 mW A-version: 100 mW
Supply voltage	-	5 to 30 VDC
Software, Windows™	-	SmartExplorer Software, for configuration, test and data logging
Operating and storage temperature range	-40 °C to +80 °C	-40 °C to +80 °C
Humidity range	0 to 100 %	0 to 100 %
MTBF (Mean Time Between Failures) **	> 10 years	> 10 years
Ingress Protection (IP) rating	67	67
Recommended applications	High performance direct radiation monitoring for meteorological stations or concentrated solar energy applications	High performance direct radiation monitoring for meteorological stations or concentrated solar energy applications

Note: **The performance specifications quoted are worst-case and/or maximum values.**
*** adjustable with SmartExplorer Software**

Dimensions

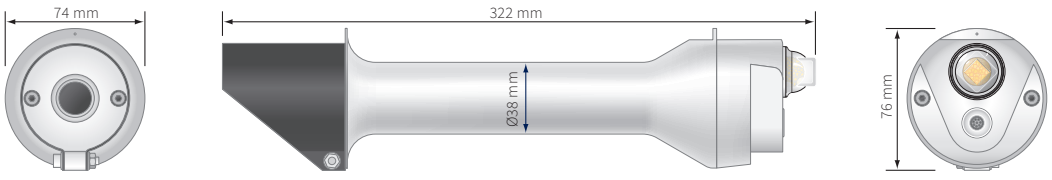

Single Phase Inverter with HD-Wave Technology

INVERTERS

SE2200H, SE3000H, SE3500H, SE3680H,
SE4000H, SE5000H, SE6000H

Optimized installation with HD-Wave technology

- Specifically designed to work with power optimizers
- Record-breaking efficiency
- Extremely small, lightweight and easy to install
- High reliability
- Built-in module-level monitoring
- Outdoor and indoor installation
- Fixed voltage inverter for longer strings
- Smart Energy Management control
- Advanced safety feature - integrated arc fault protection
- Compatible with the StorEdge Interface for StorEdge™ applications

solaredge.com

solaredge

/ Single Phase Inverter with HD-Wave Technology

SE2200H, SE3000H, SE3500H, SE3680H, SE4000H, SE5000H, SE6000H

	SE2200H	SE3000H	SE3500H	SE3680H	SE4000H	SE5000H	SE6000H	
OUTPUT								
Rated AC Power Output	2200	3000	3500	3680	4000	5000[1]	6000	VA
Maximum AC Power Output	2200	3000	3500	3680	4000	5000[1]	6000	VA
AC Output Voltage (Nominal)	220/230							Vac
AC Output Voltage Range	184 - 264.5							Vac
AC Frequency (Nominal)	50/60 ± 5							Hz
Maximum Continuous Output Current	10	14	16	16	18.5	23	27.5	A
Utility Monitoring, Islanding Protection, Configurable Power Factor, Country Configurable Thresholds	Yes							
INPUT								
Maximum DC Power	3400	4650	5425	5700	6200	7750[2]	9300	W
Transformer-less, Ungrounded	Yes							
Maximum Input Voltage	480							Vdc
Nominal DC Input Voltage	380							Vdc
Maximum Input Current	6.5	9	10	10.5	11.5	13.5	16.5	Adc
Reverse-Polarity Protection	Yes							
Ground-Fault Isolation Detection	600kΩ Sensitivity per Unit							
Maximum Inverter Efficiency	99.2							%
European Weighted Efficiency	98.3	98.8				99		%
Nighttime Power Consumption	< 2.5							W
ADDITIONAL FEATURES								
Supported Communication Interfaces	RS485, Ethernet, ZigBee (optional), WiFi (optional), Cellular (optional)							
Smart Energy Management	Export Limitation, Smart Energy, StorEdge Applications							
Arc Fault Protection	Integrated, User Configurable (According to UL1699B)							
STANDARD COMPLIANCE								
Safety	IEC-62109-1/2, AS-3100							
Grid Connection Standards	AS-4777, VDE-AR-N-4105, VDE 0126-1-1, UTE C15-712, G83/2, G59/3, CEI-021, EN 50438, IEC61727, IEC62116, ÖNORM, TF3.2.1, C10-11, NRS 097-2-1							
Emissions	IEC61000-6-2, IEC61000-6-3, IEC61000-3-11, IEC61000-3-12, FCC Part 15 Class B							
INSTALLATION SPECIFICATIONS								
AC Output - Supported Cable Diameter	9-16							mm
AC - Supported Wire Cross Section	1-13							mm^2
DC Input	1 x MC4				2 x MC4 pair			
Dimensions (H x W x D)	280 x 370 x 142							mm
Noise	< 25							dBA
Weight	7.8					9	10.6	kg
Cooling	Natural Convection							
Operating Temperature Range	-20 to +60[3] (-40˚C option)							˚C
Protection Rating	IP65 — Outdoor and Indoor							

[1] 4600VA in Germany
[2] 7130VA in Germany
[3] For power de-rating information refer to: https://www.solaredge.com/sites/default/files/se-temperature-derating-note.pdf

CE RoHS

D Scripts

The important scripts created to develop the 3D model and to carry out the analyses performed in this master's thesis have been attached as a ZIP file and are available on GitHub in the repository *Simulation-of-a-vertical-bifacial-PV-system-compared-to-measured-values*. To get to the GitHub repository, the following link can also be used:

`https://github.com/amalierob/Simulation-of-a-vertical-bifacial-PV-system-compared-to-measured-values`

The included scripts are described below and are site-specific for the test site studied in this master's thesis. A few generalizations have been done in the attached files, and modified versions have been used to retrieve all the results reported in this thesis.

Weather file

This file incorporates the script developed to create the weather files with the columns of a TMY file from measured data for GHI, DHI, DNI, and albedo. The files are created in the UTC timezone and are implemented in bifacial_radiance by using right-labeled data, i.e. with a shift of -30 minutes, and instantaneous values based on a 5-minute interval to represent the data for an hour.

Uncertainty analysis

This file incorporates the script to estimate the measurement uncertainty in the data measured by the pyranometers and pyrheliometer on the test site. These functions were developed in Ref. [20], and can be found on the GitHub repository Performance-modeling-of-Bifacial-PV-Power-Plants-in-a-Nordic-Climate. These functions are using parameters defined in the calibration certificates and the data sheet of the pyranometer and pyrheliometer together with JCGM 100:2008 GUM Evaluation of measurement data [20].

3D model and simulating the irradiance

This file incorporates both the 3D model developed and how the irradiance was simulated using the 3D model. After the sky was generated, the 3D model was created before the sensor positions were defined to simulate the irradiance for the front and the rear side of the reference cells. The script shows an example of one of the time periods simulated, modified versions of the script were used to simulate other time periods.

The sky was generated with two approaches from the imported weather data, one where the sky represents one timestamp and the other one a cumulative sky to represent the sky for a longer period of time. The example in the script illustrates the case where the sky represents one timestamp to simulate the irradiance for one day with an hourly interval.

The 3D model was built with objects corresponding to the dimensions, angles, and positions of the objects on the test site as described in 3.2.1. Still, the model

was simplified to only include the PV system and the rails along the roof. Hence, surrounding objects were neglected.

Angle of incidence

This file incorporates angle of incidence (AOI) calculations using specific parameters from the test site to retrieve the irradiance where losses due to AOI have been taken into account.

Power simulation

This file incorporates the script created to simulate the DC and AC power on the test site using the average irradiance and temperature. This was done for both simulated and measured irradiance. Modifications of this script were used to retrieve results for all time periods and for the case of the cumulative sky. For the case of cumulative sky, the DC energy was simulated but the AC energy was omitted.

Materials.rad

This file incorporates all the RADIANCE default materials included in bifacial_radiance software. The materials used to create the 3D model in this thesis were *stock glass*, *Metal_Grey*, and *black*.

README.md

This file incorporates a short description of the files included in the repository as given above.

E Simulated irradiance compared to measured irradiance

E.1 Clear-sky days

The 12^{th} of August 2022

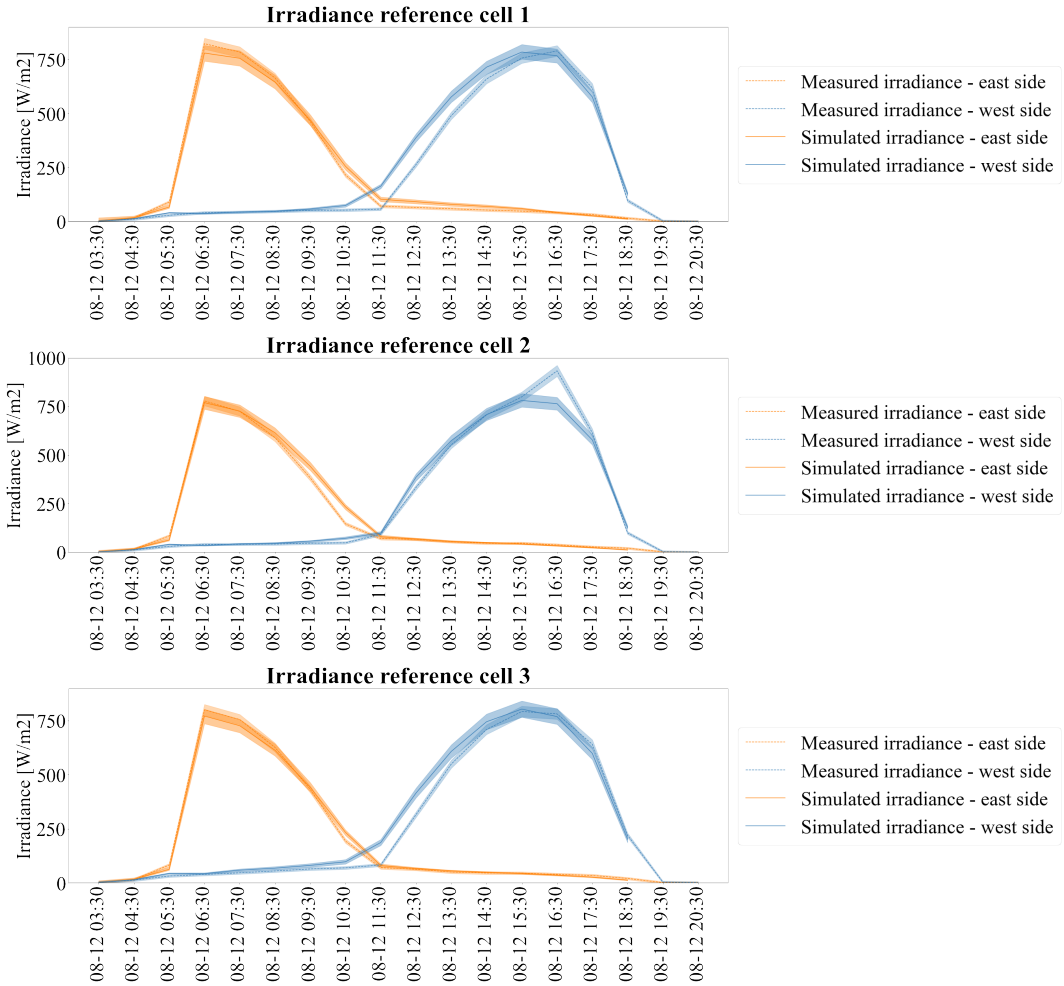

Figure 49: *Simulated and measured irradiance for the* 12^{th} *of August 2022. The measurement uncertainty shown as shaded areas is for simulated irradiance due to GHI, DHI, DNI, and albedo, while the measured irradiance has a measurement uncertainty of* ± 2.5 *%* ± 5 $\mathrm{W/m^2}$.

The 12^{th} of August 2022 - 5-minute interval

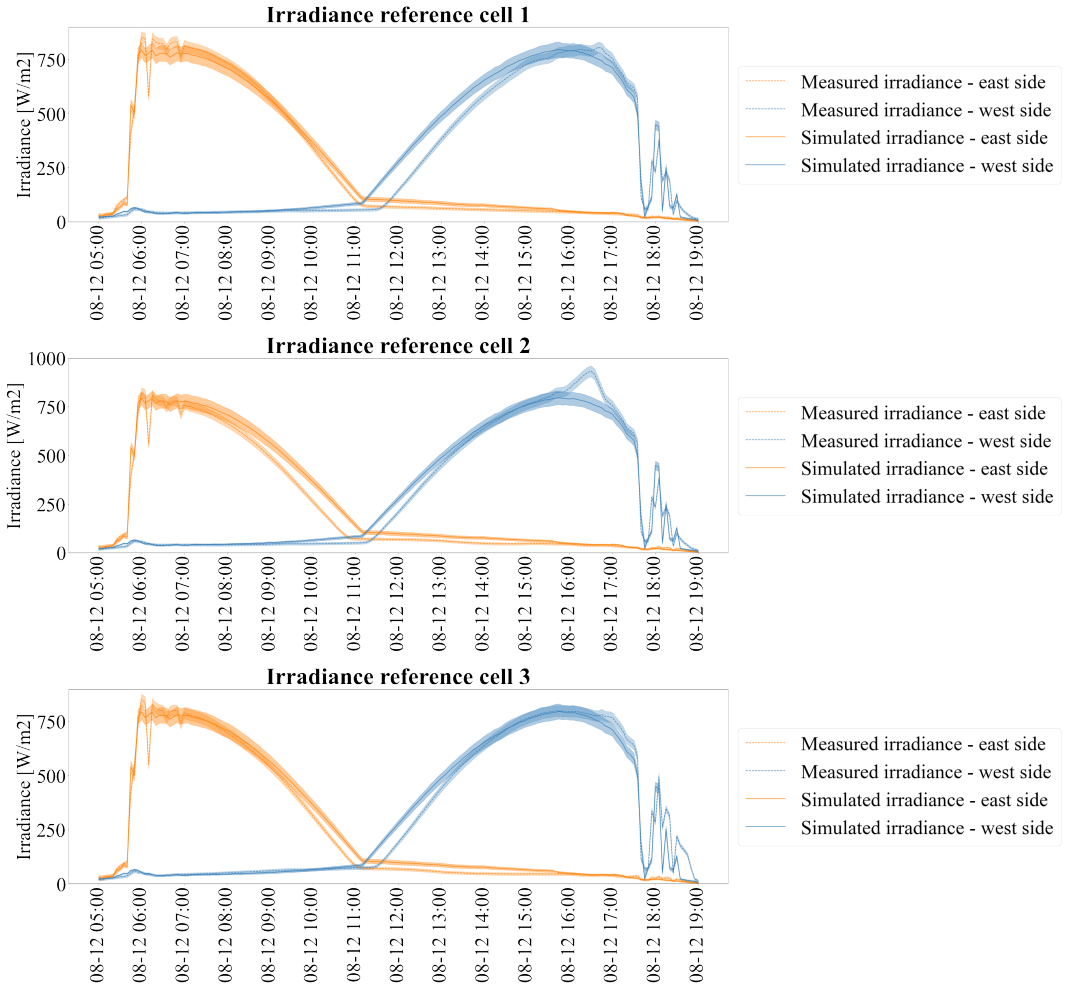

Figure 50: *Simulated and measured irradiance for the* 12^{th} *of August 2022. The measurement uncertainty shown as shaded areas is for simulated irradiance due to GHI, DHI, DNI, and albedo, while the measured irradiance has a measurement uncertainty of* ± 2.5 % ± 5 W/m^2.

The 11^{th} of October 2022

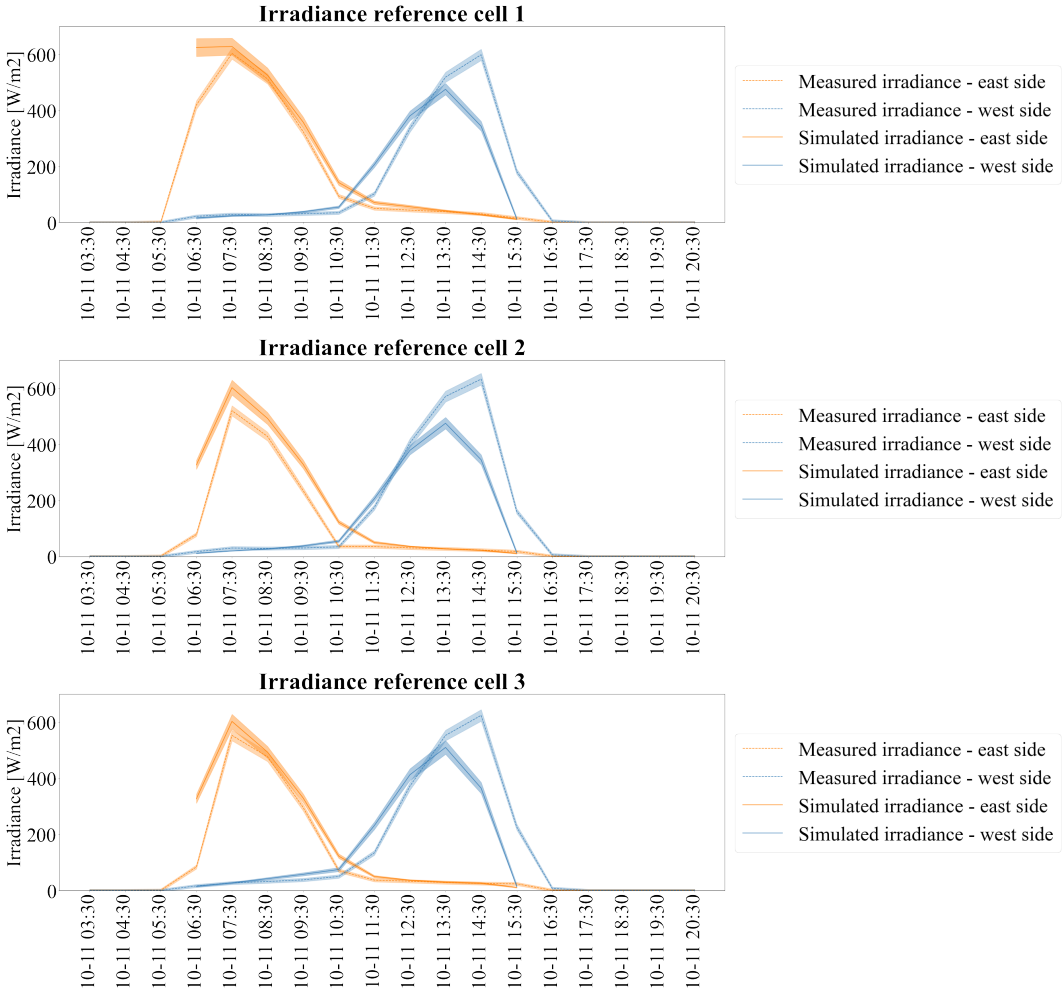

Figure 51: *Simulated and measured irradiance for the* 11^{th} *of October 2022. The measurement uncertainty shown as shaded areas is for simulated irradiance due to GHI, DHI, DNI, and albedo, while the measured irradiance has a measurement uncertainty of* ± 2.5 *%* ± 5 $\mathrm{W/m^2}$.

The 23^{rd} of December 2022

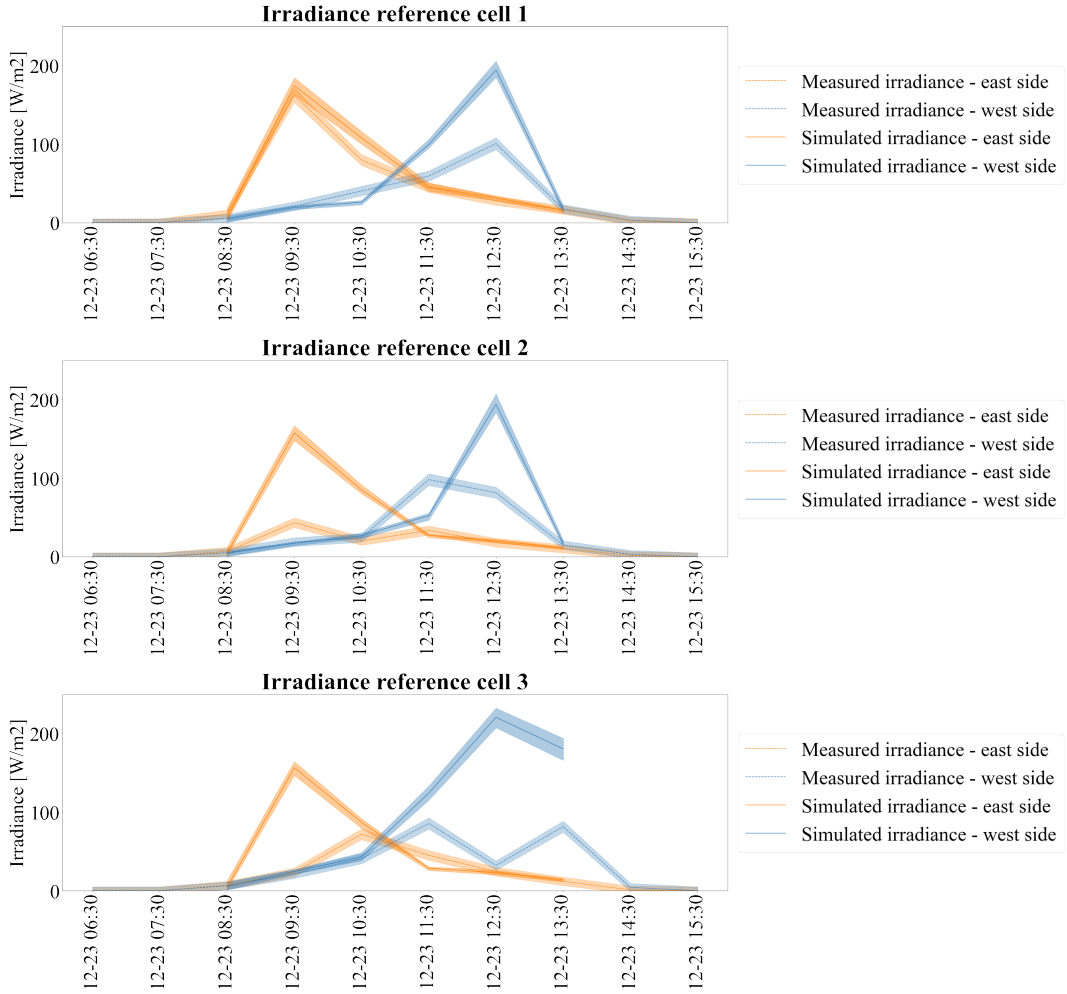

Figure 52: *Simulated and measured irradiance for the* 23^{rd} *of December 2022. The measurement uncertainty shown as shaded areas is for simulated irradiance due to GHI, DHI, DNI, and albedo, while the measured irradiance has a measurement uncertainty of* ± 2.5 *%* ± 5 $\mathrm{W/m^2}$.

The 23^{rd} of December 2022 - 5-minute interval

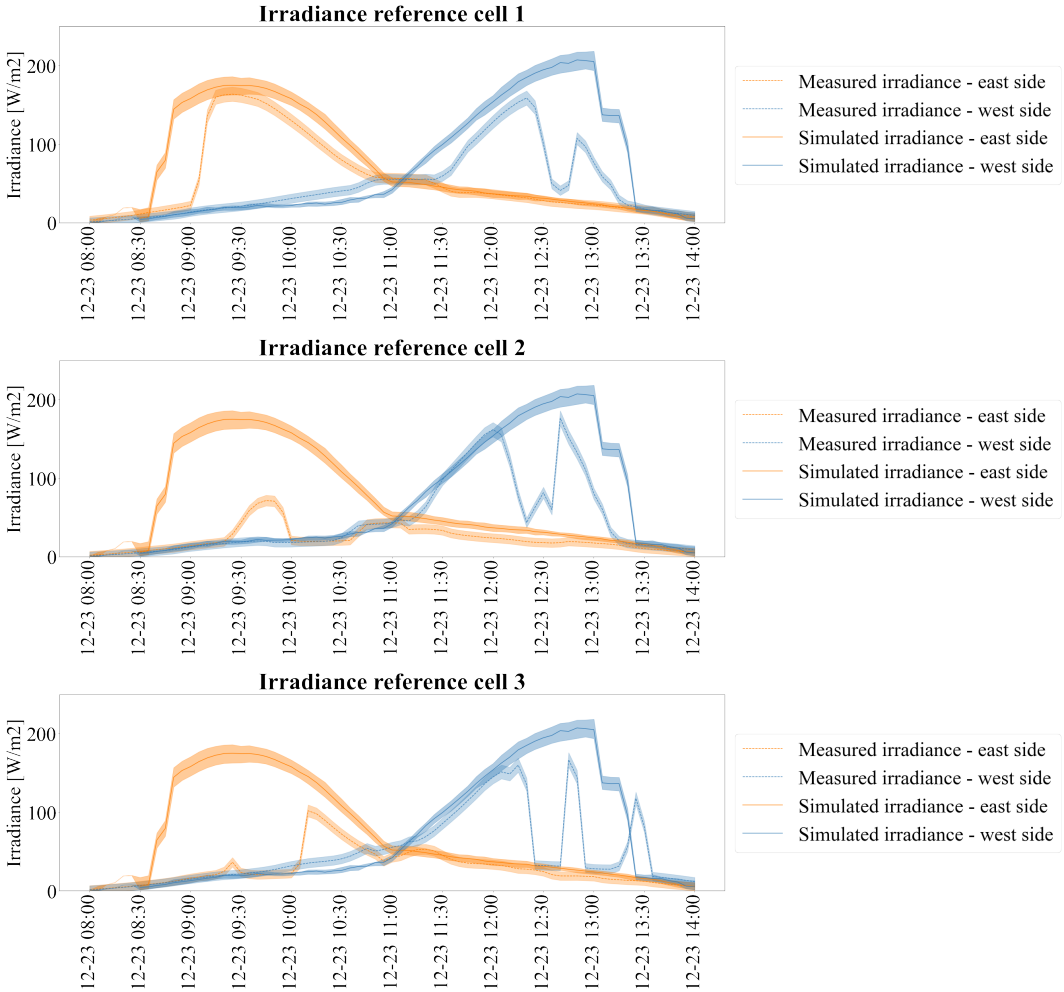

Figure 53: *Simulated and measured irradiance for the* 23^{rd} *of December 2022. The measurement uncertainty shown as shaded areas is for simulated irradiance due to GHI, DHI, DNI, and albedo, while the measured irradiance has a measurement uncertainty of* ± 2.5 *%* ± 5 $\mathrm{W/m^2}$.

The 1^{st} of March 2023

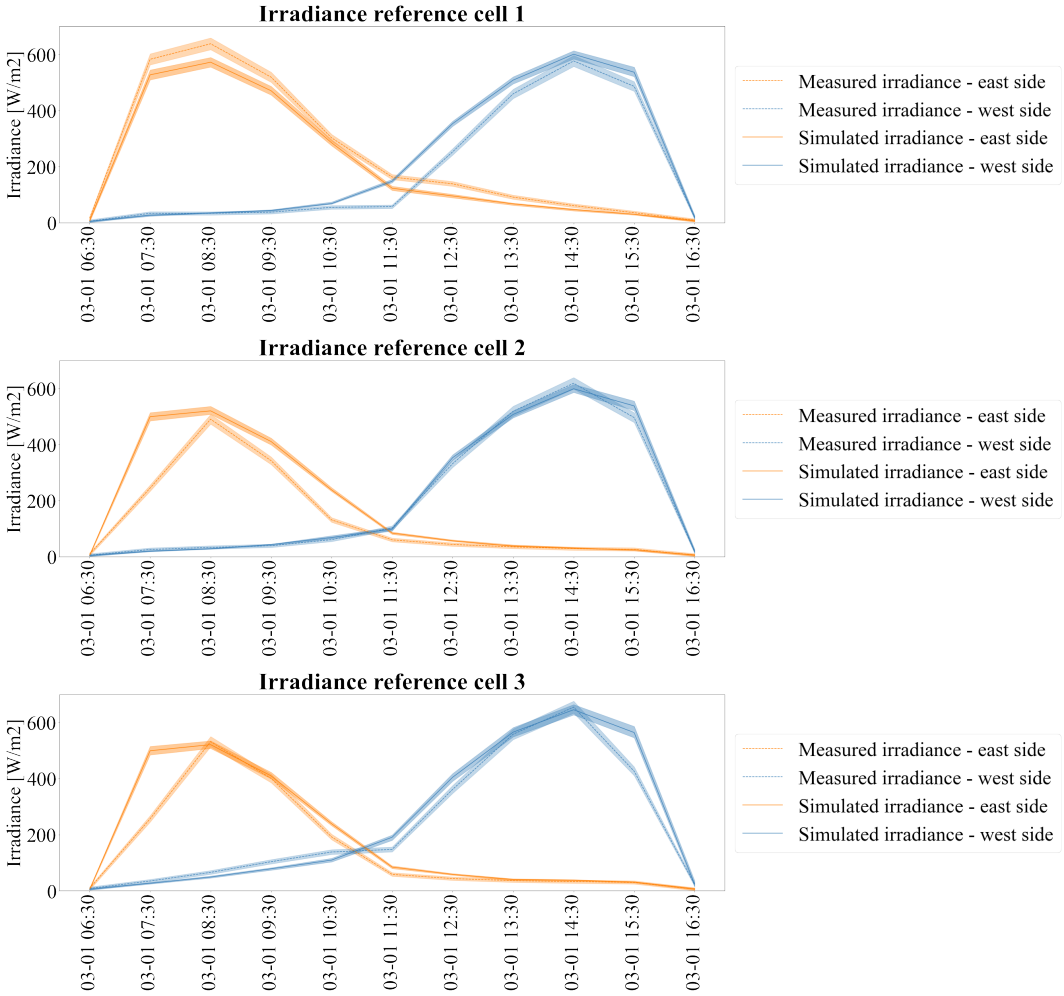

Figure 54: *Simulated and measured irradiance for the* 1^{st} *of March 2023. The measurement uncertainty shown as shaded areas is for simulated irradiance due to GHI, DHI, DNI, and albedo, while the measured irradiance has a measurement uncertainty of* ± 2.5 *%* ± 5 W/m^2.

E.2 Overcast days

The 22^{nd} of July 2022

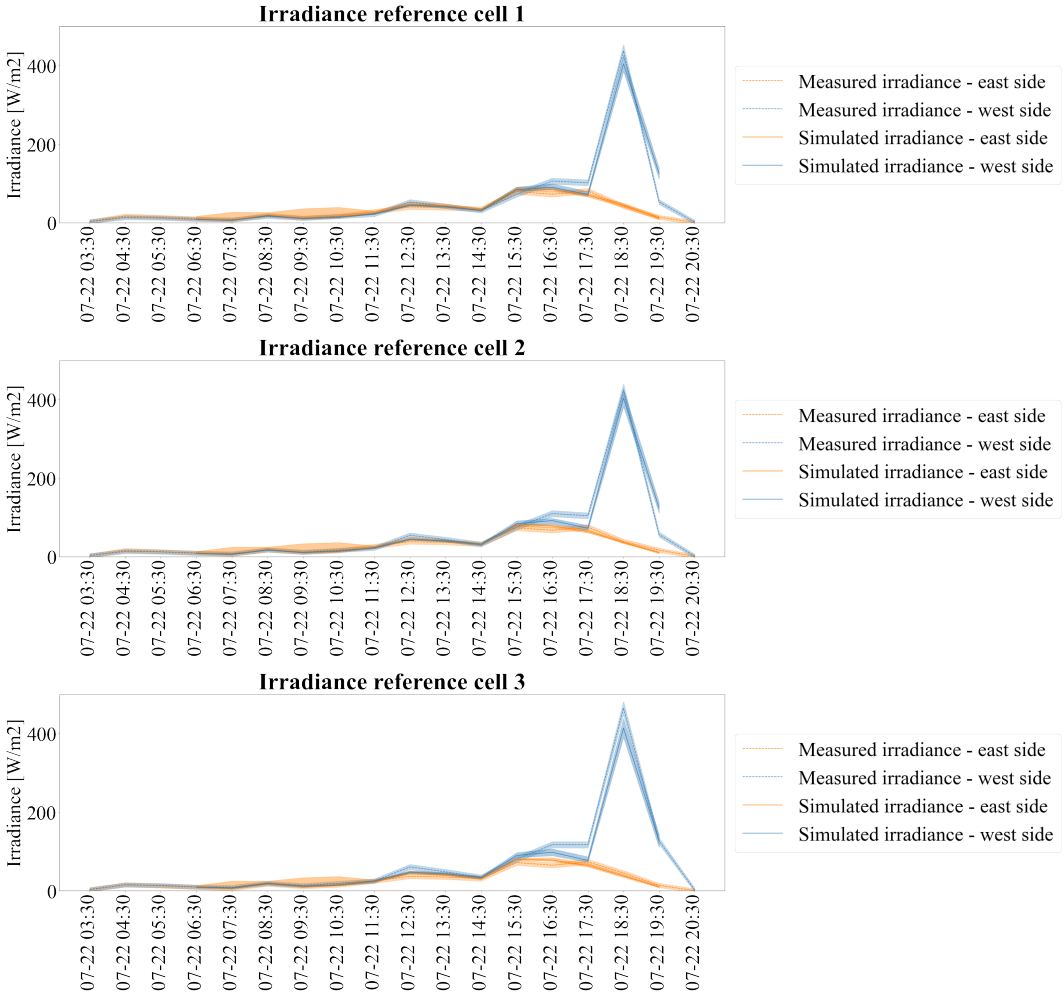

Figure 55: *Simulated and measured irradiance for the 22^{nd} of July 2022. The measurement uncertainty shown as shaded areas is for simulated irradiance due to GHI, DHI, DNI, and albedo, while the measured irradiance has a measurement uncertainty of* ± 2.5 *%* ± 5 $\mathrm{W/m^2}$.

The 17^{th} of October 2022

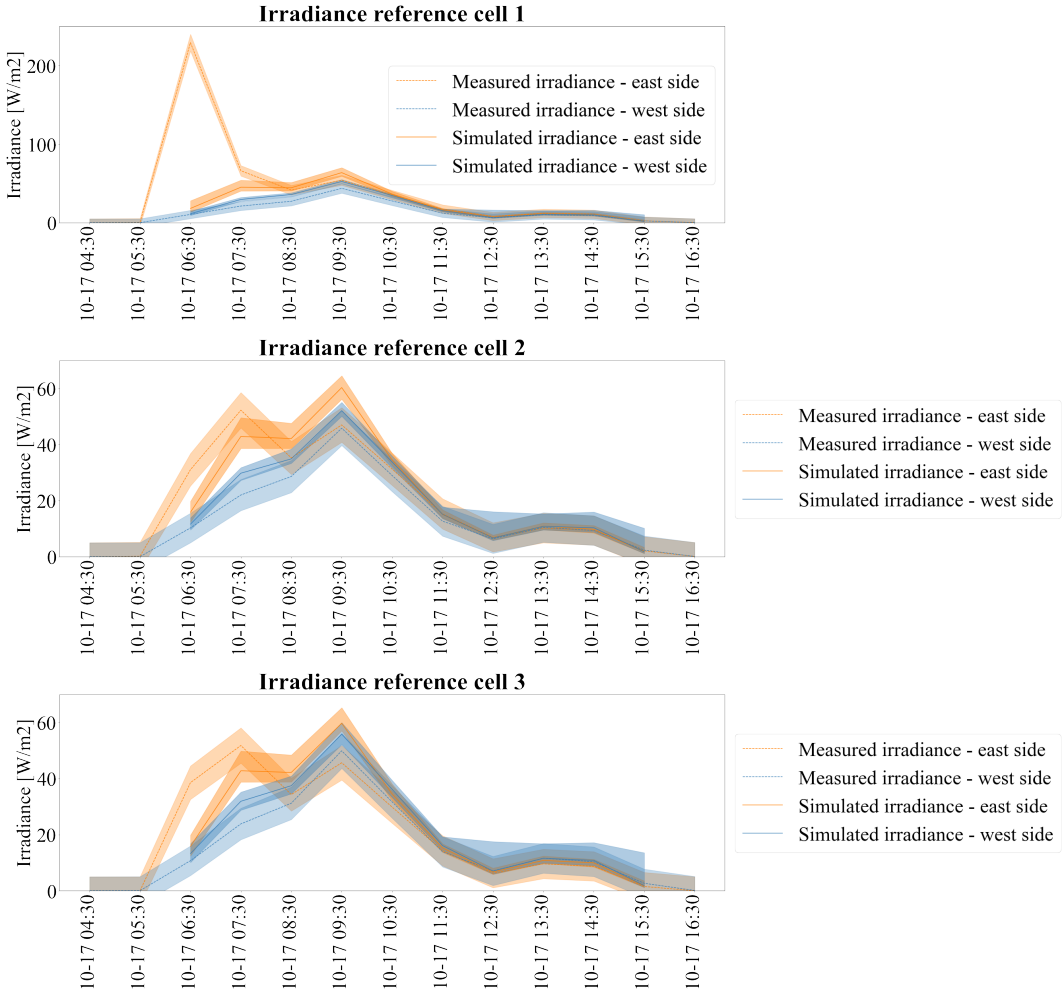

Figure 56: *Simulated and measured irradiance for the* 17^{th} *of October 2022. The measurement uncertainty shown as shaded areas is for simulated irradiance due to GHI, DHI, DNI, and albedo, while the measured irradiance has a measurement uncertainty of* ± 2.5 *%* ± 5 $\mathrm{W/m^2}$.

The 26^{st} of December 2022

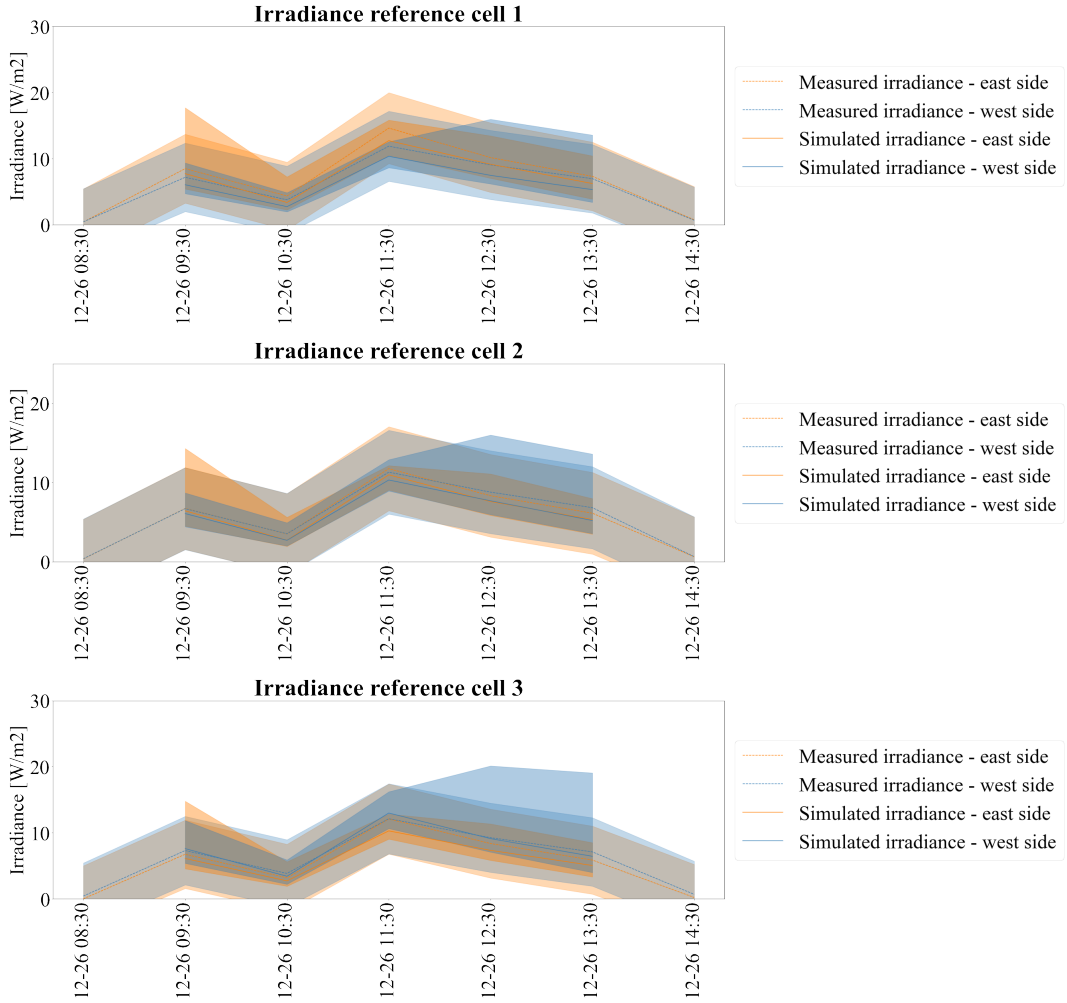

Figure 57: *Simulated and measured irradiance for the* 26^{st} *of December 2022. The measurement uncertainty shown as shaded areas is for simulated irradiance due to GHI, DHI, DNI, and albedo, while the measured irradiance has a measurement uncertainty of* ± 2.5 % ± 5 W/m^2.

The 22^{nd} of February 2023

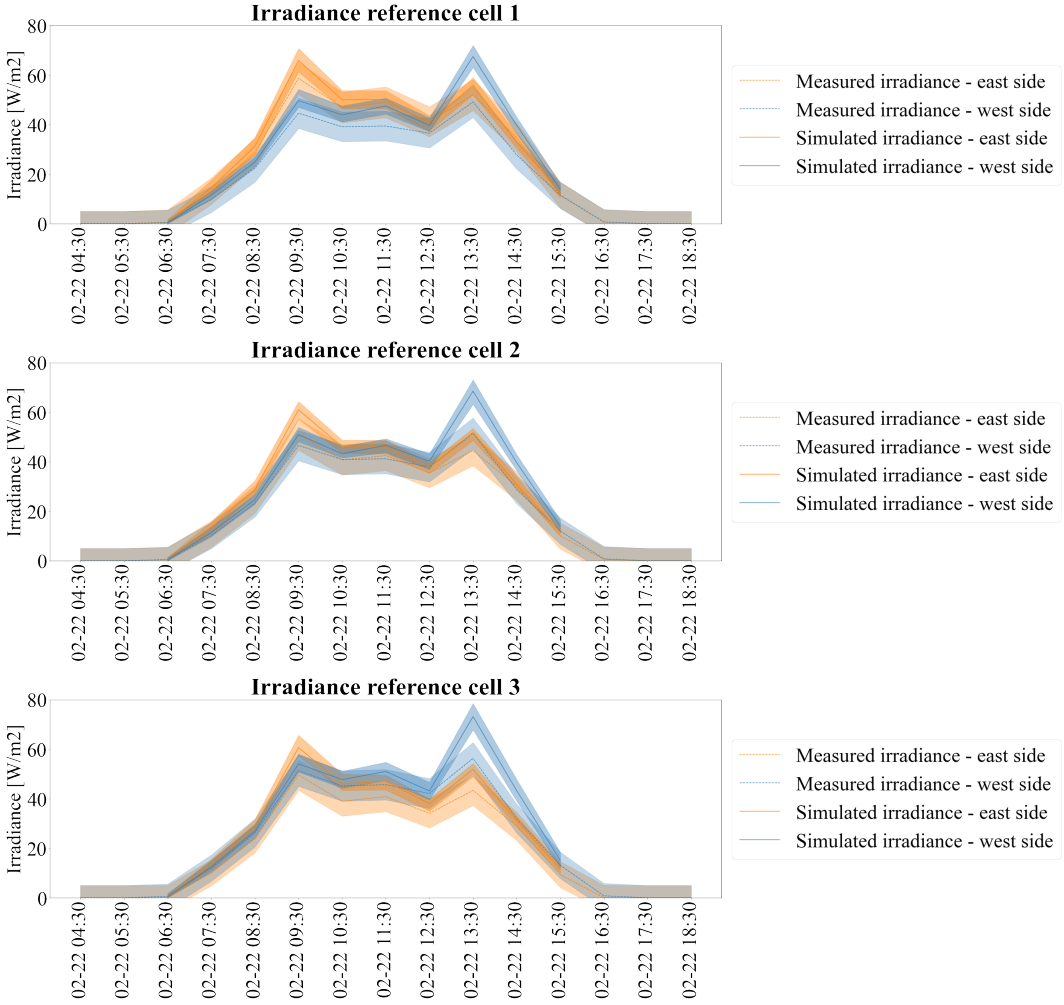

Figure 58: *Simulated and measured irradiance for the 22^{nd} of February 2023. The measurement uncertainty shown as shaded areas is for simulated irradiance due to GHI, DHI, DNI, and albedo, while the measured irradiance has a measurement uncertainty of* ± 2.5 % ± 5 W/m^2.

E.3 Days with varying weather

The 21^{st} of July 2022

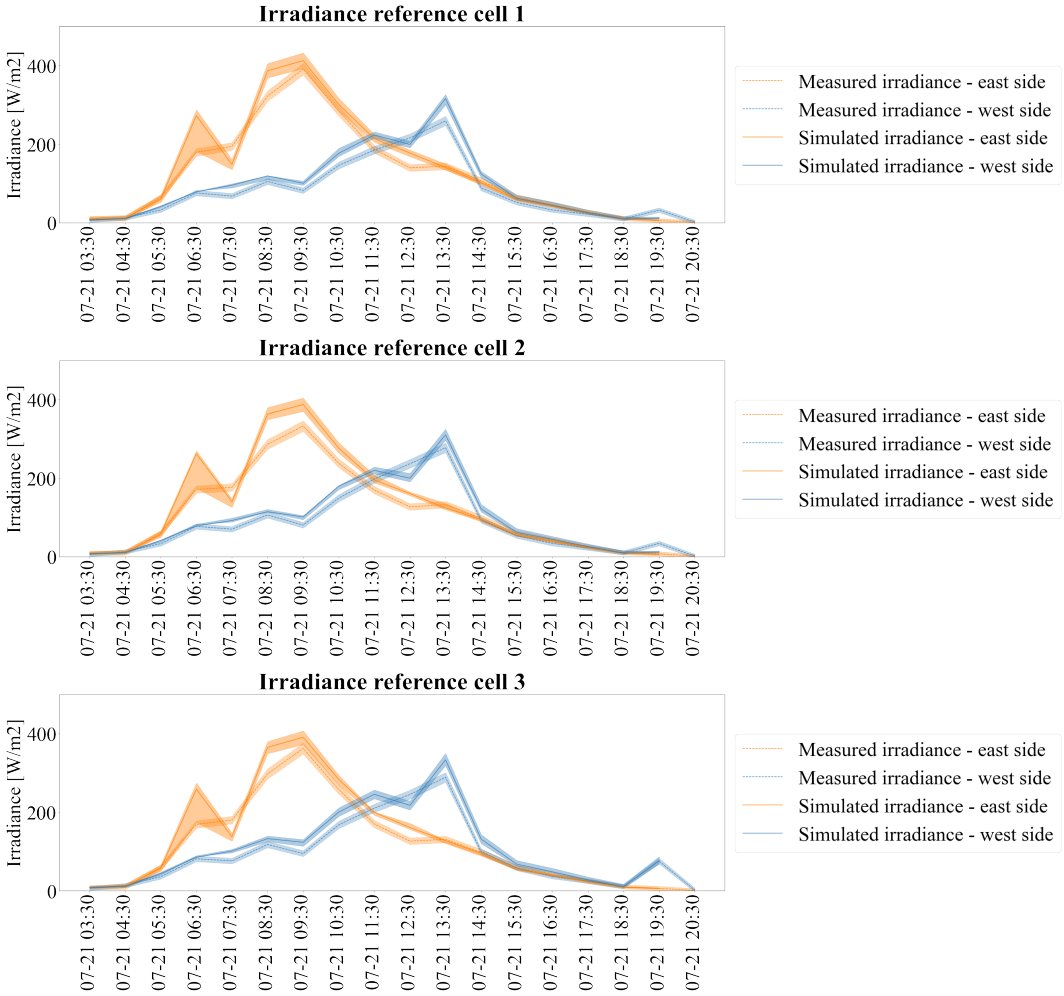

Figure 59: *Simulated and measured irradiance for the* 21^{st} *of July 2022. The measurement uncertainty shown as shaded areas is for simulated irradiance due to GHI, DHI, DNI, and albedo, while the measured irradiance has a measurement uncertainty of* ± 2.5 *%* ± 5 $\mathrm{W/m^2}$.

The 7^{rd} of October 2022

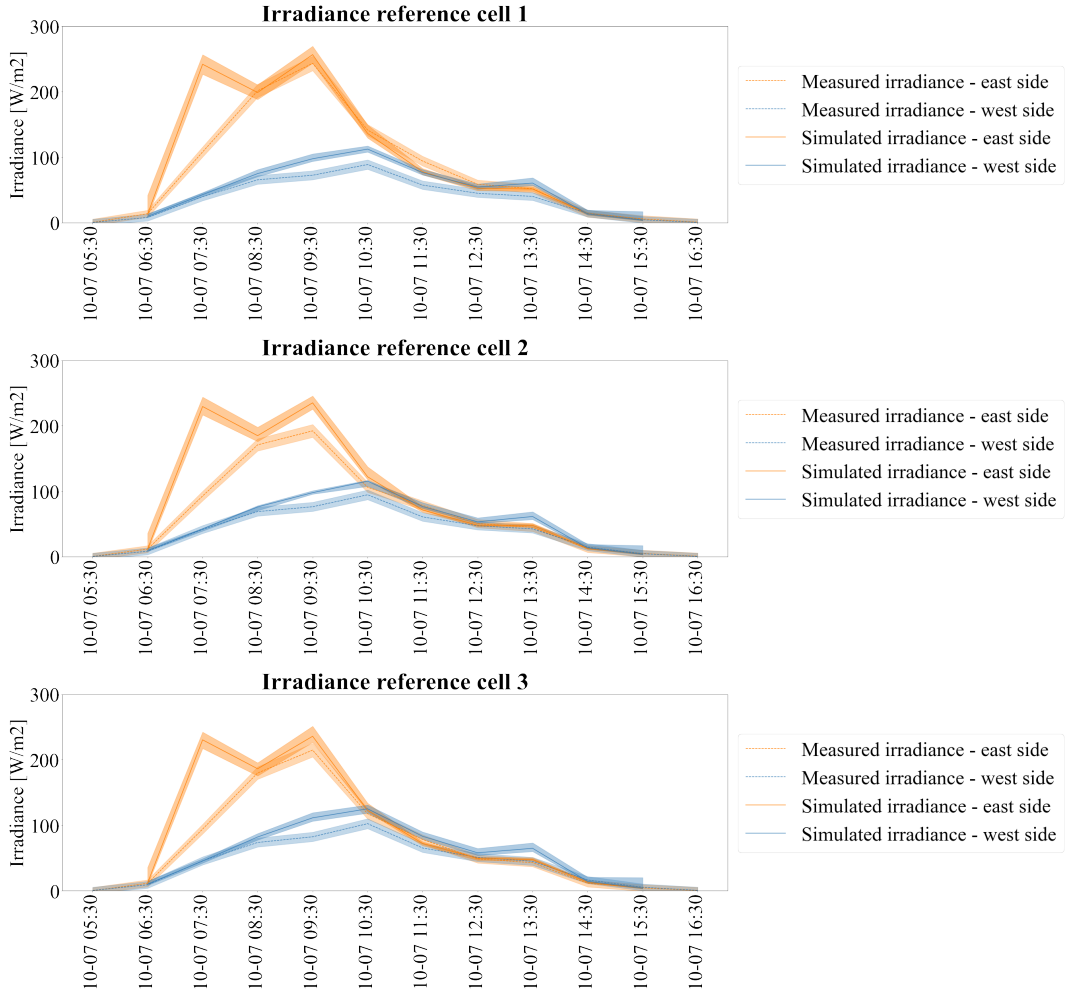

Figure 60: *Simulated and measured irradiance for the 7^{rd} of October 2022. The measurement uncertainty shown as shaded areas is for simulated irradiance due to GHI, DHI, DNI, and albedo, while the measured irradiance has a measurement uncertainty of* ± 2.5 % ± 5 W/m^2.

The 24^{th} of December 2022

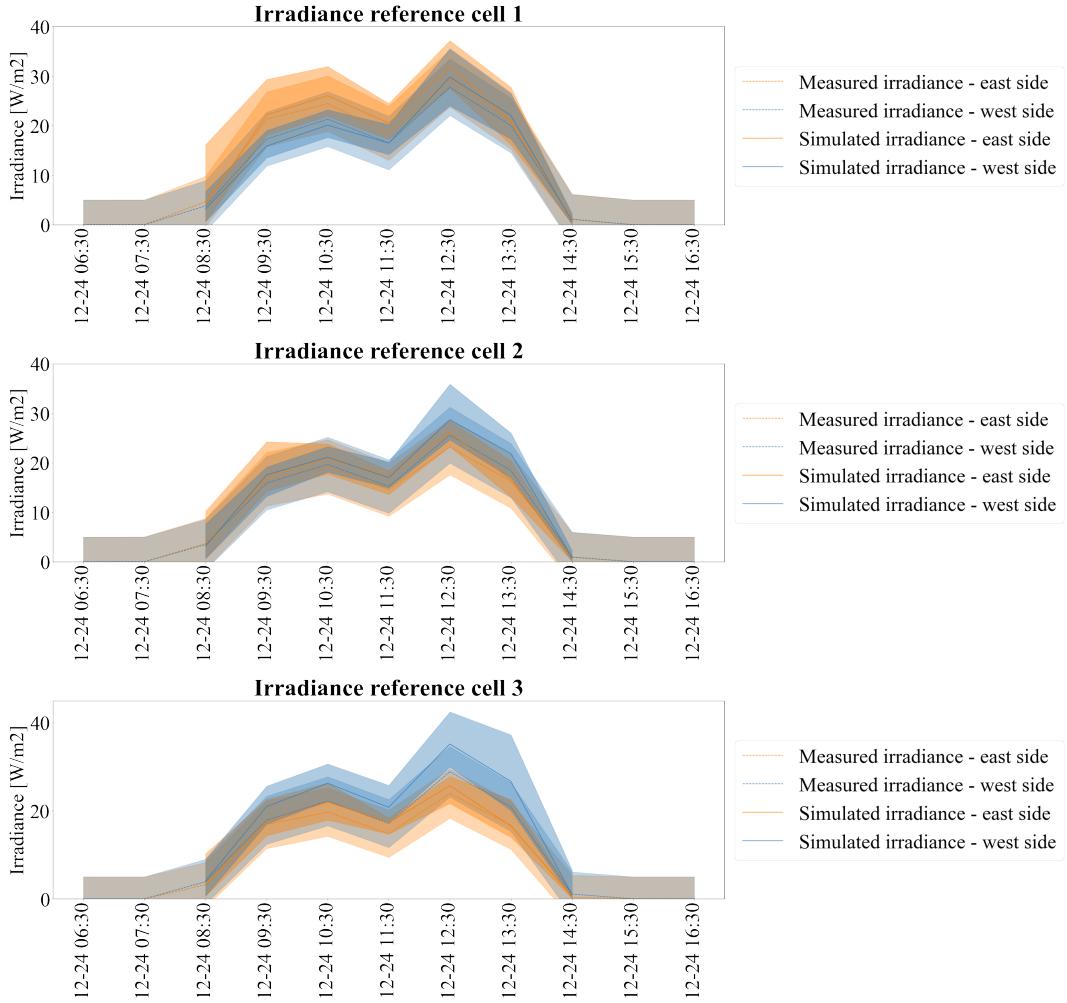

Figure 61: *Simulated and measured irradiance for the 24^{th} of December 2022. The measurement uncertainty shown as shaded areas is for simulated irradiance due to GHI, DHI, DNI, and albedo, while the measured irradiance has a measurement uncertainty of* ± 2.5 % ± 5 W/m^2.

The 26^{st} of February 2023

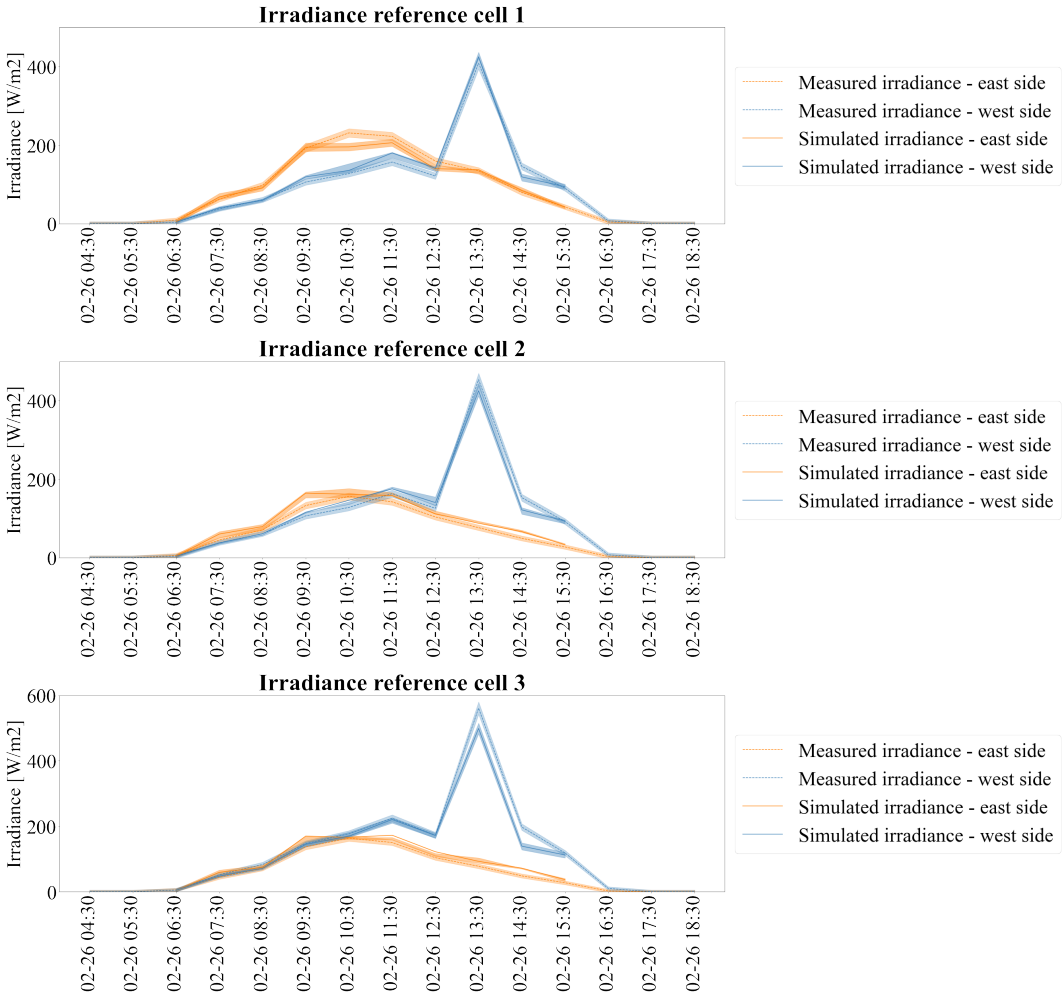

Figure 62: *Simulated and measured irradiance for the 26^{st} of February 2023. The measurement uncertainty shown as shaded areas is for simulated irradiance due to GHI, DHI, DNI, and albedo, while the measured irradiance has a measurement uncertainty of* ± 2.5 % ± 5 W/m^2.

E.4 Cumulative sky, irradiance for a longer period of time

Note that the simulation for the three reference cells is done for the periods listed in Section 3.5

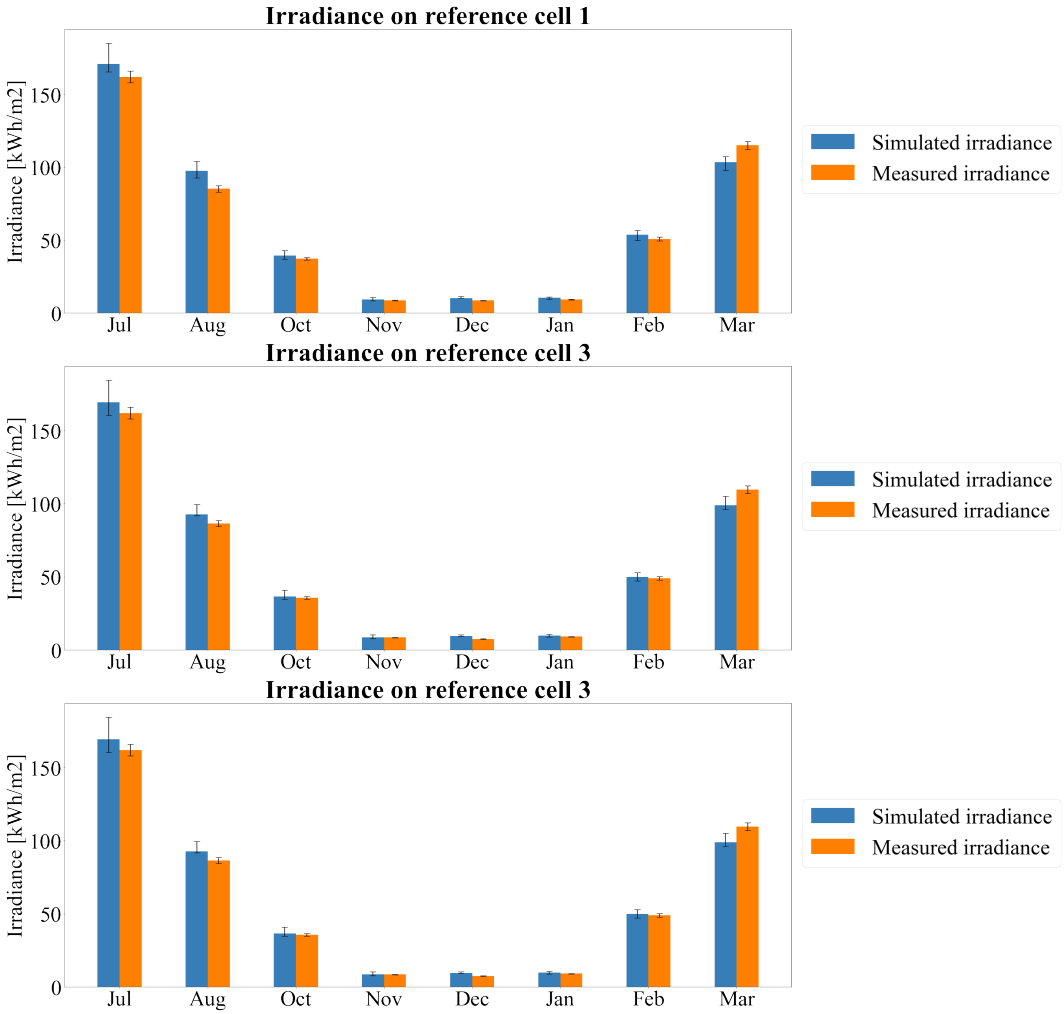

Figure 63: *Simulated irradiance using a cumulative sky compared with measured irradiance for the same time period. The shaded uncertainty for the simulated irradiance is due to the measurement uncertainty in GHI, DHI, DNI, and albedo, while the measured irradiance has a measurement uncertainty of* ± 2.5 *%* ± 5 $\mathrm{W/m^2}$.

F Orientation of the test site

12^{th} of August 2022

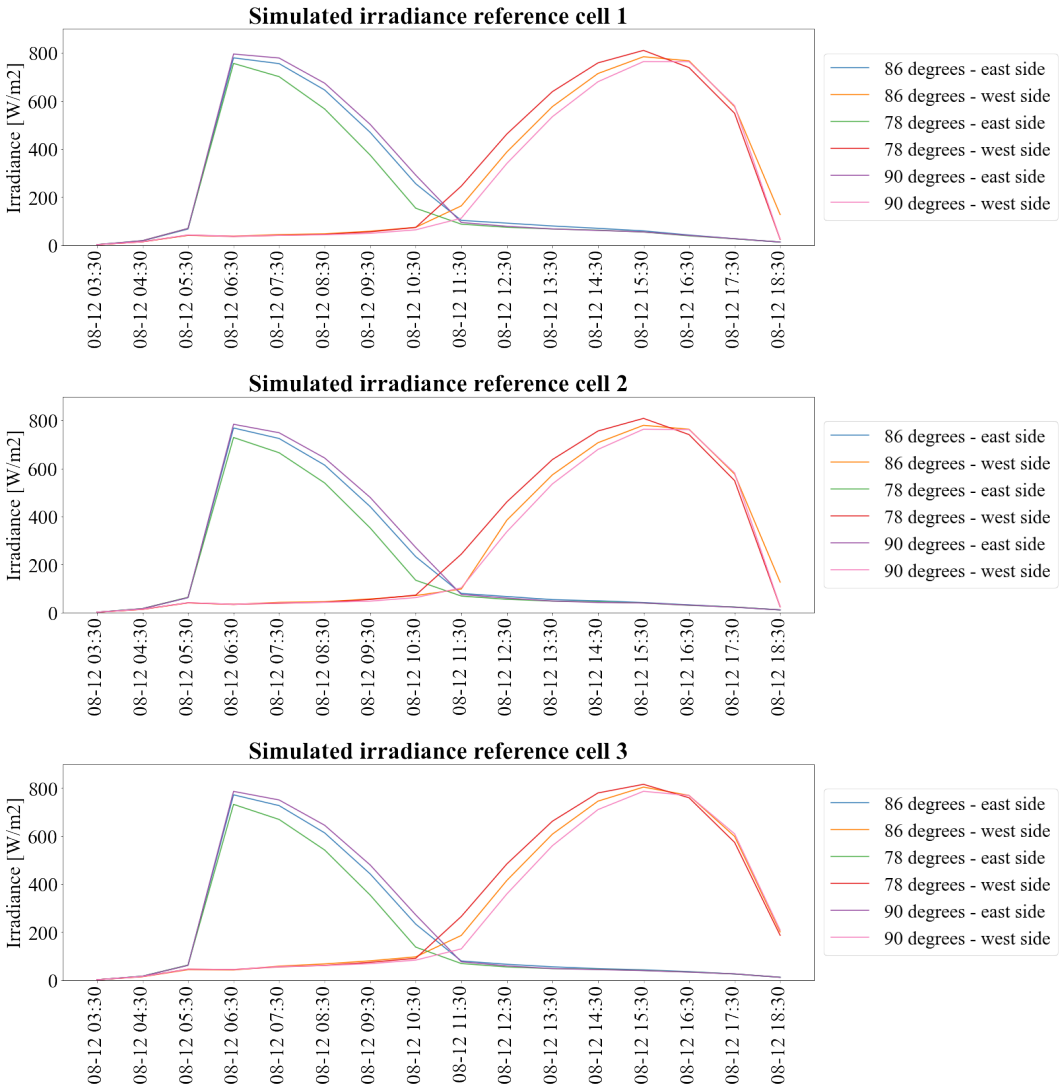

Figure 64: *Simulated irradiance the 12^{th} of August 2022 for the orientations 78°, 86° and 90° from the north compared to measured irradiance.*

26^{th} of January 2023

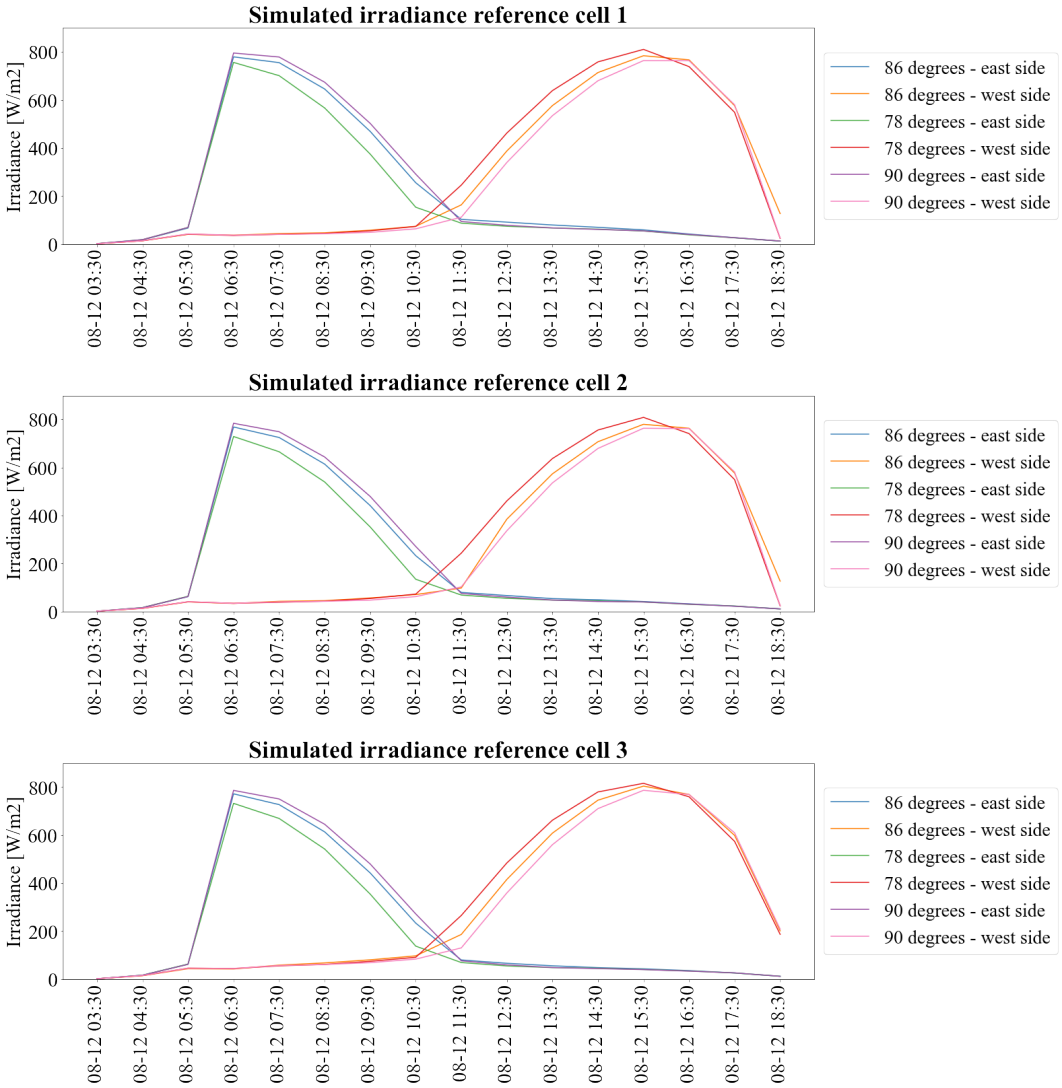

Figure 65: *Simulated irradiance the* 26^{th} *of January 2023 for the orientations 78°, 86° and 90° from the north compared to measured irradiance.*

G Measurement uncertainty due to albedo for simulated irradiance

The 12^{th} of August 2022

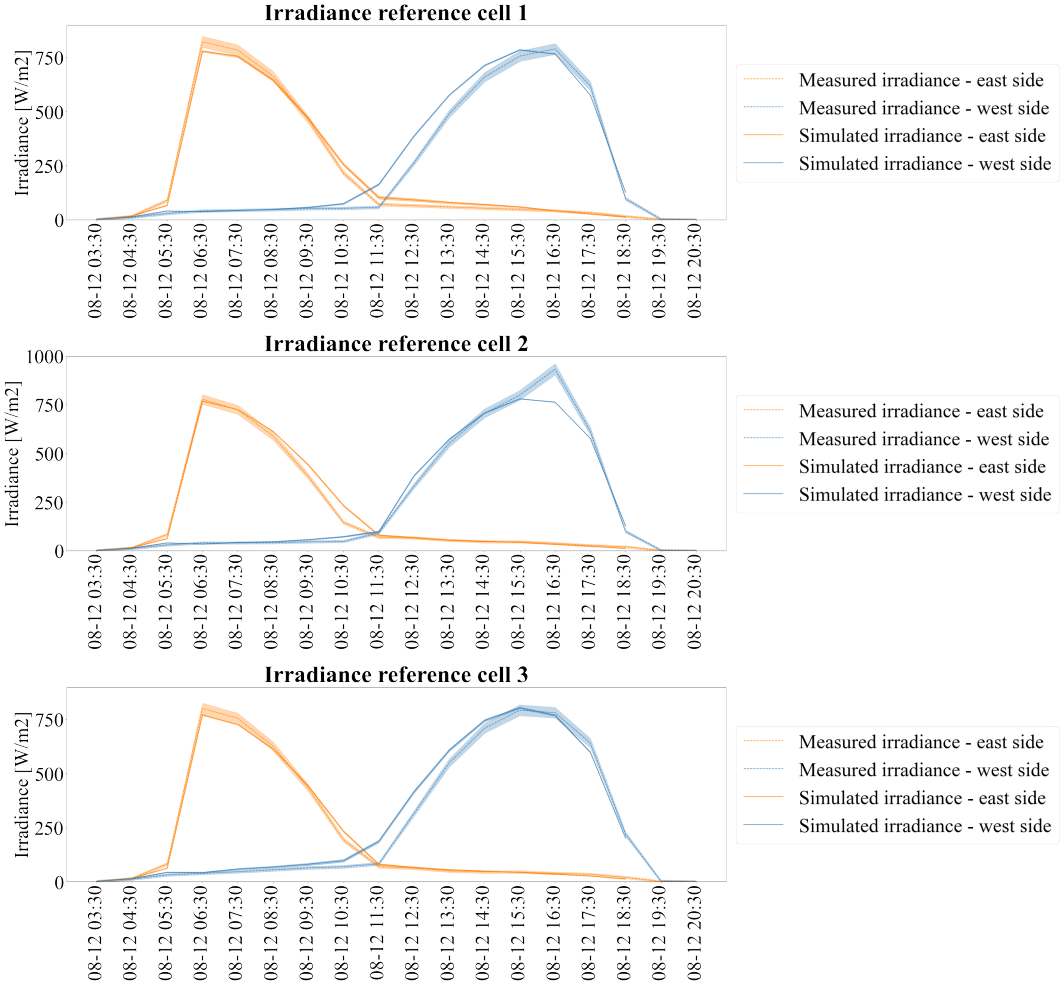

Figure 66: *Simulated and measured irradiance for the* 12^{th} *of August 2022. The shaded uncertainty for the simulated irradiance is due to the measurement uncertainty in albedo, while the measured irradiance has a measurement uncertainty of* ± 2.5 *%* ± 5 $\mathrm{W/m^2}$.

The 23^{rd} of December 2022

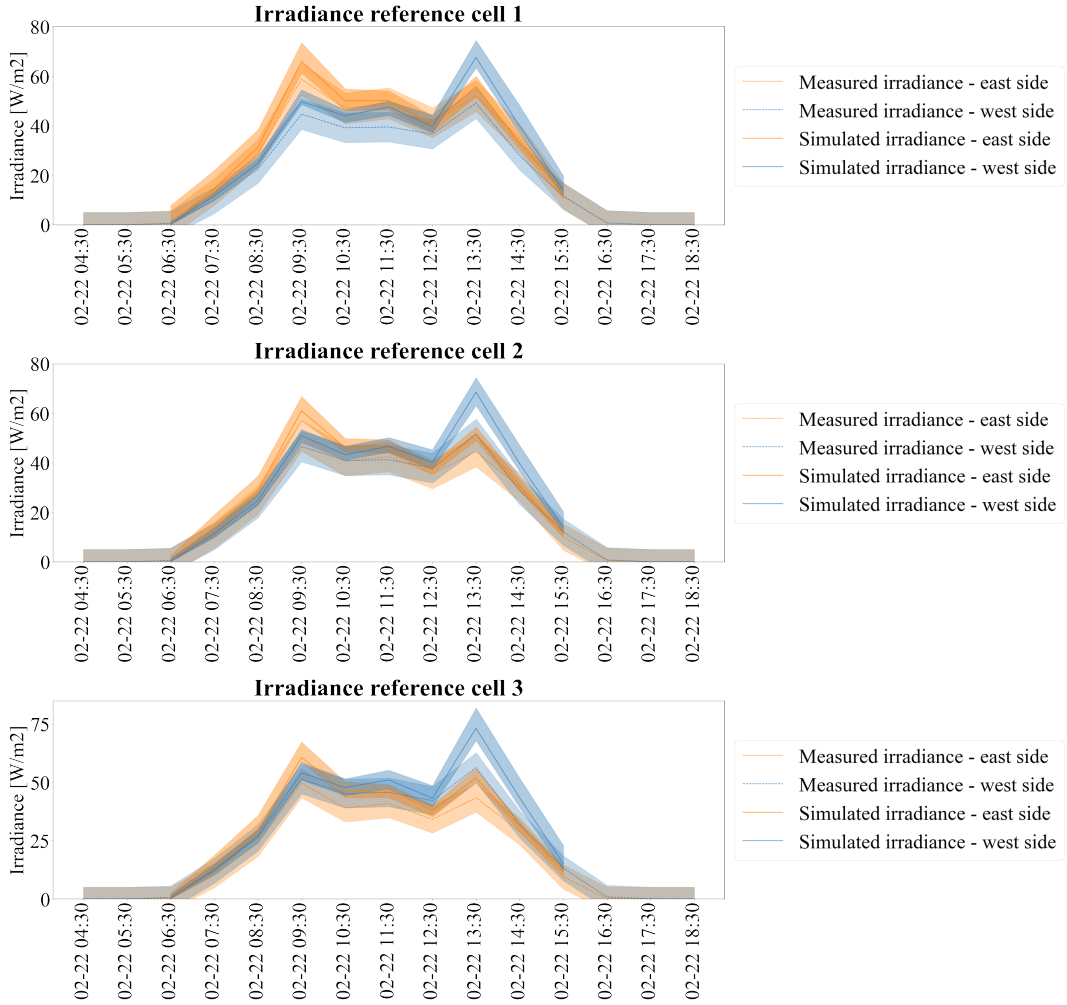

Figure 67: *Simulated and measured irradiance for the* 23^{rd} *of December 2022. The shaded uncertainty for the simulated irradiance is due to the measurement uncertainty in albedo, while the measured irradiance has a measurement uncertainty of* ± 2.5 *%* ± 5 $\mathrm{W/m^2}$.

The 22^{nd} of February 2023

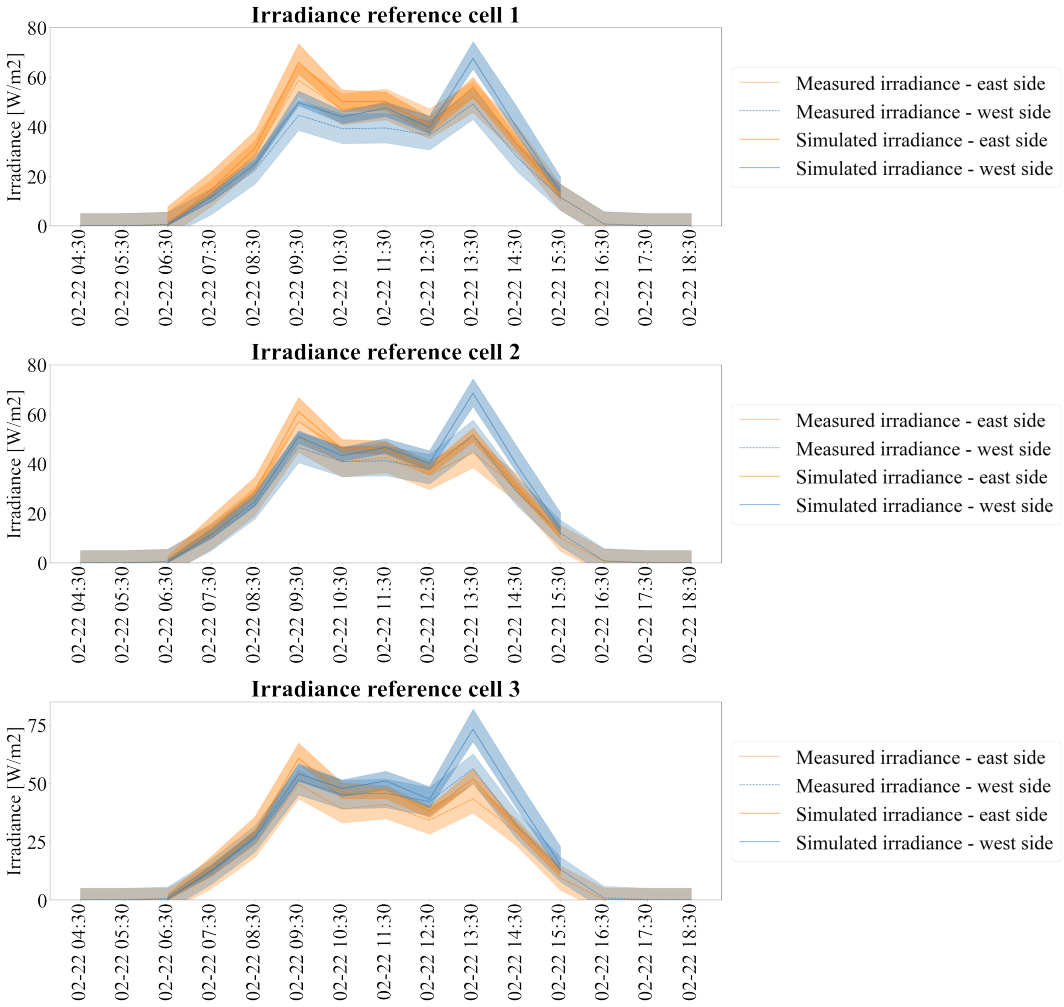

Figure 68: *Simulated and measured irradiance for the* 22^{nd} *of February 2023. The shaded uncertainty for the simulated irradiance is due to the measurement uncertainty in albedo, while the measured irradiance has a measurement uncertainty of* ± 2.5 *%* ± 5 $\mathrm{W/m^2}$.

H Simulated power for selected days

H.1 Clear-sky days

The 12^{th} of August 2022

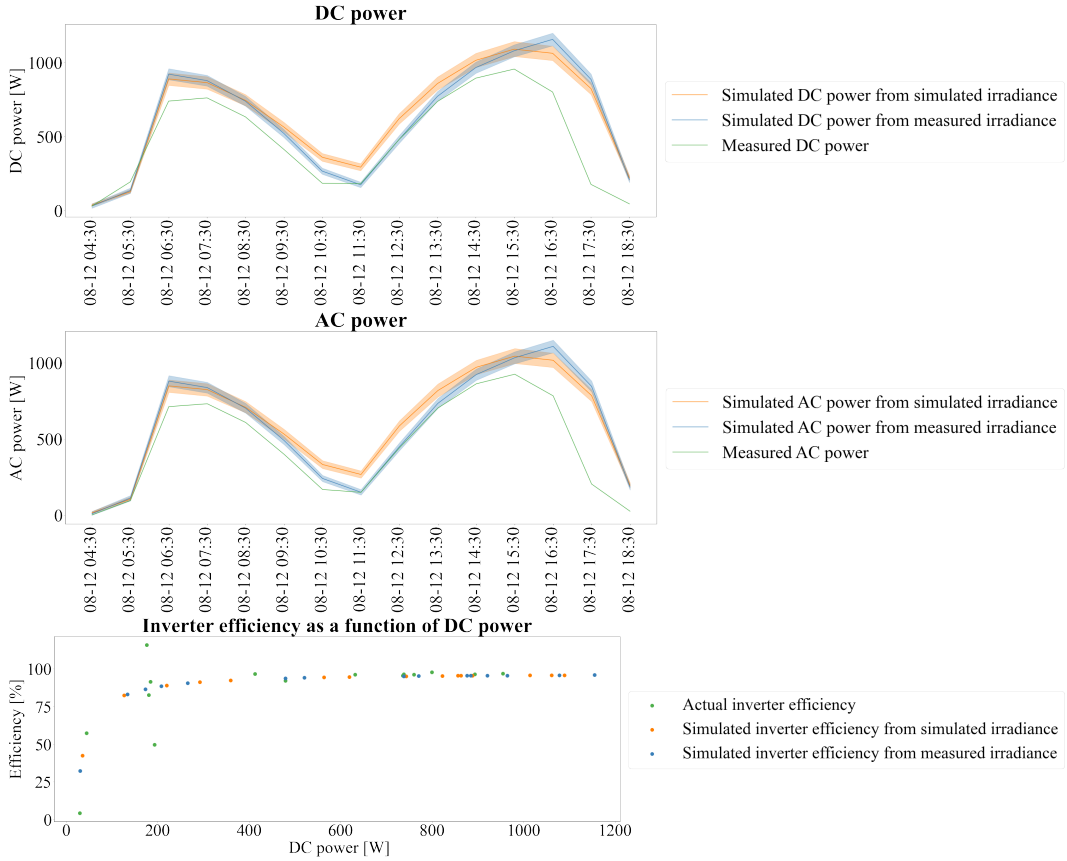

Figure 69: *Simulated DC and AC power using simulated and measured irradiance as input compared to measured DC and AC power. Thereafter displaying the inverter efficiency as a function of DC power for the* 12^{th} *of August 2022. The shaded area for the simulated results is due to the measurement uncertainty in GHI, DHI, DNI, and albedo. The measurement uncertainty for measured results has been neglected.*

The 11^{th} of October 2022

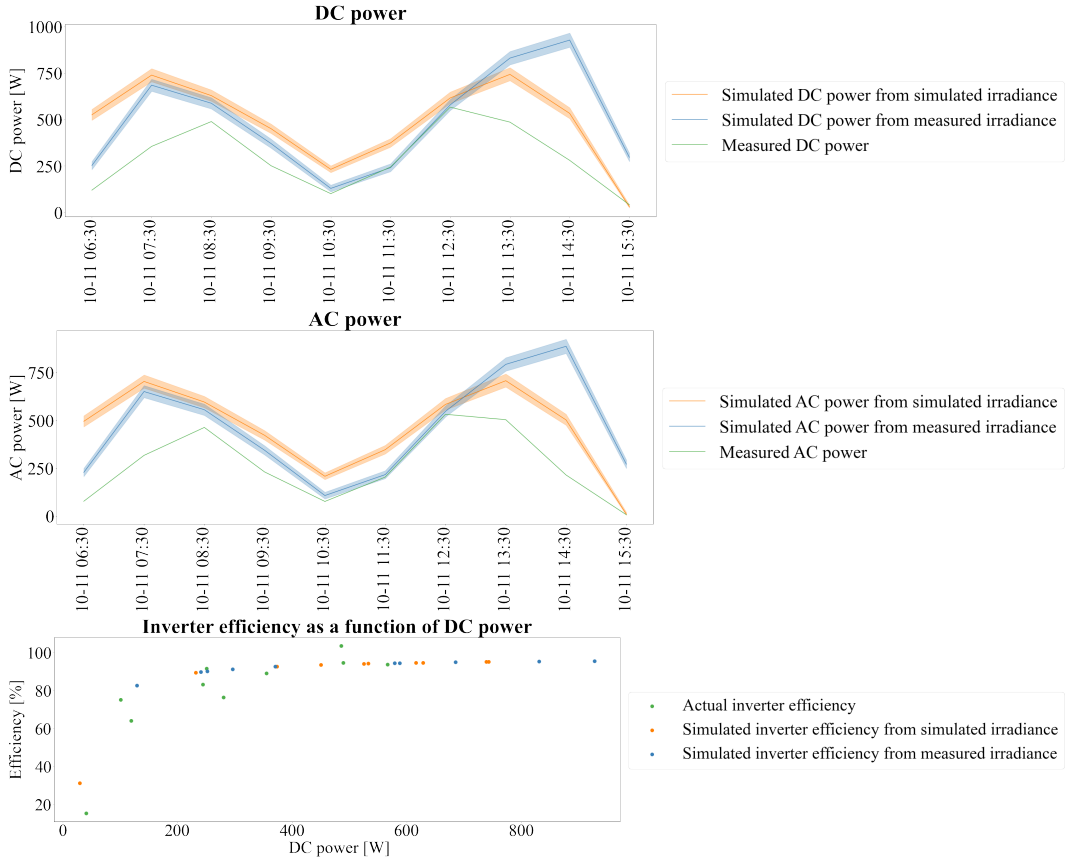

Figure 70: *Simulated DC and AC power using simulated and measured irradiance as input compared to measured DC and AC power. Thereafter displaying the inverter efficiency as a function of DC power for the* 11^{th} *of October 2022. The shaded area for the simulated results is due to the measurement uncertainty in GHI, DHI, DNI, and albedo. The measurement uncertainty for measured results has been neglected.*

The 23^{rd} of December 2022

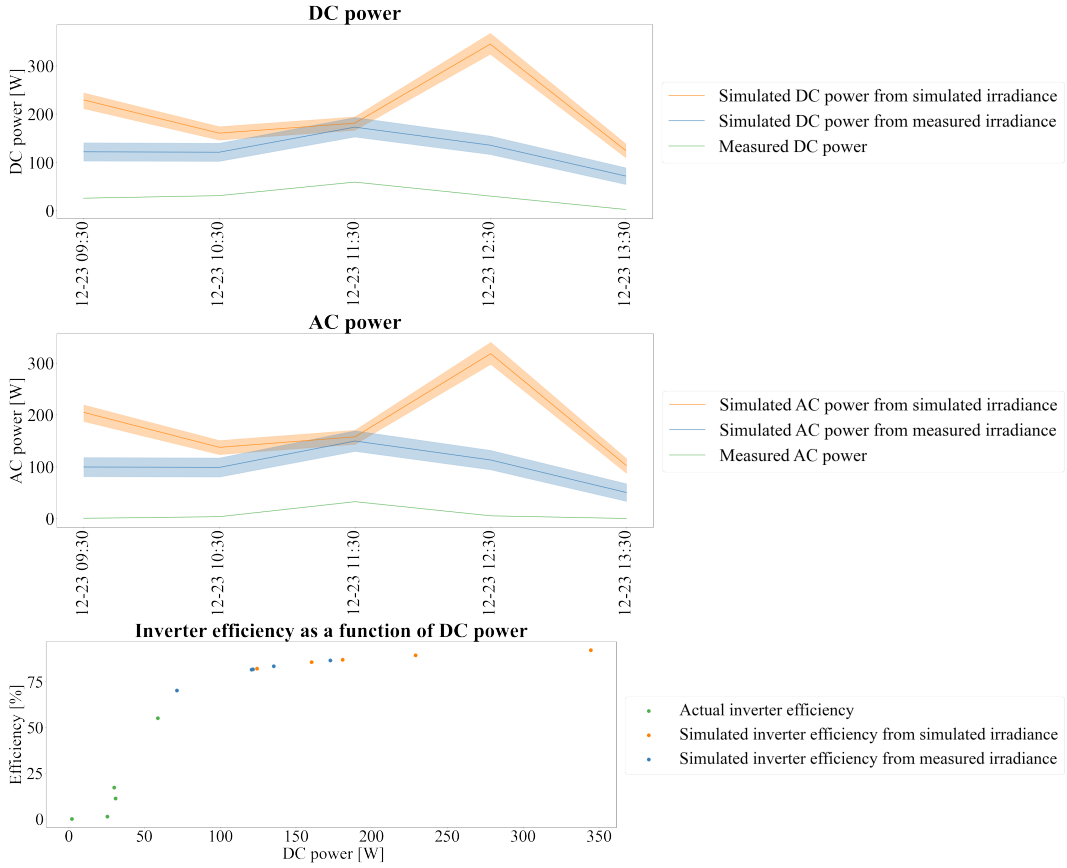

Figure 71: *Simulated DC and AC power using simulated and measured irradiance as input compared to measured DC and AC power. Thereafter displaying the inverter efficiency as a function of DC power for the* 23^{rd} *of December 2022. The shaded area for the simulated results is due to the measurement uncertainty in GHI, DHI, DNI, and albedo. The measurement uncertainty for measured results has been neglected.*

The 1^{st} of March 2023

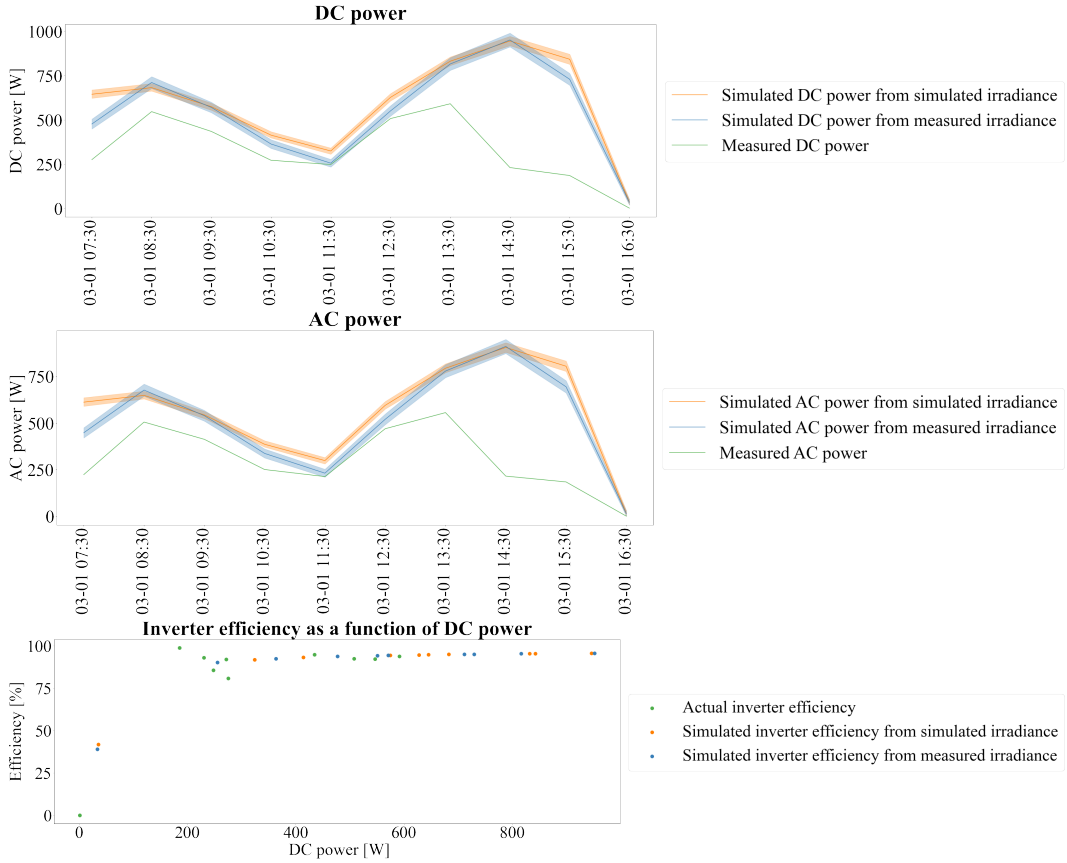

Figure 72: *Simulated DC and AC power using simulated and measured irradiance as input compared to measured DC and AC power. Thereafter displaying the inverter efficiency as a function of DC power for the* 1^{st} *of March 2023. The shaded area for the simulated results is due to the measurement uncertainty in GHI, DHI, DNI, and albedo. The measurement uncertainty for measured results has been neglected.*

H.2 Overcast days

The 22^{nd} of July 2022

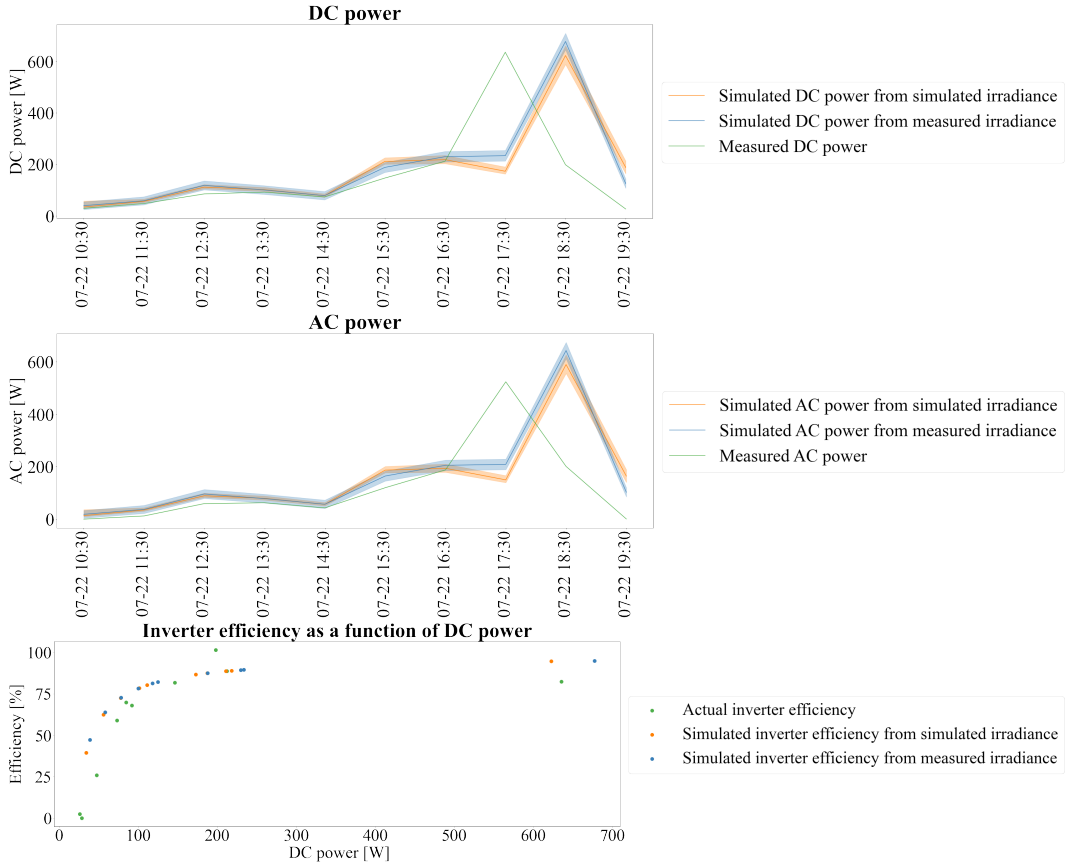

Figure 73: *Simulated DC and AC power using simulated and measured irradiance as input compared to measured DC and AC power. Thereafter displaying the inverter efficiency as a function of DC power for the 22^{nd} of July 2022. The shaded area for the simulated results is due to the measurement uncertainty in GHI, DHI, DNI, and albedo. The measurement uncertainty for measured results has been neglected.*

The 17^{th} of October 2022

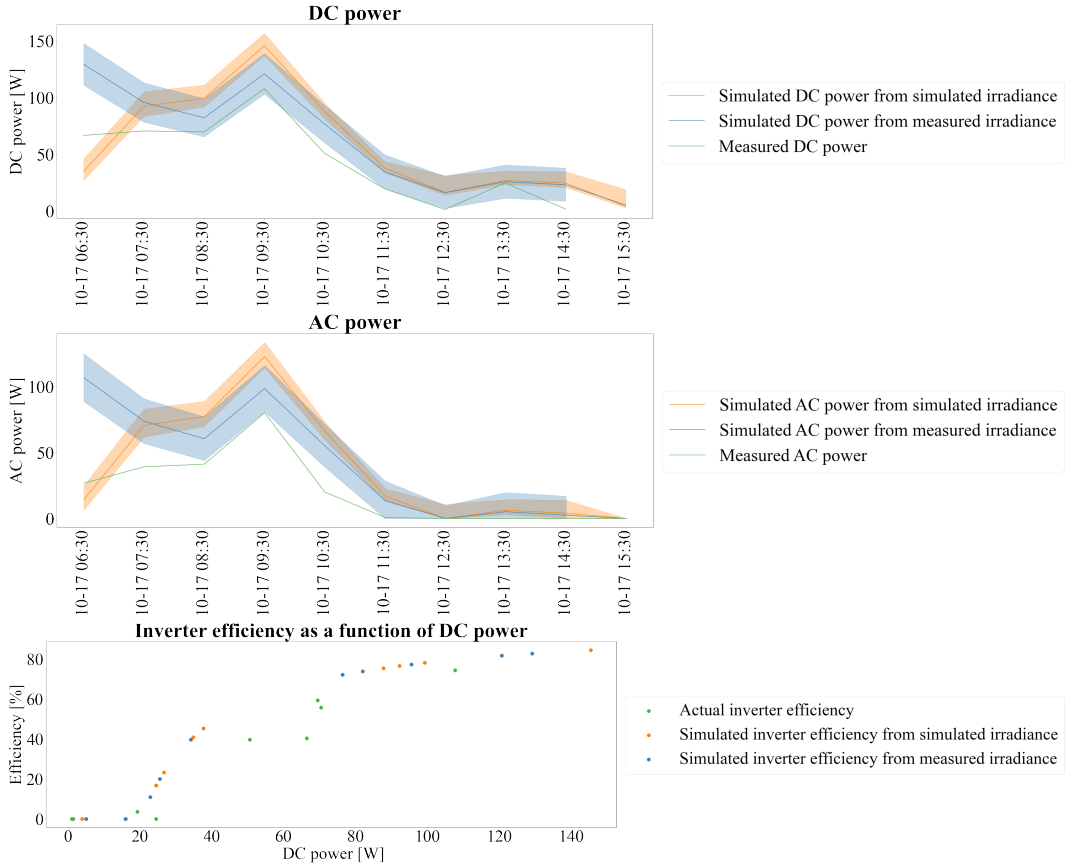

Figure 74: *Simulated DC and AC power using simulated and measured irradiance as input compared to measured DC and AC power. Thereafter displaying the inverter efficiency as a function of DC power for the* 17^{th} *of October 2022. The shaded area for the simulated results is due to the measurement uncertainty in GHI, DHI, DNI, and albedo. The measurement uncertainty for measured results has been neglected.*

The 26^{st} of December 2022

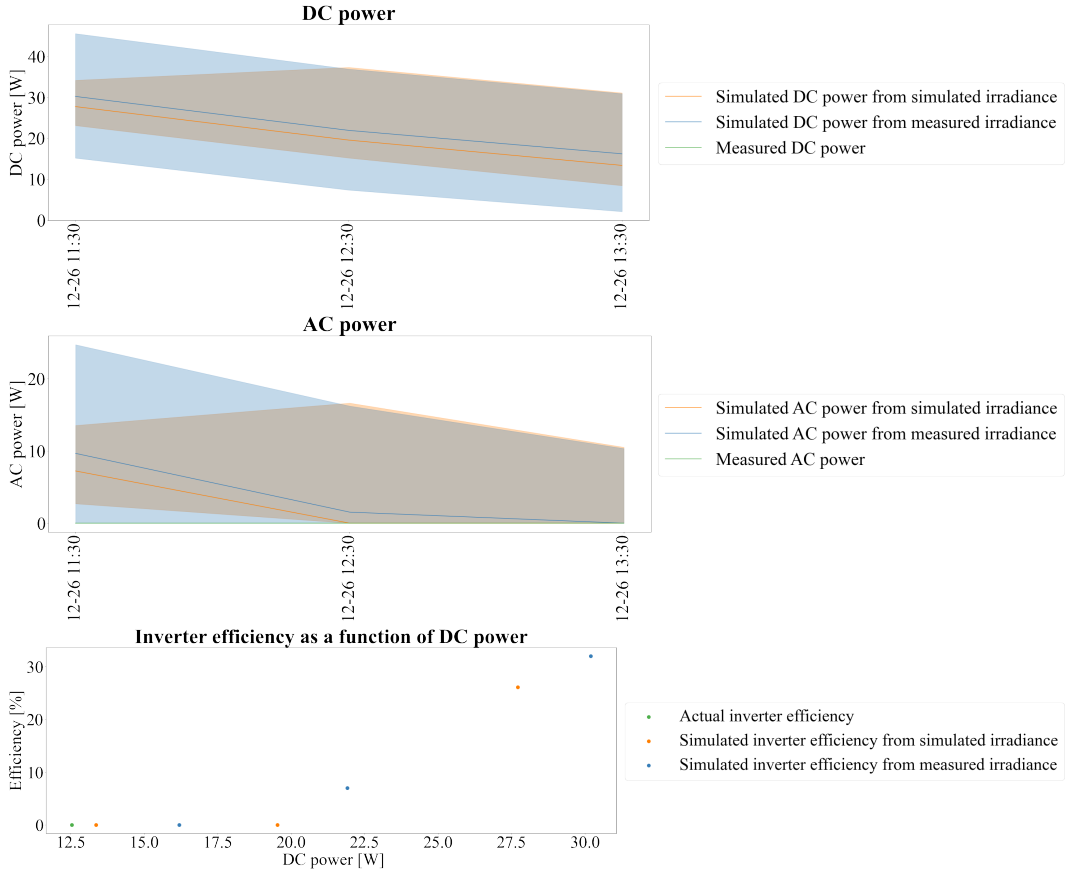

Figure 75: *Simulated DC and AC power using simulated and measured irradiance as input compared to measured DC and AC power. Thereafter displaying the inverter efficiency as a function of DC power for the* 26^{st} *of December 2022. The shaded area for the simulated results is due to the measurement uncertainty in GHI, DHI, DNI, and albedo. The measurement uncertainty for measured results has been neglected.*

The 22^{nd} of February 2023

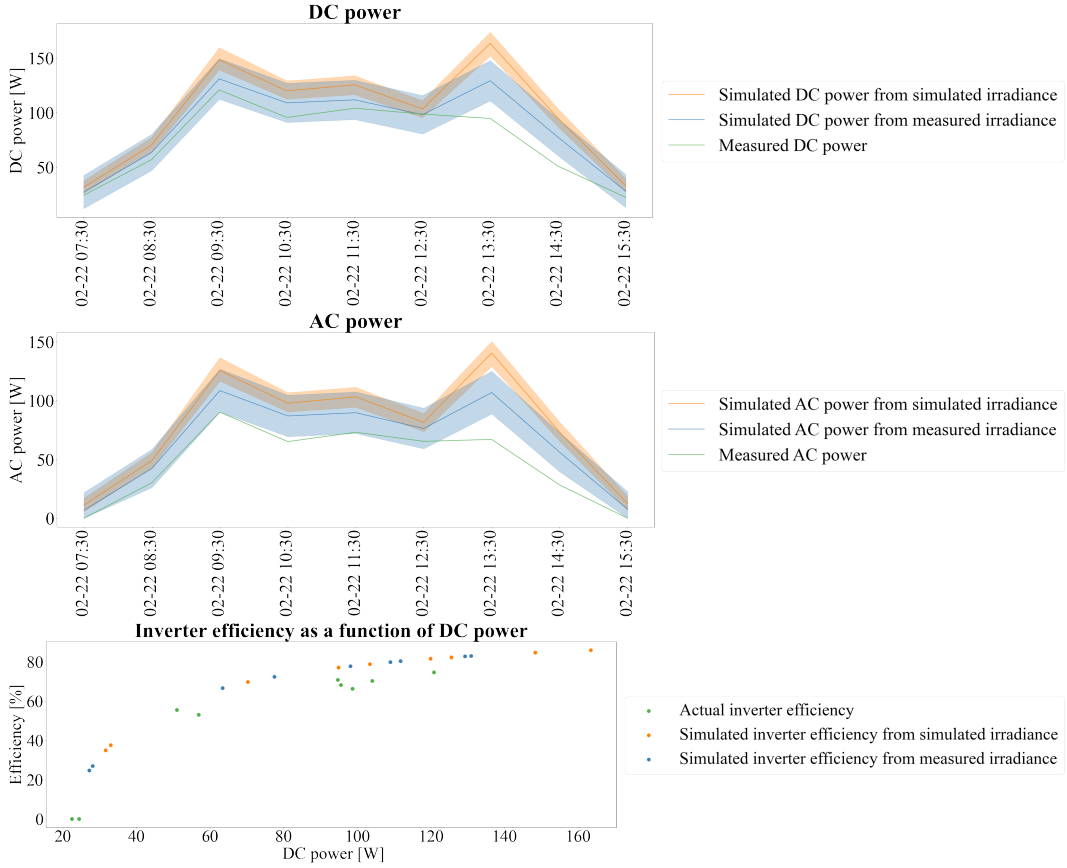

Figure 76: *Simulated DC and AC power using simulated and measured irradiance as input compared to measured DC and AC power. Thereafter displaying the inverter efficiency as a function of DC power for the* 22^{nd} *of February 2023. The shaded area for the simulated results is due to the measurement uncertainty in GHI, DHI, DNI, and albedo. The measurement uncertainty for measured results has been neglected.*

H.3 Days with varying weather

The 21^{st} of July 2022

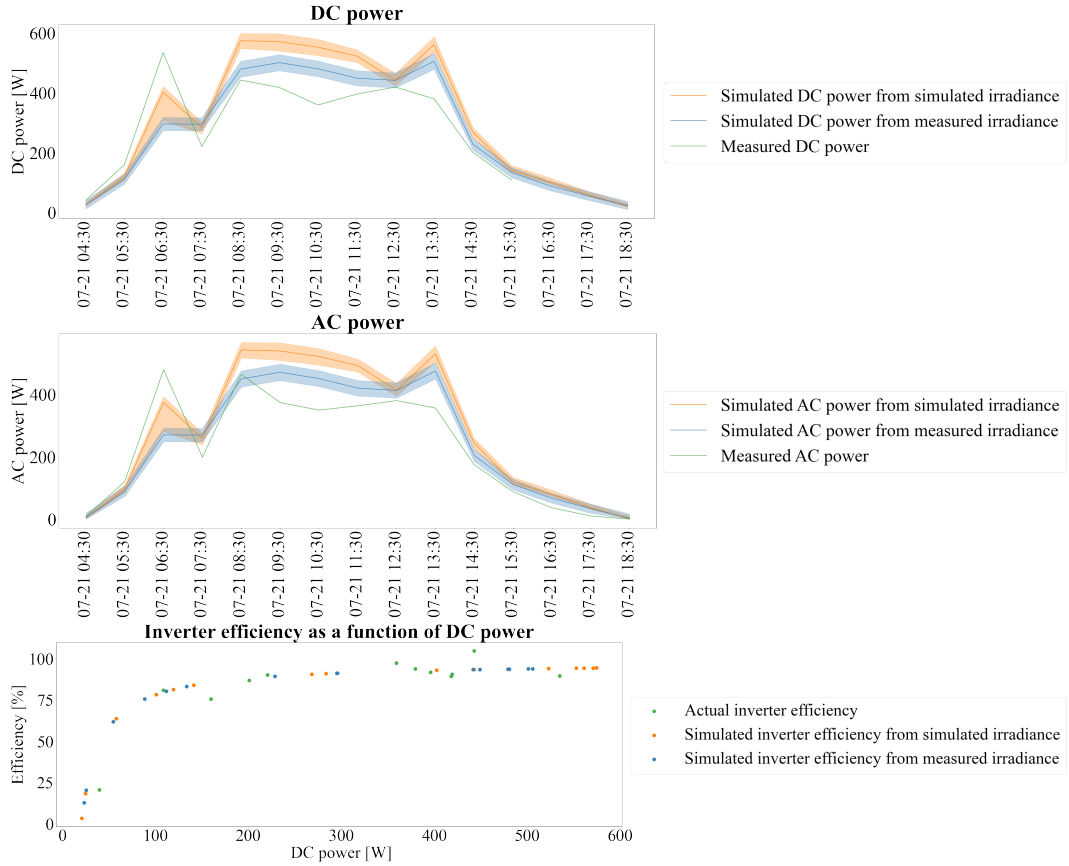

Figure 77: *Simulated DC and AC power using simulated and measured irradiance as input compared to measured DC and AC power. Thereafter displaying the inverter efficiency as a function of DC power for the* 21^{st} *of July 2022. The shaded area for the simulated results is due to the measurement uncertainty in GHI, DHI, DNI, and albedo. The measurement uncertainty for measured results has been neglected.*

The 7^{th} of October 2022

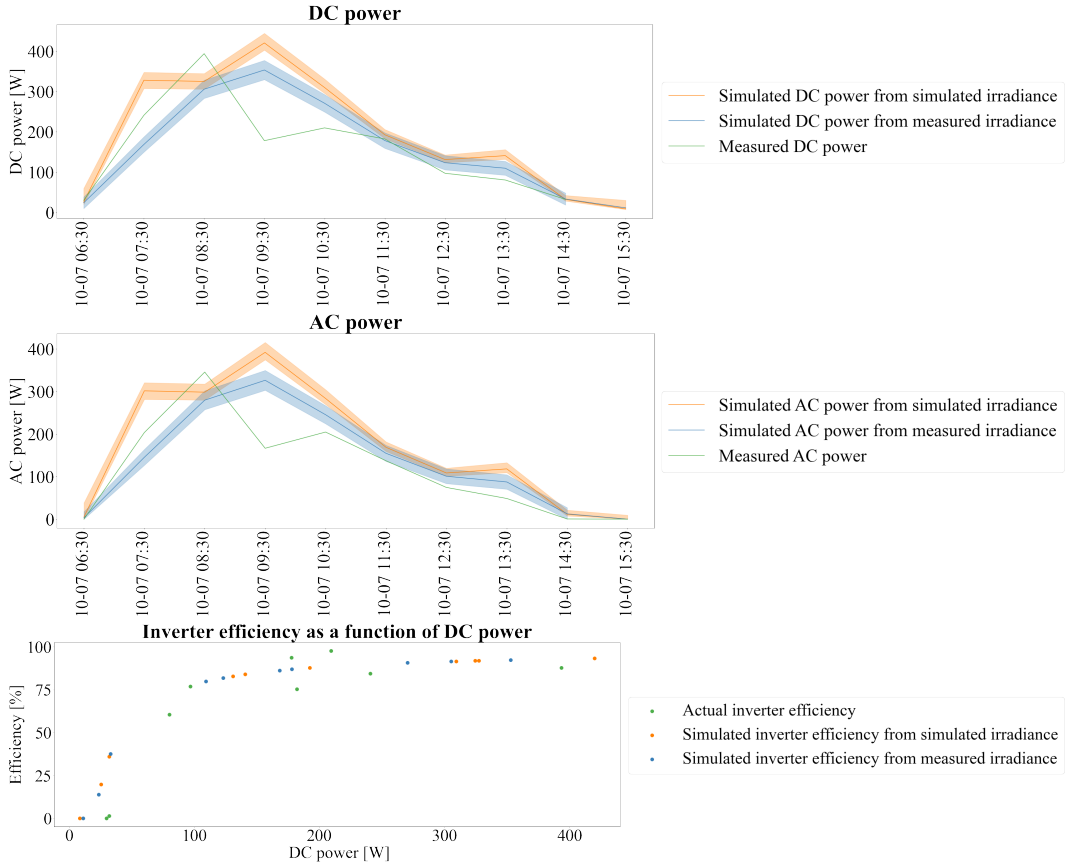

Figure 78: *DC and AC power using simulated and measured irradiance as input compared to measured DC and AC power. Thereafter displaying the inverter efficiency as a function of DC power for the 7^{th} of October 2022. The shaded area for the simulated results is due to the measurement uncertainty in GHI, DHI, DNI, and albedo. The measurement uncertainty for measured results has been neglected.*

The 24^{th} of December 2022

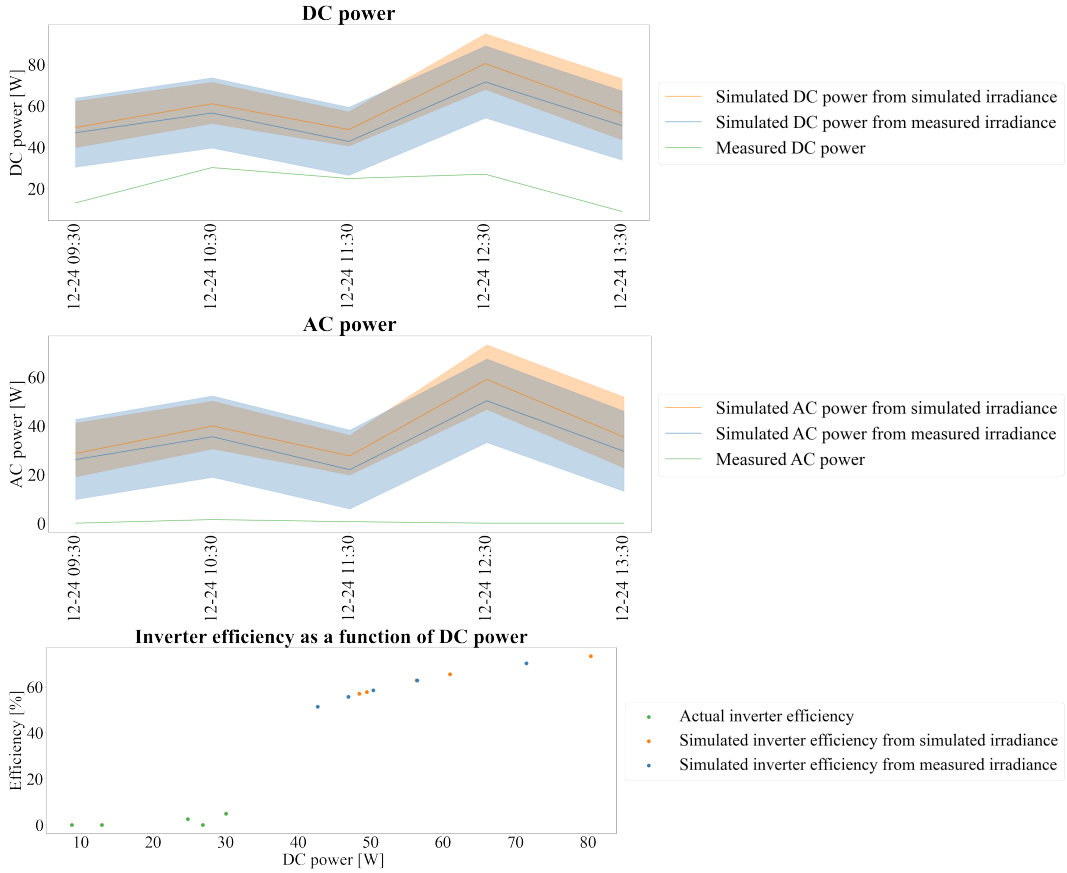

Figure 79: *Simulated DC and AC power using simulated and measured irradiance as input compared to measured DC and AC power. Thereafter displaying the inverter efficiency as a function of DC power for the 24^{th} of December 2022. The shaded area for the simulated results is due to the measurement uncertainty in GHI, DHI, DNI, and albedo. The measurement uncertainty for measured results has been neglected.*

The 26^{st} of February 2023

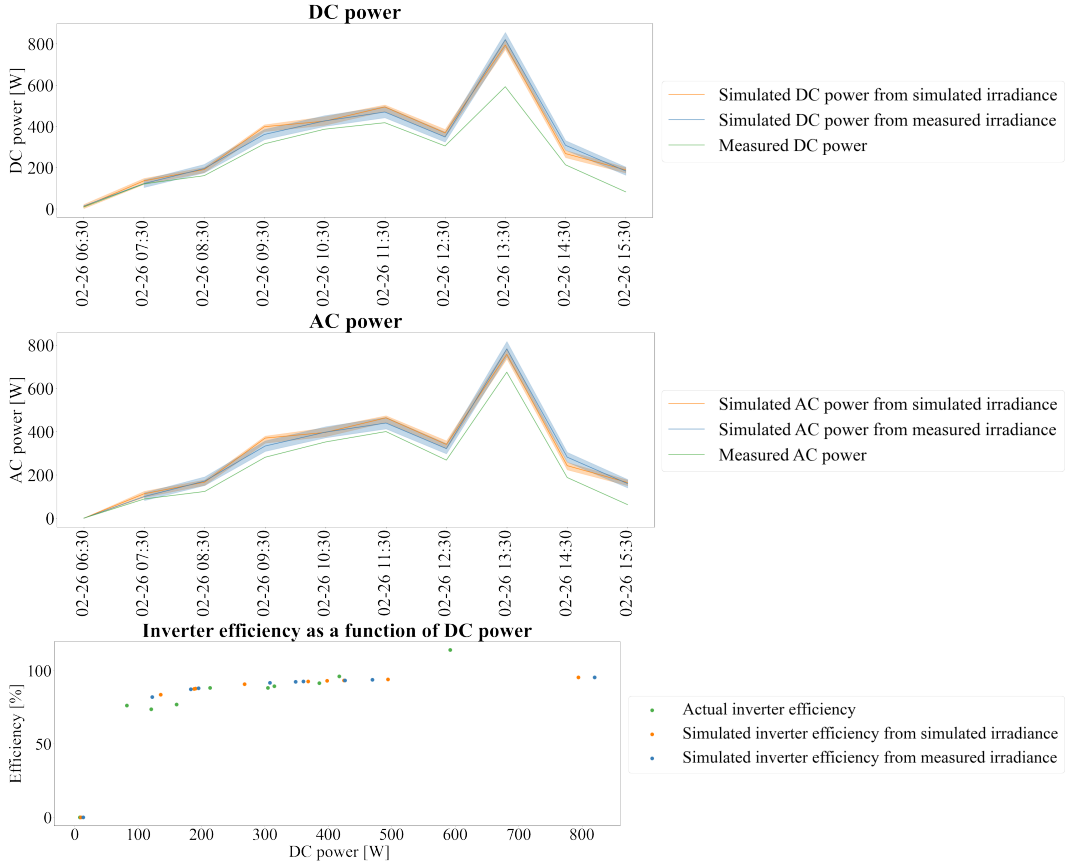

Figure 80: *Simulated DC and AC power using simulated and measured irradiance as input compared to measured DC and AC power. Thereafter displaying the inverter efficiency as a function of DC power for the* 26^{st} *of February 2023. The shaded area for the simulated results is due to the measurement uncertainty in GHI, DHI, DNI, and albedo. The measurement uncertainty for measured results has been neglected.*

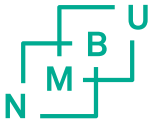

Norges miljø- og biovitenskapelige universitet
Noregs miljø- og biovitskapelege universitet
Norwegian University of Life Sciences

Postboks 5003
NO-1432 Ås
Norway